UNIVERSITY OF CANTERBURY

Department of Physics and Astronomy

CHRISTCHURCH NEW ZEALAND

Diffusion Tensor Imaging of Motor Connectivity in Selected Subjects with Stroke

by

Peter R Smale

MDPH 690
Medical Physics Project

Submitted in partial fulfillment of the requirements for the degree of Master of Science in Medical Physics (Clinical).

Diffusion Tensor Imaging of Motor Connectivity in Selected Subjects with Stroke

Peter R Smale

MDPH 690
Supervisors:
Dr Richard Watts
Dr Winston Byblow
Dr Fergus Thomson

Abstract

Diffusion Tensor Magnetic Resonance Imaging (DTI) is a recently-developed technique that can image *in vivo* the white matter pathways of the central nervous system. This study used 12-direction diffusion-weighted MRI data from nine stroke patients acquired as part of a three-year stroke rehabilitation study coordinated by the Movement Neuroscience Laboratory at the University of Auckland. DTI was used to investigate corticospinal connectivity. From the FA maps, it is found that in those patients whose motor connectivity has been compromised by the stroke to the extent that no motor evoked potential (MEP) can be elicited from a selected affected muscle group, the asymmetry in mean FA values in the posterior limbs of the internal capsules (PLICs) is correlated with functional recovery as measured by the Fugl-Meyer clinical score. Using probabilistic tractography in the contralesional hemisphere produced CST location and somatotopy results that were consistent with those of previous studies. However, in the ipsilesional hemisphere, connectivity results were highly variable. A measure of change in symmetry of mean connectivity is found to correlate with functional recovery as measured by change in FM score. This supports previous work which has correlated CST integrity and functional improvement and it supports the theory that functional recovery after stroke depends on the extent to which motor CNS symmetry can be regained in the new post-stroke architecture. It also suggests that the movement of the fMRI activations occurs in such a way as to make the most of the preserved white matter connectivity.

In a sufficiently complicated problem, actual
sampling is better than an examination of all
the chains of possibilities.
–Stan Ulam,
Adventures of a Mathematician

Acknowledgments

I would like to thank the people in the Movement Neuroscience Laboratory for the opportunity to work in the world of neuroscience. In particular, I thank Winston Byblow, Cathy Stinear, and James Coxon for their enthusiastic guidance.
Thanks also to my supervisor in Christchurch, Richard Watts, for his support. We both grappled a bit with the long-distance supervision.
Finally, thanks to Fergus Thomson at Auckland Hospital, who encouraged and supported my research, even though it wasn't directly related to my hospital work.

Contents

Figures

Tables

Nomenclature

APBT Active Passive Bimanual Therapy

CNS Central nervous system

CSF Cerebrospinal fluid

CST Corticospinal tract

DTI Diffusion tensor imaging

DWI Diffusion-weighted imaging

FA Fractional anisotropy

FACT Fiber assignment by continuous tracking

fMRI Functional Magnetic Resonance Imaging

FMRIB Oxford Centre for Functional Magnetic Resonance Imaging of the Brain

FSL FMRIB Software Library

HARDI High angular resolution diffusion imaging

MEP Motor evoked potential

MNL Movement Neuroscience Laboratory, Department of Sport and Exercise Science, University of Auckland

mpg Motion-probing gradient

MRI Magnetic Resonance Imaging

pdf Probability distribution function

PLIC Posterior limb of the internal capsule

rTMS Repetitive transcranial magnetic stimulation

SLF Superior longitudinal fasciculus

TE Time of echo

TEND Tensor deflection

TMS Transcranial magnetic stimulation

Chapter 1

Introduction

1.1 Aims

1.1.1 The Movement Neuroscience Lab Stroke Study

The Movement Neuroscience Laboratory in the Department of Sport and Exercise Science of the University of Auckland (MNL) is undertaking a three-year clinical study investigating the recovery of chronic stroke patients following a novel physical therapy. Both before and after the therapy, the patients' upper limb function is evaluated according to established clinical scales; their motor connectivity and motor cortical excitability is assessed using transcranial magnetic stimulation; and their sensorimotor cortical function is assessed using functional magnetic resonance imaging (fMRI). A broad goal of this study is to use these parameters to find out how to optimise therapeutic intervention in chronic stroke—some patients will respond better than others to different therapies.

The goal of stroke therapy in general is to enhance the responsiveness of the CNS to its own adaptive changes in order to maximise functional recovery [2]. For chronic stroke patients, spontaneous recovery is very unlikely, but it is still possible to facilitate some recovery by therapeutic intervention [3]. The brain's capacity for plastic change is enhanced by increasing the excitability of the neuronal networks. This occurs naturally in the acute phase. In the chronic phase, this can be done by various therapeutic means—pharmaceuticals or repetitive TMS (rTMS), for instance. Excitability can also be enhanced by physical activity. Constraint-induced movement therapy is a means of forcing use of the affected limb by constraining movement of the unaffected limb. A novel form of therapy, active-passive bimanual therapy (APBT), has been found to promote functional improvement in chronic stroke patients [4]. APBT changes some key neurophysiological parameters that correlate with cortical reorganisation and balancing of activity across the two hemispheres [5]. The aim of the MNL stroke study is to investigate the effect of APBT on patients with different types of stroke by monitoring these parameters before and after therapeutic intervention.

1.2 Background: Stroke, cortical plasticity and recovery

This study is concerned with human cortical reorganisation after stroke—an area of research greatly facilitated in recent years by the development of non-invasive functional imaging. Recent reviews include [2, 3, 6, 7, 8] and there is also a recent book: Recovery after Stroke (2005) [1].

Stroke is the second leading cause of death worldwide and 50% of survivors recover incompletely [1]. Stroke types are broadly divided into *ischaemic*—caused by interruption of blood flow, and *haemorrhagic*—caused by the rupturing of blood vessels. Classification is important because the pathophysiology, mortality and recurrence vary greatly between

different types [1]. A stroke results in a lesion consisting of a core of dead neurons surrounded by an underperfused penumbra [7], in which ischaemia has been insufficient to kill the neurons but has nevertheless rendered them dysfunctional [3]. It is possible for this region to regain some of its viability during the healing process.

In a healthy adult, sensorimotor motor cortical activity in each hemisphere is approximately symmetrical [3]. After a stroke, in the chronic phase, this activity is reduced in the hemisphere containing the lesion, and often abnormally enhanced in the contralesional hemisphere [5]. The recovery of motor function is associated with the extent to which the original symmetrical activation patterns can be regained within the constraints of the individual patient's new post-stroke functioning anatomy and physiology [2, 5][1]. APBT has been found to reduce abnormally high TMS excitability thresholds and increase the size of motor representations in the ipsilesional cortex, while activity in the contralesional cortex is reduced [3].

Recovery among stroke patients varies greatly, even amongst those whose strokes have identical acute characteristics [3]. Post-stroke, there is more or less continuous functional adaptation at the cellular and systems levels, occurring most vigorously in the weeks and months following the event, but persisting, and capable of being revivified to some extent even in the chronic phase [2, 7]. In neuroscience, the term *plasticity* refers to functional adaptation at molecular, synaptic, cellular, network, and system levels following injury [8]. Although a detailed discussion of plasticity is beyond the scope of this document, for completeness, various possible mechanisms of plasticity are summarised in Table 1.1.

Modern non-invasive neuro-imaging provides an unprecedented opportunity to study the recuperative role of the central nervous system following stroke in human beings [3], and therefore also to devise new therapies based on neurobiological principles and tailored to suit individual pathology [2]. The MNL study uses TMS and MRI in conjunction with clinical assessment to monitor the response of patients to the APBT intervention. TMS uses a figure-eight-shaped coil to induce a focused pulse of electrical activity in a selected cortical representation, triggering a motor-evoked potential (MEP) in the associated muscle(s). In patients with stroke, it may be more difficult to elicit a MEP in the associated muscle because the cortical excitability threshold is abnormally high. TMS therefore provides a probe into both neural circuit connectivity and excitability.

MRI uses the relaxation times of precessing hydrogen protons under the influence of radio-frequency magnetic pulses to provide various contrasts, providing quite diverse (and, compared to conventional radiographic techniques, harmless) internal imaging possibilities. Of particular interest is the *functional* capability of MRI. Changing localised concentration of paramagnetic deoxy-haemoglobin in cerebral blood flow during activity, whether mental or physical, is the basis of functional MRI. Structural contrasts include T_1, most commonly used for anatomical imaging, and T_2, which highlights cerebrospinal fluid.

There is also Diffusion-weighted magnetic resonance imaging (DWI), in which the contrast is provided by varying cellular-scale structural constraints on the intravoxel microscopic random motions of water molecules. A DWI dataset can be post-processed to

[1]The term "functional recovery" could refer to the improvement of limb function, or to the improvement of viability of motor pathways. This is an important distinction in the context of this study. In this report, I use "functional recovery" only to describe the kind of improvement of limb function that is assessed against established scales like the Fugl-Meyer scale. Plastic recovery in the CNS I will refer to as "neurophysiological recovery".

Plasticity Mechanisms
Network
1. Recovery of neuronal excitability: resolve cell and axon ionic dysequilibrium; reverse edema; resorb blood; reverse transsynaptic diaschisis
2. Activity in partially spared pathways
3. Representational plasticity within neuronal assemblies
4. Recruit a parallel network not ordinarily activated by a task (e.g. unaffected hemisphere or ipsilesional prefrontal cortex)
5. Engage a subcomponent of a distributed network (e.g. a pattern generator for walking)
6. Modulation of excitability by neurotransmitters (e.g. serotonin, dopamine)
Pre/Postsynaptic
1. Modulate neuronal intracellular signalling for metabolic functions (e.g. neurotrophic factors, protein kinases)
2. Alter synaptic plasticity: modulate basal synaptic transmission; neurotransmitter and peptide modulators alter excitability; denervation; hypersensitivity of postsynaptic receptors; regulation of number or types of receptor (e.g. AMPA receptors); activity-dependent unmasking of synaptic connections; experience-dependent learning (e.g. long-term potentiation); dendritic sprouting onto denuded receptors of nearby neurons
3. Axonal and dendritic collateral sprouting from uninjured neurons
4. Axonal regeneration: gene expression for remodeling proteins; modulation by neurotrophic factors; actions of chemoattractants and inhibitors in the milieu
5. Remyelination
6. Reverse conduction block; ion channel changes on axons
7. Neurogenesis

Table 1.1: Potential intrinsic biological mechanisms to lessen sensorimotor impairments and disabilities (From Barnes et al. (2005) p 52 [1])

yield the structure of white matter.

The contribution of the present study to the MNL stroke study is to assess connectivity in the study subjects using DWI and to determine ways in which diffusion parameters can aid or inform clinical assessment and therapy.

1.3 Recent research in Diffusion-Weighted MR Imaging

This section reviews the development of diffusion MRI and is necessarily brief about the underlying physics. Details about the physical principles of MRI will be given in Chapter 2.

The attenuating effect of the diffusion of liquid molecules on T_2 relaxation times in Nuclear Magnetic Resonance was first noted by Hahn in his exposition of spin echoes in 1950 [9]. Carr and Purcell reformulated and extended this work in 1954 [10], and suggested a way of measuring the diffusion constant based on their observation that the 180° pulse in a spin echo sequence partially eliminates the attenuation caused by diffusion. Stejskal and Tanner published the optimal multiple diffusion-probing gradient spin echo pulse sequence that underlies modern DWI in 1965 [11]. They noted that there is a Fourier relationship between the diffusion function $P(\mathbf{r})$, representing the probability that a water molecule diffuses a distance $\mathbf{r}$ in time τ, and the diffusion MR signal $E(\mathbf{q})$ [12]. Specifically: $P(\mathbf{r}) = F[E(\mathbf{q})]$ for diffusion wave vector $\mathbf{q} = \gamma\delta\mathbf{g}$. γ is the water proton gyromagnetic ratio, $\mathbf{g}$ is the diffusion-probing gradient field, and δ is the duration of the gradient. With this so-called Q-space imaging, it is possible to measure directly the microscopic diffusion function within each voxel of the MR image [12].

Measurement of the complete diffusion function requires long acquisition times and strong magnetic field gradients, which means Q-space techniques have been used only for materials and small animals. The potential for using diffusion as a *clinical* imaging parameter was ascertained in the mid-1980s [13], and technological advances allowed the production of diagnostic-quality images on commercial scanners in the early 1990s. Further advances in DWI have also required the development of models of diffusion in human white matter, permitting better approximation of the true diffusion function while remaining within clinically acceptable constraints.

Diffusion is measured by virtue of the change in precession frequency induced in nuclei whose direction of diffusion has some component parallel to the direction of an imposed magnetic field gradient. Using this fact, a number of diffusion-measuring gradients, applied with some isotropic distribution of directions, can be used to generate an image of preferred directions of diffusion within a volume. Diffusion *anisotropy* results from the constraint of diffusion in vivo by cell membranes. In particular, in the brain, anisotropic diffusion has been found to be consistent with the presence of oriented bundles of the myelinated axons which constitute white matter [14].

Indirect imaging of the oriented axon bundles ("white matter tractography") therefore became a possibility by assuming that the local diffusion signals, i.e. the signals from a single voxel along a series of motion-probing gradient directions, may be modeled by a 3D Gaussian distribution. The covariance matrix of this Gaussian is proportional to the *diffusion tensor* [15], a real and symmetric 3×3 matrix whose elements encode the diffusion information: how much, and in which direction. Several scalar measures of diffusion anisotropy can be derived from the diffusion tensor. Conventionally, these require an eigenvalue decomposition of the diffusion tensor in each voxel: the direction

of anisotropy is usually computed from the eigenvectors, and a quantity representing the degree of anisotropy can be calculated from some combination of the eigenvalues. Invariant measures have also been derived from the diffusion ellipsoids without the need for diagonalisation of the tensor [16], which can produce image artifacts in the presence of background noise [17]. The diffusion tensor is strikingly visualised as a field of ellipsoids whose dimensions are encoded in the tensors (see Fig. 1.1). The *Diffusion Tensor Imaging* (DTI) analysis was first explicated by Le Bihan, Pierpaoli, Basser, and others in the mid-1990s (eg. [13, 18, 19]).

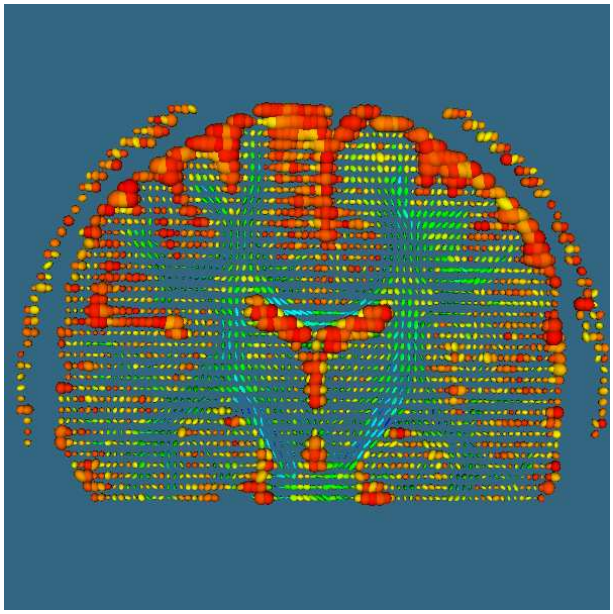

Figure 1.1: The diffusion tensors can be represented by ellipsoids whose axes point in the directions given by the eigenvectors and have magnitudes given by the corresponding eigenvalues. White matter can be recognised as prolate ellipsoids, while CSF in the ventricles and surrounding the brain corresponds to spheres (isotropic diffusion) with large radii (high apparent diffusion coefficient).

Anisotropy is usually quantified as the fraction of the norm of the diffusion tensor that can be ascribed to anisotropic diffusion, the fractional anisotropy (FA), but there are other characterisations (given in [20], and see also [21]). White matter tractography has been accomplished by generating streamline trajectories through the principal eigenvector field in much the same way that flow lines are generated through a vector field in hydrodynamics. Review papers include [20, 22]. The most well-known of these algorithms is the FACT (Fiber Assignment by Continuous Tracking) of Mori et al. (1999) [19]. Tracking begins at specified seed points, stepping through the volume following the direction of the principle eigenvectors using trilinear interpolation. Streamlines are terminated when certain stopping criteria are met, eg. the FA may fall below a threshold value, or the angle between principle eigenvectors in successive voxels may be anatomically infeasible. Another algorithm, TEND (Tensor Deflection) [23], specifies an initial vector of anisotropy which is transformed using the entire diffusion tensor interpolated at each step. The TEND and FACT algorithms are called *deterministic*.

The coincidence of major eigenvector direction and local fibre tract orientation has been justified histologically (e.g. [19]). Several free DTI software packages have become available [24, 25, 26, 27, 28], many studies have used DTI in applications (e.g. [29,

30, 31, 32]), and an atlas of human white matter has been produced [33]. Thus we can say that this *tensor model* of diffusion has met with some success—the information it gives us has been shown to correspond to some considerable extent with what we know about real white matter architecture in the human brain. However, this requires qualification: it is an assumption of the tensor model that the predominant direction of diffusion can be modeled by a single Gaussian. This assumption is inadequate when two or more myelinated fibres cross in a single voxel, as occurs, for example, where the fibres of the corticospinal tract (CST) intersect with those of the corpus callosum and the superior longitudinal fasciculus. A High Angular Resolution Diffusion Imaging (HARDI) study has demonstrated significant multimodal directional structure in regions where fibres cross [34]. Such voxels will show a relatively low FA. A higher uncertainty in fibre direction implies a lower FA value, but not vice versa [15]: a low FA may indicate uncertainty in fibre direction as well as the absence of myelinated fibres, which presents difficulties in the interpretation of the tracking algorithm in such regions [35]. This issue is informally known as the *crossing problem*. Finding a solution to it that does not require impractical numbers of diffusion-weighted acquisitions—the HARDI study used 126 [34]—or inordinate computation time, is the main area of research in theoretical DWI. Some key papers include [15, 34, 36, 37, 38, 39].

These efforts have involved more complicated models of the diffusion process than the tensor model. In [34], for example, each voxel is assumed to be subdivided into a discrete number n of homogeneous regions, each with a Gaussian distribution of fibre directions. The objective is then to determine the n tensors and their corresponding volume elements that minimise a least-squares fit with the observed diffusion signal. Using the Expectation-Maximisation algorithm along with certain physiological constraints on the eigenvalues of the tensors, this study was able to resolve underlying fibre populations corresponding to known anatomy. It was found that due to partial volume effects, the calculated fibre orientations differed significantly from those given by the usual (deterministic) tensor method in regions of fibre heterogeneity.

The only work to extend the direct diffusion spectrum measurement approach suggested by the work of Stejskal and Tanner has been the "Q-Ball" imaging of [12, 37], in which a spherical Funk-Radon transform is applied to the cartesian Q-space, making considerable savings in computation time and visualising complex intravoxel neural architecture. This is new work and is not widely available.

Given a model of the diffusion function, whether it be the tensor model or a more elaborate one like the multi-tensor model, it becomes possible to use *probabilistic* methods to obtain the likelihood of anatomical connectivity between any two points in the brain [39]. Probabilistic tractography provides quantitative information about white matter connectivity. Given a diffusion signal model and a noise model, we can obtain the likelihood of the data Y given the parameters Ω: $P(Y|\Omega)$. Then *Bayes' rule* permits the computation of the *posterior* distribution of the parameters given the data: $P(\Omega|Y) \propto P(Y|\Omega)P(\Omega)$. That is, Bayes' rule lets us compute a probability density function (pdf) for each voxel, given some diffusion data, of what the likely true diffusion statistics of that voxel are, assuming the models for signal and noise [28]. Now, given the voxel-wise pdfs, sampling methods such as Monte Carlo can be used to determine global parameters on connectivity from each voxel in the volume to every other voxel [15]. Connectivity in the human thalamus obtained by this probabilistic method was found to correspond well to predictions derived from invasive studies of non-human primate thalamus [40].

The current study relies on the probabilistic tractography software FSL [28]. At the time of writing, FSL's diffusion tractography is based on a model of a single direction of anisotropy on an isotropic background. Compared with the Gaussian tensor model, this model avoids errors due to sorting the eigenvectors and is more amenable to be extended to allow more than one fibre compartment. The next release of FSL will include this capability (T. Behrens [41]). Probabilistic models that are able to account for any distribution of intravoxel fibre directions have been tested [39], but are not yet freely available.

1.3.1 Aims of this project

From the point of view of DWI, the most important mechanisms of plasticity are those involving repair of neuronal anatomy: axonal and dendritic sprouting, remyelination, and neurogenesis. However, in the chronic phase, these processes take place only to a limited extent, and DWI does not discern them directly—they contribute to changes in the diffusion properties that are beyond the resolution of DWI. In the MNL stroke study, just one diffusion weighted dataset was obtained prior to therapy, under the assumption that therapy-related change will be functional rather than structural.

The current study has the following aims:

1. The papers of Holodny et al. (2005) [42] and Zarei et al. (2007) [43] investigate the somatotopic arrangements of corticospinal tracts in the internal capsules. The former used the deterministic tractography algorithm and the latter used probabilistic methods. The current study attempts to replicate these very recent results in a new sample population of stroke patients. While the contralesional hemispheres should yield similar results, the ipsilesional internal capsules could potentially show very different arrangements.
2. Functional MRI activations before and after therapy are different, especially in the ipsilesional hemisphere. Using probabilistic connectivity mapping, this study aims to image the active motor pathways at the level of the posterior limbs of the internal capsules (PLICs). The active areas, especially in the lesioned hemisphere, could potentially change if there is significant recruitment of new pathways following therapy.
3. In some patients, TMS failed to elicit any MEP, which suggests very poor or interrupted connectivity in their motor pathways. This study aims to find some correlation between the extent of connectivity revealed by probabilistic connectivity mapping and the presence or absence of MEPs.

Chapter 2

The Physics of Diffusion Tensor Imaging

This chapter reviews the fundamentals of diffusion MRI. The first section outlines the aspects of the mechanics of MRI with a view to explaining diffusion imaging only. In the interests of brevity, topics such as the imaging of various contrasts by different pulse sequences, e.g. inversion recovery sequences for T_1, are omitted.

In order to explain imaging using the diffusion signal, it is necessary to explain the behaviour of nuclei in magnetic fields (§2.1.1), the generation of the particular tissue contrasts that make MRI such a powerful imaging technique, and the use of the spin echo magnetic field pulse sequence to obtain T_2-weighted MR images (§2.1.2). The attenuating effects of the microscopic motion of water molecules can then be discussed (§2.1.3). The second part of the chapter describes the two types of tractography algorithms by outlining first the deterministic FACT algorithm (§2.2.2), and then the Bayesian probabilistic methods of FSL's FDT tractography tool (§2.2.3).

2.1 Obtaining a diffusion-weighted magnetic resonance signal

2.1.1 The mechanics of nuclear magnetic resonance

Magnetic Resonance Imaging records the radio frequency signals emitted by the precessing spins of hydrogen protons *in vivo* under the influence of superimposed magnetic fields.

A proton is susceptible to the influence of a magnetic field by virtue of its magnetic dipole moment. Because it also possesses intrinsic angular momentum, or *spin*, the proton does not simply align itself along the direction of the magnetic field lines. Rather, the direction of its spin *rotates around* the direction of the magnetic field lines at a constant frequency dependent on the strength of the magnetic field. This motion is called *precession*. The angular frequency of precession is called the *Larmor frequency*, which is given by

$$\omega = \gamma B, \tag{2.1}$$

where γ is the *gyromagnetic* ratio (derived from the magnetic dipole moment and the spin of the proton), and B is the magnitude of the magnetic field.

For protons, the Larmor frequency is 42.58 MHz/T, which lies in the radio frequency part of the electromagnetic spectrum for magnetic fields of a few T. For electrons, which are 2000 times less massive than protons, the Larmor frequency lies in the microwave range—there will never be electron-targeted MRI on living humans.

Due to thermal interactions between the atoms in a sample exposed to a magnetic field, only a very small excess fraction (a few per million) of the protons find their preferred alignment along the direction of the imposed field. The fraction may be relatively small, but the tissue proton density of $\sim 10^{20}$ per mm^3 means that the excess generates a *net magnetisation* vector, pointing in the direction of the external field and with a magnitude

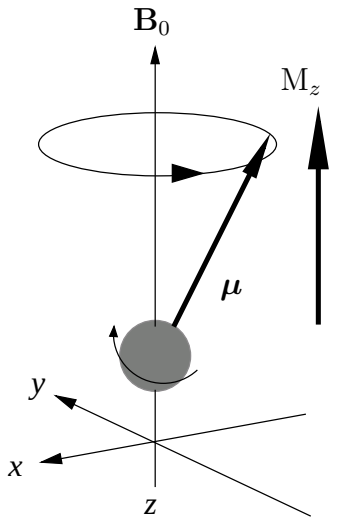

Figure 2.1: **Precession of net magnetisation vector around a magnetic field aligned in the z-direction.** In this case, (2.3) says that M_z will not change, while change in the transverse components M_x and M_y will be constant—in other words, it describes a circle in the xy-plane.

defined as the number of spins per unit volume times the average magnetic moment:

$$\mathbf{M} = N\langle\boldsymbol{\mu}\rangle. \tag{2.2}$$

It is an important quantum mechanical result that the net magnetisation vector has the same behaviour in an external magnetic field as the individual magnetic moment. It obeys the same equation of motion:

$$\mathrm{d}\mathbf{M}/\mathrm{d}t = \gamma(\mathbf{M} \times \mathbf{B}). \tag{2.3}$$

This is the *Bloch equation with no relaxation*. It describes the rotation around the **B**-axis of a vector anchored at the origin, and from it we can derive the Larmor equation.

Equation (2.3) does not completely describe the motion of the net magnetisation vector. Thermal agitation and internuclear interactions are responsible for deviations of **M** from its equilibrium position along the direction of the external field, leading to additional terms. For argument's sake, let $\mathbf{B} = B_z\hat{\mathbf{z}}$, a static field oriented in the z-direction, as in Figure 2.1. The total spin energy is then $E = -B_zM_z$. Note that generally, while thermal effects result in a change of the total energy of the system, internuclear interactions like the transfer of energy between spins leave the total energy unchanged [44]. If thermal agitation nudges **M** from its equilibrium, **M** will *relax back* into its equilibrium in a time proportional to how far it was initially offset, so for the longitudinal component M_z, the component that affects the total spin energy, we can say

$$\frac{\mathrm{d}M_z}{\mathrm{d}t} = \frac{1}{\mathrm{T}_1}(M_0 - M_z), \tag{2.4}$$

where T_1 is the relaxation time, also called *spin-lattice* relaxation because it involves the dissipation of energy from the proton into the surrounding molecular lattice.

It turns out that grey matter has a longer T_1 than white matter, so it takes longer for grey matter to recover from any perturbation away from equilibrium.

Obviously, perturbation from equilibrium also affects the transverse components of $\mathbf{M}$. In contrast to M_z, M_x and M_y will *increase* with the perturbation and then *decrease* with relaxation:

$$\frac{\mathrm{d}M_x}{\mathrm{d}t} = -\frac{M_x}{\mathrm{T}_2}, \qquad \frac{\mathrm{d}M_y}{\mathrm{d}t} = -\frac{M_y}{\mathrm{T}_2}. \tag{2.5}$$

This time, the transverse relaxation time T_2 depends on the transfer of spin energy amongst neighbouring nuclei (without conversion to kinetic energy of the atoms—equations (2.5) do not affect $E = -B_z M_z$). The transverse relaxation is often called *spin-spin* relaxation.

Grey matter has a longer T_2 than white matter, while CSF and other fluids have very long T_2 values. T_1 is always *greater* than T_2.

These considerations complete the mechanical picture of nuclear induction in a static external magnetic field, first described by Bloch in 1946 [44]. For completeness, the full Bloch equations for a static field $\mathbf{B}= B_x\hat{\mathbf{x}} + B_y\hat{\mathbf{y}} + B_z\hat{\mathbf{z}}$ in component form are

$$\begin{aligned}
\frac{\mathrm{d}M_x}{\mathrm{d}t} &= \gamma(M_y B_z - M_z B_y) - \frac{1}{\mathrm{T}_2}M_x \\
\frac{\mathrm{d}M_y}{\mathrm{d}t} &= \gamma(M_z B_x - M_x B_z) - \frac{1}{\mathrm{T}_2}M_y \\
\frac{\mathrm{d}M_z}{\mathrm{d}t} &= \gamma(M_x B_y - M_y B_x) + \frac{1}{\mathrm{T}_1}(M_0 - M_z).
\end{aligned} \tag{2.6}$$

After a 90° pulse, the net magnetisation lies entirely in the transverse plane: $\mathbf{M}_{t=0} = (M - 0, 0, 0)^{\mathrm{T}}$, and the solutions to these equations are, respectively:

$$\begin{aligned}
M_x(t) &= M_0 e^{-t/\mathrm{T}_2}\cos(\omega_0 t) \\
M_y(t) &= M_0 e^{-t/\mathrm{T}_2}\sin(\omega_0 t) \\
M_z(t) &= M_0(1 - e^{-t/\mathrm{T}_1}),
\end{aligned} \tag{2.7}$$

where $\omega_0 = \gamma B$. The exponential parts of these equations are plotted in Figure 2.2 to show the different tissue contrasts graphically. The characteristic times used to plot the graphs for the different tissues are shown in Table 2.1.

Tissue	T_1 (ms)	T_2 (ms)
Fat	260	80
White matter	780	90
Grey matter	900	100
CSF	2400	160

Table 2.1: **Relaxation characteristic times for major neurological tissues.**

2.1.2 Obtaining a nuclear magnetic resonance signal

The 90° pulse and the free induction decay signal. We can superimpose a second magnetic field *pulse* $\mathbf{B}_1 = B_x\hat{\mathbf{x}}$, perpendicular to the static field $\mathbf{B} \equiv \mathbf{B}_0$. The idea of the $\mathbf{B}_1$ pulse is that if it is applied at the Larmor frequency, it exerts a new torque on the precessing spins which tips $\mathbf{M}$ away from the $\mathbf{B}_0$ direction, and continues to tip it until the pulse is switched off. If the pulse is applied for the right length of time, the magnetisation vector is left precessing entirely in the transverse plane. This is called

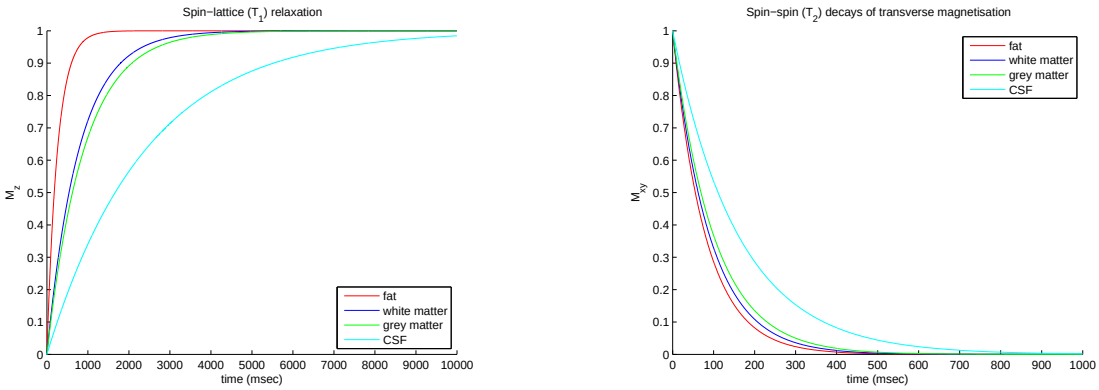

Figure 2.2: **Longitudinal and transverse relaxation times for different tissues.**

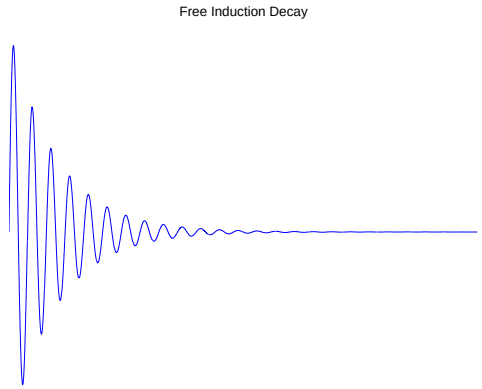

Figure 2.3: **The free induction decay signal.** The transverse component of the magnetisation vector is at a maximum when the 90° pulse is switched off. Then its decay is registered by an appropriately-placed coil as an exponentially decaying oscillating current.

a *90° pulse*. The rotating transverse magnetisation induces an oscillating current in an appropriately-placed coil. The decay of the transverse magnetisation after the 90° pulse is registered by the coil as an exponentially decaying oscillation corresponding to the transverse magnetisation given in (2.7) (see Figure 2.3). This transient nuclear induction signal is called the *free induction decay* signal, or FID.

Spin Echoes. There are in fact two processes that contribute to the decay of the tranverse magnetisation and the generation of the FID. The true T_2 relaxation rate is accelerated by inhomogeneities in the magnetic field. Local variations in the field experienced by protons are due to nearby spins and variations in $\mathbf{B}_0$. This means that the precession frequencies of neighbouring protons are not always the same—there is actually a distribution of frequencies, the mean of which is the Larmor frequency. Some nuclei precess faster and some slower. Consequently, *dephasing* of the precessing nuclei accelerates the loss of the transverse signal, so that the FID decays at a rate proportional to the characteristic time $T_2^\star < T_2$.

The effects of the inhomogeneities in the external field can be separated from spin-spin relaxation by a *spin echo* pulse sequence [9]. A spin echo pulse sequence consists of a 90° degree pulse followed by a 180° pulse after a time delay of TE/2 milliseconds. At the

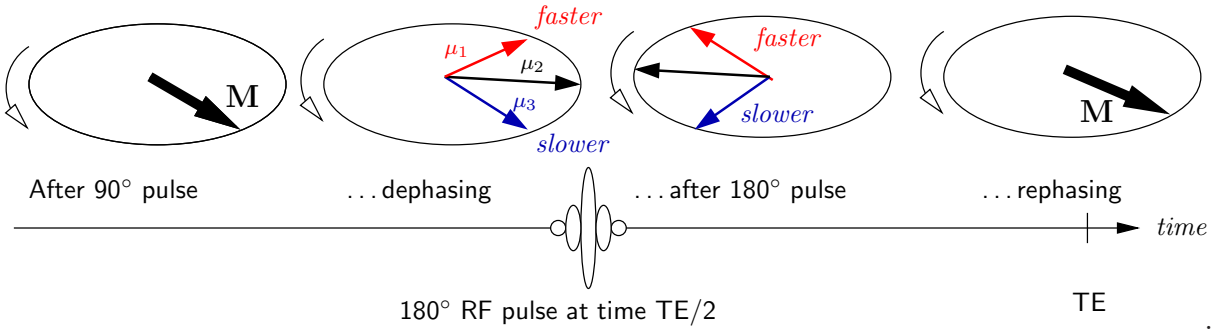

Figure 2.4: **Spin Echo pulse sequence.** The 90° pulse leaves the net magnetisation vector **M** rotating in the transverse plane. The frequency of precession varies from nucleus to nucleus ($\boldsymbol{\mu}_i$), leading to $T_2^\star$ dephasing. A 180° pulse applied at TE/2 puts the faster vectors behind and the slower ones in front. The rephased nuclear magnetic moments produce a new net magnetisation. Dephasing resumes (not shown).

echo time TE, the signal is recorded. This procedure is shown in Fig. 2.4. Before the 180° pulse, the distribution of the individual magnetic moment vectors has fanned out over the whole transverse plane, so that their sum, i.e. the net magnetisation, reduces to zero. The effect of the 180° pulse is to flip the spins. The result is rather like running a film of runners backward. The faster runners who were racing ahead are now behind, while the slower ones who were lagging further and further behind are suddenly in front, so that they all cross back over the start line at the same time. This corresponds to the "echo" in the FID. The amplitude that the echo attains is a function of the true T_2, so that even with successive 180° refocusing pulses, separated by a time TE, the net magnetisation eventually falls to nothing. The resulting voltage signal is a series of shrinking, back-to-back FIDs.

2.1.3 Water diffusion attenuates the T2 signal: Measuring diffusion

In 1954, Carr and Purcell wrote that microscopic diffusion, or *Brownian motion*, of water molecules can severely compromise measurement of T_2 relaxation times [10]. The problem is that during the time it takes for the signal to be localised, the "labelled spins" in water molecules that contribute to the signal may have diffused out of the region of interest. In terms of the distance travelled by a diffusing molecule in a given time, measurable diffusion occurs on T_2 time scales and acts to exponentially attenuate the recorded MR signal.

The theory of diffusion was developed by Einstein in one of his three great papers of 1905 [45]. From his work on statistical mechanics, he correctly determined the 3D relationship between how far a particle travels and the diffusion properties of the medium:

$$\langle \mathbf{r}^2 \rangle = 6\mathbf{D}t. \tag{2.8}$$

The distance travelled, $\mathbf{r}$, is a "crow flies" distance, not the actual path length. According to this equation, given many particles diffusing in a medium, the average squared distance a particle will travel in a given time t is proportional to the self-diffusion properties $\mathbf{D}$ of the medium[1]. The quantity $\mathbf{D}$ is a tensor, encoding both direction and magnitude

[1]This is a profound result. It represents a solution to the problem posed by (apparently perpetual) Brownian motion: how to reconcile time-symmetric Newtonian mechanics with the second law of thermodynamics [46].

information.

Biological tissues are heterogeneous. The apparent diffusion coefficent is affected by factors like proteins and cell boundaries. Because of this, diffusion is seldom isotropic in three dimensions. Diffusion *anisotropy* is the basis of diffusion tensor imaging.

From the point of view of MRI, we could expect that it might be possible to obtain a diffusion-weighted signal by virtue of the rate of change of the nuclear precession, and the consequent phase difference, caused by the diffusion of the nucleus into a region where the magnetic field is slightly different [10]. In 1965, Stejskal and Tanner laid the foundations of modern DWI by adding paired motion-probing magnetic field gradient (mpg) pulses to a spin echo pulse sequence [11]. The relative locations of the mpg pulses is shown in Fig. 2.5. The first pulse, of duration δ, labels a set of nuclei by imposing a gradient pulse. The second pulse, comes at time Δ after the first, and has the same duration δ. Because it comes *after* the 180° pulse, it has an opposite, "unlabelling" effect on the spins. With no diffusion, the second pulse undoes any phase change the nuclei may have undergone as a result of the first pulse. So for static spins, the bipolar gradient pair is said to be transparent [47], and there will be no attenuation of the T_2 signal when it is recorded at the echo time. If nuclei move on the other hand, the phase difference they acquire during their motion along the mpg does not cancel out, there is destructive interference between the nuclear magnetic moments due to their distribution, and there will be some corresponding attenuation of the T_2 signal. From Equations (2.7) and (2.8), the diffusion-weighted signal in the ith gradient direction can be written [15]

$$S_i = S_0 \exp[-b\mathbf{g}_i\mathbf{D}\mathbf{g}_i{}^{\mathrm{T}}], \tag{2.9}$$

where $S_0 \propto M_0 e^{-TE/T_2}$ is the signal with no motion-probing gradients applied. The vector $\mathbf{g}$ contains the directional information for each mpg in the form of a list of unit vectors. The number b has units of seconds per square millimetre and is known as the *b-factor*. It can be obtained analytically by solving the equation of coherence loss derived by Stejskal and Tanner [48] with mpg pulse timing Δ, duration δ, and gradient strength G (see Fig. 2.5):

$$b = (\gamma G\delta)^2(\Delta - \delta/3). \tag{2.10}$$

The b-factor is "tuned" to optimise diffusion sensitivity by adjustment of mpg strength, timing, or duration. Since the diffusion coefficient of water in biologic tissues is $\sim 10^{-3}$ mm^2/s, b is generally $\sim 10^3$ s/mm^2, resulting in a signal attenuation $\sim 1/e$ typically.

2.2 From diffusion signal to connectivity

2.2.1 Obtaining the diffusion tensor

A nucleus that moves through an applied magnetic field gradient experiences a changing precessional frequency in accordance with Larmor's equation (2.1). Clearly though, it is only the extent to which its displacement has a component *along* the direction of the applied gradient that induces a frequency change — a nucleus that moves entirely perpendicularly to the applied gradient direction will experience no change in its precessional frequency. Because diffusion can only be measured along one direction at a time, a more accurate measure of the diffusion coefficient is obtained by applying several mpg pairs and acquiring a whole volume of scans along each (see Figure 2.6). From the data from each

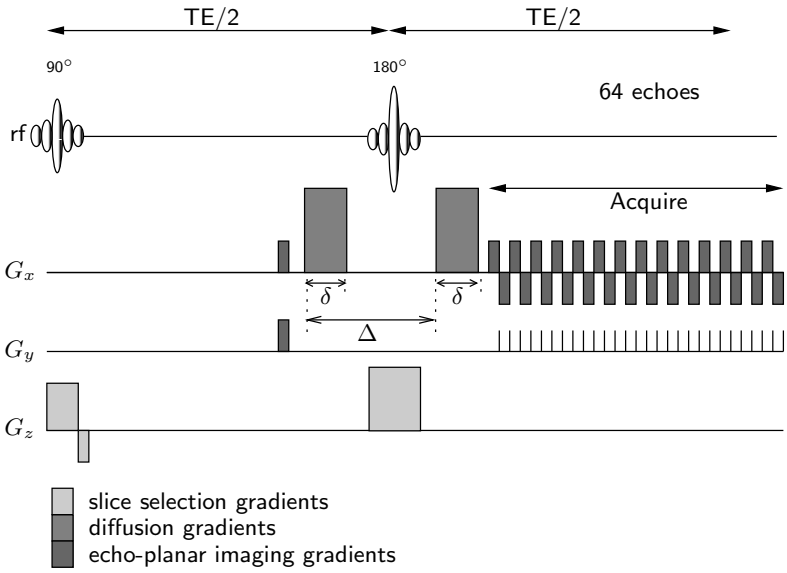

Figure 2.5: **Spin echo pulse sequence with motion-probing gradients** This is an echo-planar imaging (EPI) sequence, similar to the one used by the Siemens Magnetom Avanto 1.5 T at the Centre for Advanced MRI. In the picture, the gradients are aligned purely in the x direction. Source: Turner & Le Bihan (1995) [49]

mpg direction for each voxel, the full diffusion tensor can be estimated by a least squares regression (See §2.2.2 below). A minimum of 6 directions and a $b = 0$ (i.e. no mpg, or pure T_2) scan are required to obtain adequate 3D information. The diffusion datasets for the MNL stroke study used 12 directions. The number of directions is discussed further in §2.2.4.

One might expect a diffusion image to be bright in regions of fast diffusion, and darker in regions of restricted diffusion. In the images in Fig. 2.6, we see the opposite contrast. The reason for this can be seen by inspection of (2.9). The (most commonly used) pulse sequence is a spin echo sequence *weighted* to be sensitive to diffusion by tuning $b \sim 10^3$ sec/mm^2. By (2.9), any diffusion then results in the registration of some fraction of the pure T_2-weighted signal: in the ventricles in Fig. 2.6, diffusion is fast and isotropic, the signal is therefore heavily attenuated, and the image is dark; where the image is bright, e.g. in callosal areas (shown by the yellow ellipses on the T_2 image), there is restricted diffusion and the signal is unattenuated.

The images in Fig. 2.6 have been windowed and levelled for clarity. The diffusion-weighted images are generally very dark in comparison to the T_2. The eighth image in Fig. 2.6 shows just how "severely compromised" the pure T_2 signal is by diffusion.

A close look at the corpus callosal regions (yellow ellipses) in each slice shows that the diffusion-weighted signal is stronger in some directions than in others: the diffusion is being inhibited in some direction, and is almost free in others—it is *anisotropic*. Despite its resolution of 1.8 × 1.8 mm, the diffusion-weighted image is revealing the presence of the myelinated axons, meaning that the *microscopic* movement of water molecules follows preferentially the direction of the axon alignment, and leads to a macroscopic effect. This is what makes DTI such a powerful tool: it enables the imaging of white matter pathways *in vivo* by comparing the magnitude and direction encoded in the diffusion tensor at each voxel in the volume. The first step in this process is to calculate the diffusion tensor.

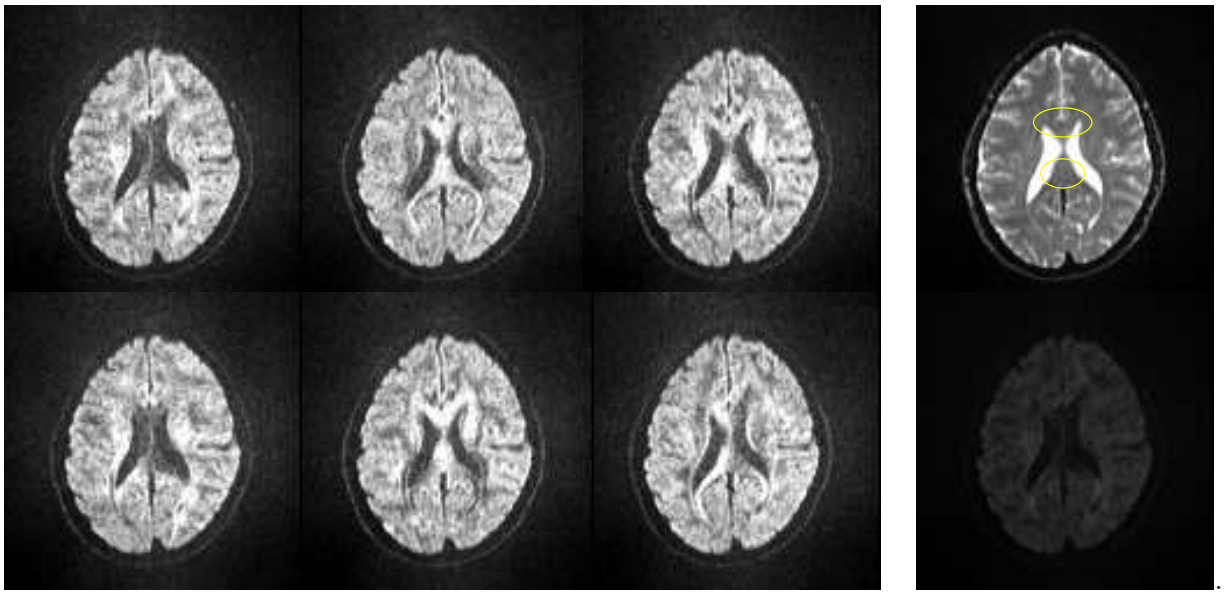

Figure 2.6: **Motion-probing gradient (mpg) directions.** A minimum of 6 mpg directions are required to obtain sufficient directional information to estimate the diffusion tensor. This is due to the fact that diffusion-related attenuation can only be measured along one direction at a time. The figure shows diffusion-weighted images from six different directions and a $b = 0$ image. The yellow ellipses on the T_2 image highlight the ventricles and the medial corpus callosal regions. The eighth image (lower row on the right) is a diffusion-weighted slice with pixel values scaled according to the T_2 image.

2.2.2 White matter tracts as streamlines: the FACT algorithm

Calculation of the diffusion tensor. The problem is first to find the diffusion coefficient along each gradient direction once we have measured the corresponding diffusion-weighted signal, and then to use this directional information to estimate a *best-fit model* of the true diffusion in each voxel. The diffusion tensor model assumes that the true local diffusion may be represented by a 3D Gaussian distribution whose covariance matrix is proportional to the diffusion tensor, $\mathbf{D}$ [15]. This is the simplest model, and the most commonly used. In some parts of the brain, this may not be an anatomically-justifiable model for the true diffusion. This will be discussed further in §2.2.3. The following is a heuristic outline of the application of the method of least squares to the problem of characterising the diffusion in each voxel.

The least squares problem for the system $\mathbf{A}x = \beta$ consists in finding an x that minimises the distance $\|\beta - \mathbf{A}x\|_2$. First, we multiply both sides of the system by $\mathbf{A}^{\mathrm{T}}$ to make it square:

$$\mathbf{A}^{\mathrm{T}}\mathbf{A}x = \mathbf{A}^{\mathrm{T}}\beta. \tag{2.11}$$

This is the fundamental formula for solving least squares problems. We want to couch the diffusion tensor estimation problem in these terms. We can use (2.9) as a guide. If we write it

$$b\mathbf{g}\mathbf{D}\mathbf{g}^{\mathrm{T}} = \ln(S_0/S), \tag{2.12}$$

and (taking a bit of a leap) define

$$b\mathbf{g}\mathbf{g}^{\mathrm{T}} \equiv \mathbf{A}, \qquad s \equiv \ln(S_0/S), \tag{2.13}$$

it is not too hard to discern a least squares problem (using the rule from matrix algebra that says since $\mathbf{A}^{\mathrm{T}}\mathbf{A}$ is square and its determinant will never be 0, it is invertible):

$$d = (\mathbf{A}^{\mathrm{T}}\mathbf{A})^{-1}(\mathbf{A}^{\mathrm{T}}s). \tag{2.14}$$

The vector d is 7×1 and contains the natural logarithm of the raw $b = 0$ signal and the six independent entries of $\mathbf{D}$. For n gradient directions, and $i = 1, \ldots, n$, $\mathbf{A}$ is the $n \times 7$ matrix

$$\mathbf{A} = -b[\mathbf{1} \;\; \mathbf{g}^{\mathrm{T}}\mathbf{g}] = -b[1 \;\; g_x^2 \;\; g_y^2 \;\; g_z^2 \;\; 2g_xg_y \;\; 2g_xg_z \;\; 2g_yg_z]_i, \tag{2.15}$$

while the $n \times 1$ vector s contains the natural logarithm of the actual diffusion-weighted information from each mpg. (Note that the $\mathbf{1}$ in (2.15) is an $n \times 1$ vector of ones, not an identity matrix.)

So far, we have assumed that all measured signals S have the same variance. We incorporate noise by taking $\mathrm{S} \equiv \mathrm{S}_{\mathrm{meas}} = \mathrm{S}_{\mathrm{true}} + \sigma$. Now, since we have worked with $\ln(\mathrm{S}_{\mathrm{meas}})$, there is an uncertainty proportional to $1/\mathrm{S}_{\mathrm{meas}}$. This means that the least-squares fit should give more weight to the ln(S) of high signal values and less weight to the ln(S) of low signal values [50]. It is necessary to account for this variance by incorporating the diagonal weighting matrix $\mathbf{W}$, so that (2.14) becomes

$$d = (\mathbf{A}^{\mathrm{T}}\mathbf{W}\mathbf{A})^{-1}(\mathbf{A}^{\mathrm{T}}\mathbf{W}s). \tag{2.16}$$

This algorithm, with a few refinements (and perhaps with added smoothing or noise correction [25]), can be readily programmed. The result is a diffusion tensor for each (non-zero) voxel in the volume,

$$\mathbf{D} = \begin{bmatrix} d_2 & d_5 & d_6 \\ d_5 & d_3 & d_7 \\ d_6 & d_7 & d_4 \end{bmatrix} = \begin{bmatrix} D_{xx} & D_{xy} & D_{xz} \\ D_{yx} & D_{yy} & D_{yz} \\ D_{zx} & D_{zy} & D_{zz} \end{bmatrix}.$$

Eigenvalue decomposition of the diffusion tensor. The diagonal elements $D_{ij}, i = j$ in $\mathbf{D}$ represent the variance of the diffusion-weighted signals in each of the directions defined by the readout gradients of the scanner. The off-diagonal entries $D_{ij}, i \neq j$ are covariances. In this study, the orientation of tissue structure is obtained from $\mathbf{D}$ by the process of diagonalisation [51]. This parametrises the diffusion tensor as

$$\mathbf{D} = \mathbf{V}\mathbf{\Lambda}\mathbf{V}^{\mathrm{T}}, \tag{2.17}$$

where

$$\mathbf{\Lambda} = \begin{bmatrix} \lambda_1 & 0 & 0 \\ 0 & \lambda_2 & 0 \\ 0 & 0 & \lambda_3 \end{bmatrix} \tag{2.18}$$

is the matrix of eigenvalues of $\mathbf{D}$, and $\mathbf{V}$ is the matrix whose columns are the corresponding eigenvectors. Because of the symmetry of $\mathbf{D}$, the eigenvalues will all be real, and the eigenvectors will form a complete orthogonal set.

The diagonalised diffusion tensor can be represented in 3D as an ellipsoid whose axes are the eigenvectors of $\mathbf{D}$, and whose surface is defined by the eigenvalues, or root mean squared displacement ($\sqrt{2D_it}$, from (2.8)) of the diffusing particles in each of the ellipsoid principal axis directions. Diffusion ellipsoids are shown in Fig. 1.1 and in Fig. 2.8 below.

In the sulci and ventricles, the ellipsoids are relatively large and spherical, representing fast, isotropic diffusion. In regions with more intense background white, e.g. the corpus callosum and the CST, the ellipsoids are smaller, and clearly show a prevailing orientation. In these regions, the diffusion is slow and constrained by the presence of myelin axonal sheaths.

Scalar measures of diffusion anisotropy. There are many invariant quantities that can be extracted from the diffusion tensor, including the trace of $\mathbf{\Lambda}$, $\lambda_1 + \lambda_2 + \lambda_3$), the determinant ($\lambda_1\lambda_2\lambda_3$), and the mean diffusivity $D_{av} = \mathrm{Tr}(\mathbf{\Lambda})/3$ [50]. A mean diffusivity image is shown in Fig. 2.7, second from the left. Of these, the most commonly used is the *fractional anisotropy*, or FA, which is defined as [18]

$$\mathrm{FA} = \sqrt{\frac{3}{2}}\sqrt{\frac{\mathrm{Var}(\mathbf{\Lambda})}{\mathrm{Tr}(\mathbf{\Lambda}^2)}} = \sqrt{\frac{3}{2}}\frac{\sqrt{(\lambda_1 - \langle\lambda\rangle)^2 + (\lambda_2 - \langle\lambda\rangle)^2 + (\lambda_3 - \langle\lambda\rangle)^2}}{\sqrt{\lambda_1^2 + \lambda_2^2 + \lambda_3^2}}. \tag{2.19}$$

The FA should always lie between 0 and 1, but it is sometimes greater in practice due to rounding errors or negative eigenvalues.

An FA map has many applications. For example, an FA map enables the discrimination of white matter pathways even before myelination is evident histologically [52], so it has been used extensively in studies investigating pediatric development (e.g. [53, 54]). The symmetry of mean FA values in ROIs across hemispheres has also been used to quantify sensorimotor tract integrity in stroke recovery studies (e.g. [55, 56, 57]).

To visualise different white matter tracts, it is also useful to colour code each voxel according to the dominant direction of the principal eigenvector. A vector image such as this has three components at each voxel: conventionally, the x component is coloured red, the y green, and the z blue. With intensity scaled according to FA, the resulting RGB image shows anterior-posterior (y) tracts in green, left-right (x) tracts in red, and inferior-superior (z) in blue. An example is shown in Fig. 2.7 on the right, beside a scalar FA map of the same slice.

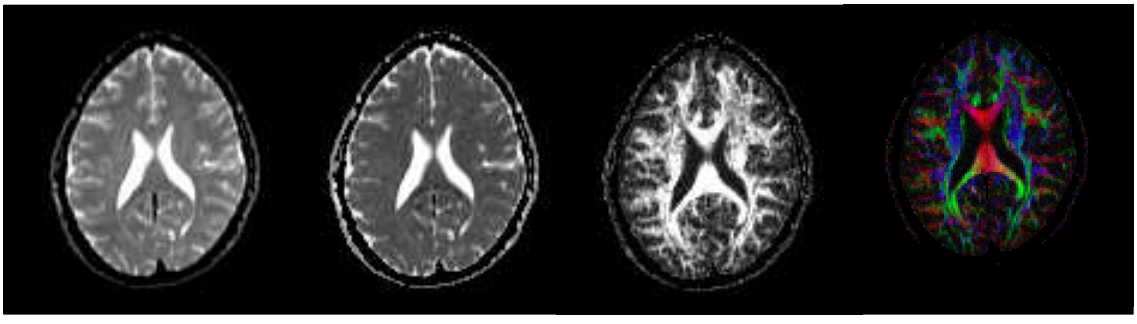

Figure 2.7: **Scalar measures of diffusion anisotropy.** From left to right: T_2 (from Fig. 2.6) for comparison; Mean diffusivity; FA; FA RGB colourmap. Subject ps01.

The FACT algorithm. The reconstruction of white matter pathways *in vivo* by using streamlines through the principal eigenvector field was first achieved by Mori et al. [19].The FACT (fibre assignment by continuous tracking) algorithm interpolates a vector at an

initial seed point from the four nearest neighbouring eigenvectors. Then, taking a small step in the direction of this vector, it asks two questions: first, is the FA at the new point sufficiently high to assume that the new position lies within white matter? and second, is the angle between the vector at this point and the interpolated vector at the next point less than a certain anatomically-reasonable threshold? These are known as stopping criteria, because if the answer to either is no, the algorithm terminates and moves to the next seed point. If the answer is yes to both, the process iterates, tracing with a polyline each step it takes in the direction of the nearest eigenvectors, until a stopping criterion is satisfied. The FA threshold is usually taken to be 0.15–0.2, and angle threshold between 40 and 60°. This process is illustrated in Figure 2.8 for tracing the CSTs.

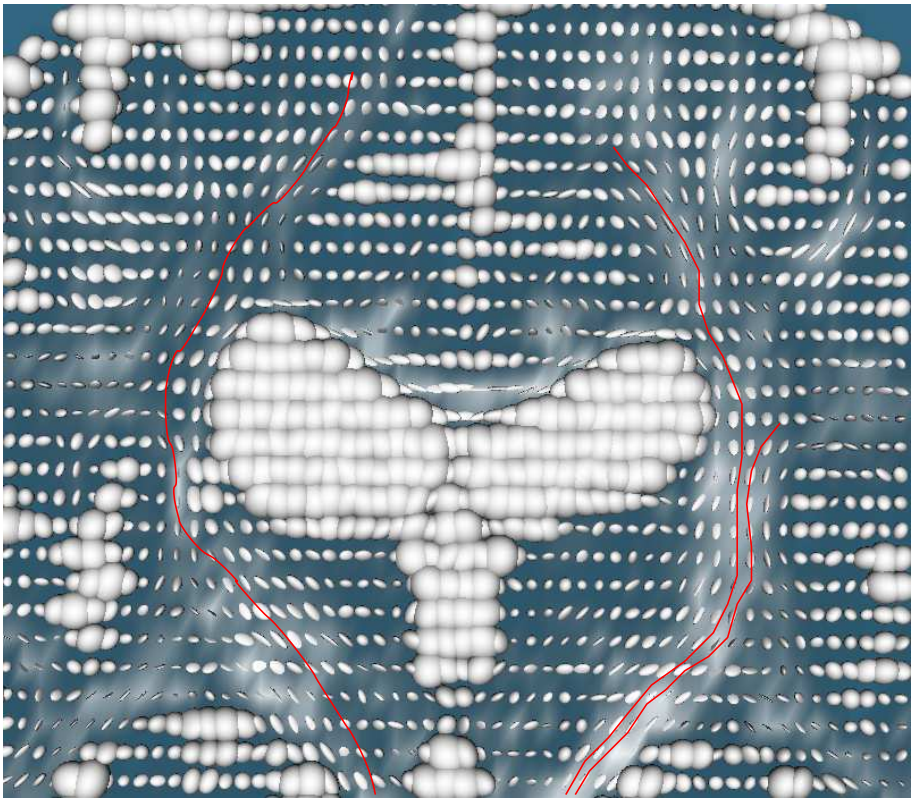

Figure 2.8: **The FACT algorithm for reconstructing white matter pathways.** Seed points lie in the left and right corticospinal tracts at the level of the brainstem (just below the bottom centre of the picture). The algorithm steps through the vector field defined by the principal axes of the diffusion ellipsoids, tracing a streamline at each step until either the FA falls below a specified threshold (represented by a more spherical ellipsoid), or the streamline curves more sharply than is anatomically feasible. White regions represent higher FA. Subject 9. A subcortical stroke lesion is located in the right hemisphere (right of picture), anterior to the coronal slice shown.

The FACT algorithm is very popular and has been used in many applications (e.g. Kunimatsu et al.(2003) [32], Konishi et al. (2005) [29], and Lee et al. (2005) [30]) correlated location of stroke lesion and involvement with CST with clinical symptoms). In regions where there is low uncertainty in the fibre direction, i.e. where the FA is greater than the threshold, it generates fibre traces that correspond to known anatomy. Its authors have recently used it to produce an atlas of white matter in the human brain [33]. It is an example of what have been called *deterministic*, or better, *linear* [51]

tractography algorithms: there is just one reconstructed trajectory for each seed point. That this is a shortcoming is apparent on inspection of the cortical regions in Fig. 2.9. At the superior extent of the sensorimotor tracts, the fibres should branch out to meet the various muscle-group representations of the Penfield homunculus (Figure 2.10). The FACT algorithm can only follow one pathway, and the low FA value at the stopping point of the fibre trace may not represent grey matter, but instead be a consequence of uncertainty in fibre direction. There is uncertainty in fibre direction when they branch and when they cross. Three major fibre tracts—the corpus callosum, corona radiata, and the superior longitudinal fasciculus—cross each other along the superior-lateral margins of the ventricles, for example. When major fibre bundles cross, the trajectory following one path may halt altogether, or be erroneously diverted to follow the other [51]. In Fig. 2.9, the CSTs were traced from a seed ROI in each posterior limb of the internal capsules. Note the single trajectories, none of which approach more lateral cortical regions. In the centre of the picture, the trajectories following the CST toward the cortex are truncated near the intersection with corpus callosum—a region of high uncertainty in fibre direction, and consequent sub-threshold FA. On the other side, and in the right posterior CST, the trajectories dogleg to follow corpus callosum. Note also that streamtubes terminate some way short of the cortex where the FA falls below the threshold of 0.2.

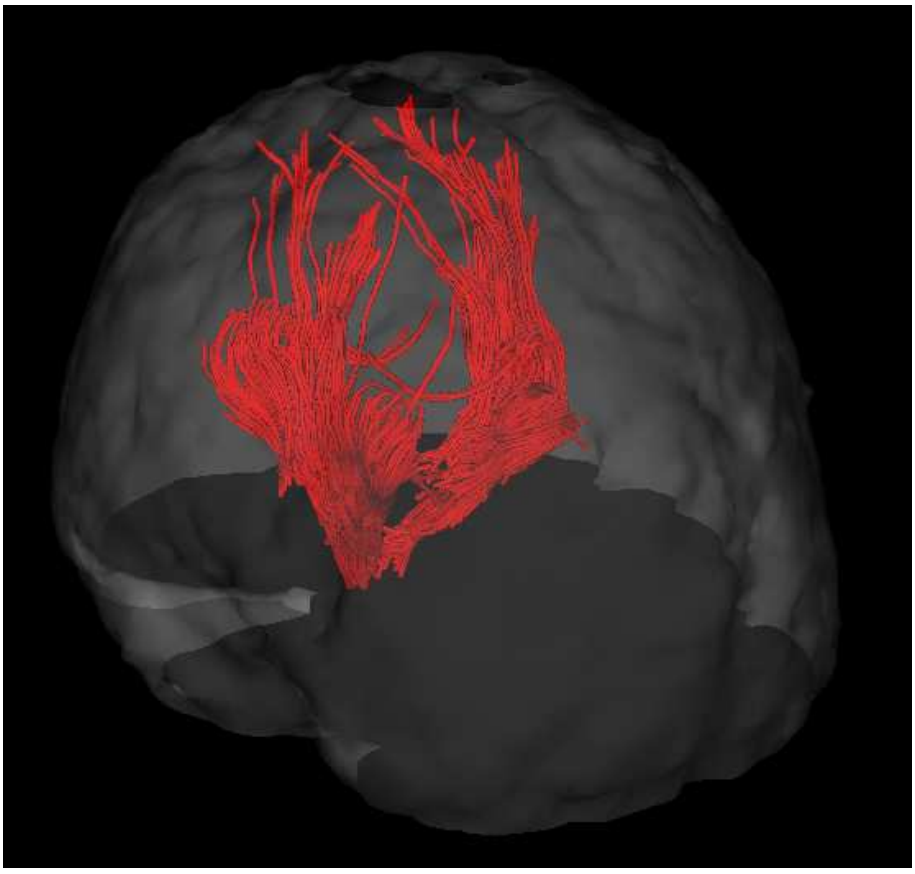

Figure 2.9: **Deterministic diffusion tensor tractography.** The corticospinal tracts, seeded from 2D ROIs drawn on an axial slice in the PLICs, are shown in red. The cortical surface is shown for orientation—anterior in the foreground. Subject ps01. Image produced with DTIStudio/3DMRI (http://lban.med.jhmi.edu)

Another weakness of deterministic algorithms is that there is no quantitative measure of confidence in the likelihood of the location of a pathway, which makes it hard to trace reliable pathways in uncertain areas [15]. *Probabilistic*, or *distributed* algorithms are an attempt to quantify this uncertainty.

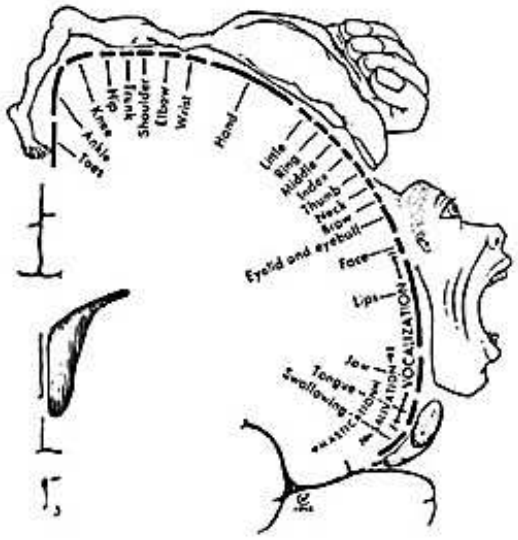

Figure 2.10: **The Penfield homunculus.** This is the diagram produced by Penfield in 1950 of the M1 cortical representations of the various muscle groups. White matter from the CST would branch out superior to the PLICs to reach each representation. Deterministic tractography can take only one path: the line of least uncertainty in the fibre orientation.

2.2.3 Determining uncertainty in DWI: probabilistic tractography

This study concerns itself only with the Monte Carlo methods used in the probabilistic fibre-tracking toolbox FDT (www.fmrib.ox.ac.uk/fsl/). There are other methods (e.g. fast marching tractography [51, 39]). The FSL software is freely downloadable. There is a comprehensive set of tutorials and an active FSL email list. The following outline is drawn mainly from the technical review published in Magnetic Resonance in Medicine in 2003 [15].

Inverse problems. When making predictions about a system, we are grappling with a *forward* problem: we are asking what the probability of obtaining a particular measurement is, given the measurable variables. Tractography is just one example of an *inverse* problem: we already know the answer (the measured diffusion-weighted signal), but we don't know the question (the exact neuroanatomy that gives rise to the measured signal). We can only suggest possible models of the "question" and see how well they fit our "answer".

In fitting our model to the measured data, we get residuals due to the fact that the true diffusion profile is much more complicated than our model. This will generate uncertainty in the model parameters. When we used the method of weighted least squares to calculate the diffusion tensor above, we were effectively *computing* the single model with parameters that fitted the data best according to the least squares metric. We have seen

that this model has its drawbacks. There is a second way of fitting a parametrised model to the data. We can relax our demand for a *single* set of parameters, and instead use a *distribution* of parameter values informed by the data we have measured. The distribution of parameter values is called a *probability distribution function* (pdf), which quantifies the uncertainty in our model parameters. For tractography, this means that rather than saying "this voxel is not connected to this one, because it is connected to that one," we can say, "there are parameter values that indicate that this voxel has a 20% chance of being connected to this voxel, and an 80% chance of being connected to that one."

The pdf is computed using *Bayes' theorem*. With models for both signal and noise, we can determine the likelihood of the data Y given the parameters Ω: $P(Y|\Omega)$. Using Bayes' theorem we can calculate the *posterior* distribution on the parameters given the data—the pdf:

$$P(\Omega|Y) \propto P(Y|\Omega)P(\Omega). \tag{2.20}$$

When computing the diffusion tensor by least squares, the free parameters were chosen to be the six independent tensor entries and the raw $b = 0$ signal S_0. The parameters of interest chosen for the diffusion tensor model in [15] are

$$\Omega = [\theta, \phi, \psi, \lambda_1, \lambda_2, \lambda_3, \mathrm{S}_0, \sigma]; \tag{2.21}$$

the three spherical-polar angles defining the shape and orientation of the diffusion tensor, its three eigenvalues, S_0, and the standard deviation of a zero-mean Gaussian noise model, σ. A pdf is calculated for each of the eight parameters.

In fact, the FDT software uses a different diffusion model. The diffusion in each voxel is modelled as occurring along a single direction, with an isotropic background diffusion [28]. The model signal looks like this:

$$\mathrm{S} = \mathrm{S}_0[(1-f)\exp(-bd) + f\exp(-bd\mathbf{g}_i^{\mathrm{T}}\mathbf{R}\mathbf{A}\mathbf{R}^{\mathrm{T}}\mathbf{g}_i)], \tag{2.22}$$

and the new parameters are the diffusivity d, the fraction of the signal contributed by diffusion along the fiber direction f, the angles (θ, ϕ) determined by the fibre direction, $\mathbf{R}\mathbf{A}\mathbf{R}^{\mathrm{T}}$ (where $\mathbf{R}$ rotates $\mathbf{A}$ to (θ, ϕ)), the $b = 0$ signal S_0, and the Gaussian noise with standard deviation σ. The main reason for using the partial volume model was originally that it maximises the chance that the branching or crossing of fibres will be seen as *uncertainty* in the principle diffusion direction (θ, ϕ), and not, as in the case of the diffusion tensor model, as a change in the diffusion profile, although experimentally there is little to distinguish the two models [15]. Other reasons for using the partial volume model include the fact that it requires estimation of the pdfs on only six parameters, and it is also more modular—it will be easier in future versions of the software to accommodate models incorporating multiple fibre directions.

In practice, (2.20) involves integrals that seldom have analytic solutions. The solution is obtained instead by *Markov Chain Monte Carlo sampling*. This is a technique by which the number distribution of a very large system is estimated by drawing a relatively small number of samples at random. The words of its discoverer, Stan Ulam, give an intuitive feel for the process which is sufficient for our needs:

> The idea for what was later called the Monte Carlo method occurred to me when I was playing solitaire during my illness. I noticed that it may be much more practical to get an idea of the probability of the successful outcome of a

> solitaire game [...] by laying down the cards, or experimenting with the process and merely noticing what proportion comes out successfully, rather than try to compute all the combinatorial possibilities which are an exponentially increasing number so great that, except in very elementary cases, there may be no way to estimate it. [...] In a sufficiently complicated problem, actual sampling is better than an examination of all the chains of possibilities ([58], p 197).

Using Monte Carlo sampling to compute a voxelwise pdf from the diffusion signal and noise models given the data takes about 9 hours on a single Pentium processor.

With an accurate pdf at each voxel, it is possible to obtain the probability of anatomical connection between any two voxels. This requires a computation of a *global* pdf, this time based on a model of global connectivity. The FDT model takes into account every possible fibre direction (θ, ϕ) at every voxel, calculating the probability of connection given this, and also the probability of this orientation given the data. This again involves intractable integrals, but, once again, the integrals can be solved implicitly by a sampling method. This time, from a given seed point z, a random sample (θ, ϕ) is selected from the posterior distribution on the orientation given the data, a step is taken in the direction of (θ, ϕ), and this is repeated until the stopping criterion is met. This is repeated many times for each z. The probability that a certain voxel A is connected to another voxel B can be represented simply as the number of probabilistic streamlines so generated which pass through A.

The main advantage of the probabilistic algorithm is that where the deterministic algorithm may be diverted by noise or stop altogether where there is significant uncertainty in fibre direction, the probabilistic algorithm can continue in *all* directions, representing an uncertain path by associating lower probabilities with voxels further along that path. This means that FDT can be run with no FA threshold stopping criterion, and a curvature threshold of $\pm 80^\circ$ just to prevent streamlines doubling back on themselves and thereby artificially increasing their likelihood.

The outcome of the FDT probabilistic tracography algorithm ProbTrack is a volume whose voxel intensities are scaled according to their likelihood of connection to the input seed. In Figure 2.11, the seed mask was the whole of the fMRI activation for each hand. The strongest connectivity is shown in yellow. Because the confidence bounds on the connectivity within the activations are so much higher than those on the connectivity down the CST, the connectivity scale has been converted to a logarithmic scale. Note the displacement of the connected white matter in the region of the lesion (green arrow).

2.2.4 How many motion-probing gradient directions?

A minimum of 6 mpg directions is required to obtain sufficient 3D information to perform tractography. Clearly though, there will be considerable uncertainty in the ability of such a diffusion-weighted scheme to adequately represent the white matter oriented in other directions—more directions would be better. Since it takes time to scan along more directions, there is a practical trade-off between directional resolution and patient comfort. The current study used 12 mpg directions. Many studies use 25–30 directions. The FSL documentation recommends that for probabilistic tractography the diffusion-weighted dataset should be obtained from not less than 25 diffusion-encoding directions [28]. There are two studies in particular that address this issue.

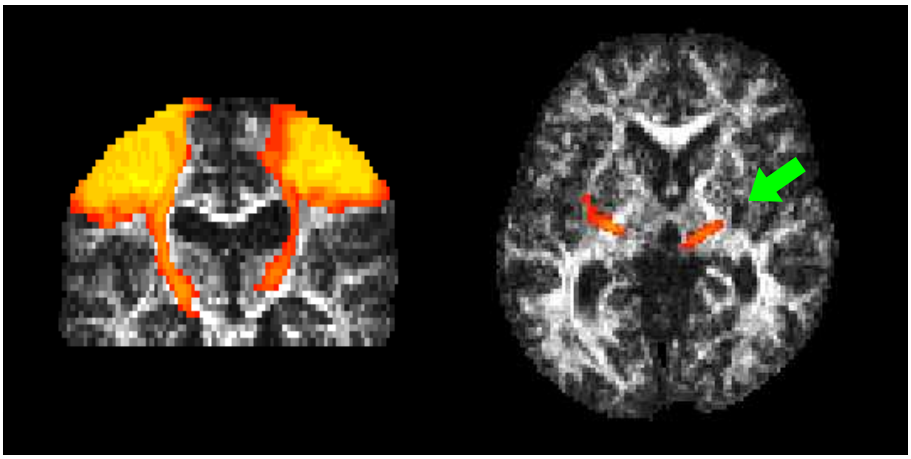

Figure 2.11: **FDT Probabilistic estimation of white matter pathways.** The fMRI activations for each hand were used as seed masks, and the probabilistic tractography algorithm ProbTrack computed the likelihood of a connection existing between each voxel in the seedmasks and every other voxel in the brain. Subject 9.

Jones [59] used Monte Carlo methods to characterise the uncertainty in diffusion tensor information from 6, 10, 12, 15, 20, and 30 directions. The uncertainty in the spherical-polar coordinate angles θ and ϕ is represented by a 95% confidence angle which narrows with more directions[2]. He describes the confidence angle response surface, i.e. the surface spanned by θ and ϕ, as being deformed like a rubber sheet under the pressure of a finger. With only 6 directions, the surface bulges up (the 95% confidence angle broadens) between the direction vectors (Figure 2.12(a)). With more directions, the surface cannot bulge so much between the vectors (Figures 2.12(b) and 2.12(c)). Figure 2.12(b) shows that with 12 directions, there is more uncertainty in the z direction, and also in two directions in the xz plane where $x = \pm 1$ and $z = 1$ (see Figure 2.13). For a person lying in the scanner reference frame, these last two directions coincide quite well with the corticospinal fibres descending from the hand cortical representations.

A study by Heiervang [60] compared results from 60 directions with those from 12 directions and found that tracts derived using fewer directions were smaller, and concluded that for defining the cores of larger fibre bundles, 12 directions would be sufficient, but more directions are needed to define smaller pathways. Anatomically reasonable results have been obtained for healthy subjects using 12 [61] and 15 [62] directions.

From the above considerations, it seems reasonable to expect to be able to do probabilistic tractography on twelve-direction data, but to keep in mind that it may be underestimating the tract volumes and missing smaller tracts. It is unfortunate that the axes of maximum uncertainty correspond to the orientations of the pathways we will be interested in. Communications on the FSL list suggest that the documentation on the FSL webpage will be updated [41].

[2]Here, θ is the angle the radial coordinate vector makes with the z axis, and ϕ is the angle it makes with the x axis.

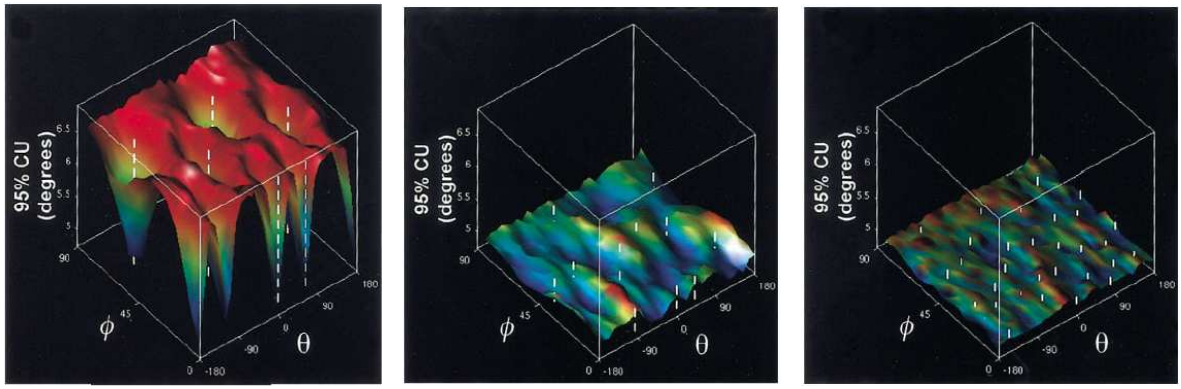

(a) 6 directions (b) 12 directions (c) 30 directions

Figure 2.12: Increasing the number of diffusion-sensitive gradient directions decreases the 95% confidence angle. See text for details. Source: Jones (2004) [59]

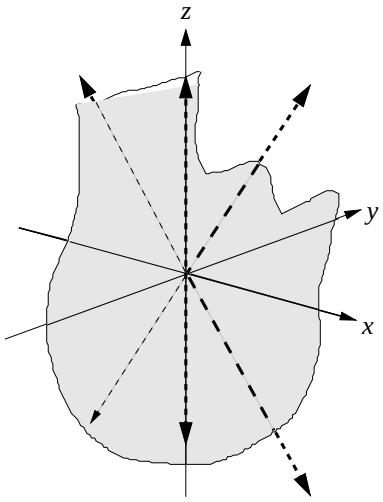

Figure 2.13: Directions of maximum uncertainty, shown as dotted arrows, in a DWI scan based on 12 directions isotropically distributed over a spherical surface (from the data in Fig. 2.12(b)). For a person lying in the scanner reference frame, the lateral axes of uncertainty coincide with the orientations of the hand fibres.

2.2.5 Diffusion tractography in stroke.

Stroke results in a lesion which by the chronic stage has become a CSF-filled cavity with correspondingly low FA. Since probabilistic tractography is capable of tracing connections through regions of low FA, it makes sense to apply probabilistic methods to the problem of assessing the lesion involvement with corticospinal tracts. From seed masks defined by the fMRI activations, one would expect delineation of all those CSTs required to perform the hand squeezing task in the healthy hemisphere. In the lesioned hemisphere, connectivity will depend on the extent of lesion involvement with the CST. The results of this analysis are presented in Chapter 4.

Chapter 3

Methods

3.1 Obtaining the data

Data were collected from 28 subjects who had suffered their first stroke not less than 6 months prior to assessment. Collection took place in six stages:

1. Clinical assessment
2. MRI (fMRI and DTI)
3. Laboratory assessment
4. Movement therapy
5. MRI (fMRI only)
6. Final assessment

3.1.1 Clinical assessment

Patient disability was assessed by an independent clinician, blinded to patient group allocation, using the National Institute of Health Stroke Scale (NIHSS) and the upper limb part of the Fugl-Meyer (FM) scale. The FM scale assigns a number between 1 and 32 to upper limb function, with smaller numbers representing poorer function. The clinical assessment was repeated after one month.

3.1.2 MRI

MRI data were acquired from the Siemens Magnetom Avanto 1.5 T MRI system at the Centre for Advanced MRI (CAMRI), Grafton, Auckland. T_1-weighted images were acquired with a 3D MPRAGE sequence (TR = 11 ms, TE = 4.94 ms, FOV = 256 mm and voxel dimensions of 1.0×1.0×1.0 mm). T_2-weighted 2D axial images were also acquired (TR = 3860 ms, TE = 89 ms, FOV = 230 mm, voxel dimensions = 0.6 mm×0.4 mm×5.0 mm). Blood oxygen level-dependent contrast images were acquired using a $T_2^\star$-weighted single-shot gradient echo EPI sequence (TR = 2570 ms, TE = 50 ms, FOV = 192 mm, voxel dimensions = 3.0×3.0×3.0 mm). DWI were obtained using a single shot spin echo EPI pulse sequence (TR = 4800 ms, TE = 88 ms) with 12 uniformly distributed Stejskal-Tanner motion-probing gradient orientations (b = 1000 s/mm^2). Four image volumes were taken along each gradient orientation, and these were averaged to increase the signal-to-noise ratio. The FOV was 230 mm, with voxel dimensions of 1.8×1.8×3.0 mm. Both fMRI and DWI sequences were obtained in the same session, taking about 40 min.

The motor task Patients in the scanner held a saline drip bag connected to a transducer in each hand. On cues projected on to a screen visible in a mirror from inside the scanner, the subjects opened and closed their hands on the saline bags for 30 seconds

Figure 3.1: **Active-passive bimanual therapy (APBT).** The paddles on the desk top are mechanically linked so that movement by the strong hand can drive the same movement in the weak hand.

according to four conditions: right hand only, left hand only, bimanual, or rest. There were four runs of two minutes duration.

3.1.3 Laboratory assessment

Motor connectivity was assessed in the lab using single pulse TMS. Motor evoked potentials were recorded from electrodes on the extensor carpi radialis muscle of each forearm. In some subjects, no MEPs could be elicited from the stroke-affected limb, whether the target muscle remained at rest or was voluntarily contracted, even at the maximum (100%) stimulator output.

3.1.4 Movement therapy

Subjects were divided into an APBT group and a task-only group. All subjects performed the task, which involved the placement of variously-shaped blocks with the affected hand. Subjects in the APBT group were provided with an APBT unit (see Fig. 3.1). This is a desktop-mounted device with two vertical paddles mechanically linked to each other. With both hands strapped to the paddles, movement of the strong hand drives the same movement of the weak hand. APBT patients were asked to use this device for 15 minutes at a time, three times a day, followed by ten minutes of the block task, for four weeks. The aim of this procedure was to test the hypothesis that APBT establishes a neurophysiological context that is more receptive to the plastic changes instigated by the block motor task.

3.1.5 MRI

The second MRI session involved acquisition of a second, post-therapy, fMRI dataset based on the same task and using the same protocol as the first. No other scans were acquired.

3.1.6 Final assessment

After a month of movement therapy, the clinical assessment, and TMS were repeated. The clinical assessment and TMS were repeated after one further month.

3.2 Data processing

3.2.1 SPM and FMRI

Nine of the 32 subjects in the study were selected for SPM/DTI analysis based on their activation of ipsilesional hemisphere during the performance of the motor task with the affected hand. The reason for this was that the activations would be used as seed masks in the probabilistic tractography.

Functional data were analysed using SPM2 [64]. Data were corrected for slice timing, then realigned to the first image from the first run. The images were then unwarped to correct for EPI distortion. They were then coregistered and resliced using the $b = 0$ (no diffusion weighting) volume from the DWI dataset as a template. The aim was to transform the fMRI activations into the diffusion space so that they could be used as seed masks for the tractography. The reason for choosing the T_2 template in particular was that the $T_2^\star$ functional scans are more similar to the pure T_2 diffusion volume, having bright CSF. After coregistration, the data were smoothed using a 3D 7 mm Gaussian kernel.

The three conditions were modeled by a box-car function convolved with a canonical hemodynamic response function. Voxels were considered active if they had a positive t score corresponding to a p value corrected for a familywise error (FWE) of no more than 0.01. The appropriate sensorimotor cortical activation was then excised and binarised using the avwmaths command line tools in the FSL package, to be used in the tractography analysis.

3.2.2 DWI processing

The DWI dataset was converted into a 4D Analyze format .hdr/.img pair. Calculation of the volume of diffusion tensors was achieved using MATLAB by the process described in §2.2.2.

For typical axial oblique anterior commissure-posterior commissure (AC-PC) aligned imaging, the patient image orientation is rotated relative to the scanner reference frame, while the diffusion gradients are locked to the scanner reference frame. On Siemens scanners, it is therefore necessary to rotate the gradient vector components into the patient reference frame to obtain the correct directional information from the diffusion data (Figure 3.2). In the DICOM header of the diffusion images produced by the scanner, there is an entry "Image Orientation Patient" (0020 0037) which contains six numbers. These are the first two direction cosines of the radiographer's rotation of the field of view relative to the scanner frame. The third direction cosine is obtained from the cross product of these first two. These three vectors form the rows of the matrix that rotates the gradient vector from the scanner frame to the patient image frame [65]. A small Matlab script read the DICOM header and produced the required transformations.

Analyze volumes were produced of the mean diffusivity, the fractional anisotropy, the eigenvalues and the components of the principle eigenvectors at each voxel, and the

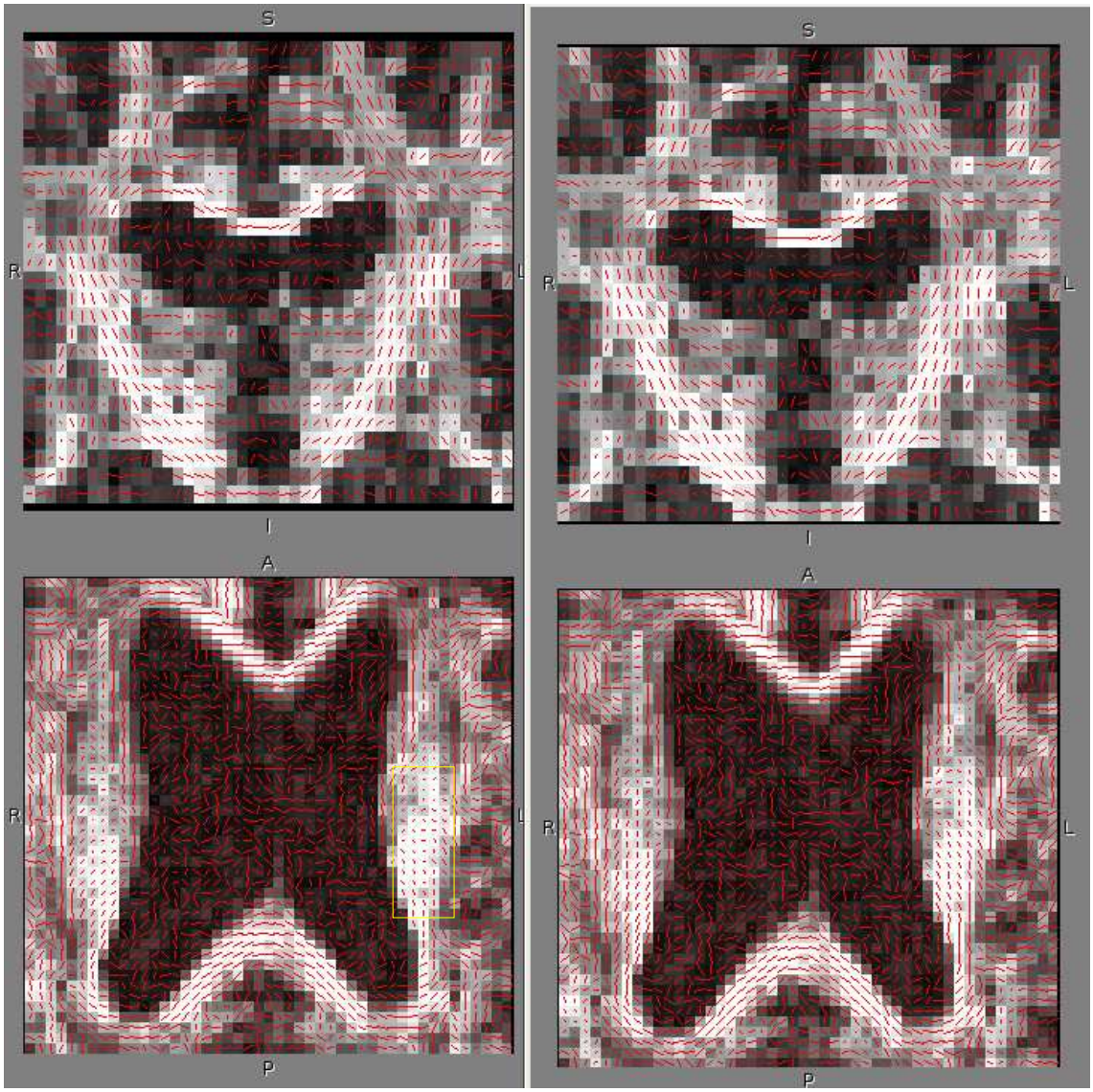

Figure 3.2: **Principle eigenvectors of the diffusion tensor (coronal and axial projections).** The left two frames show the eigenvectors corrected for the patient image orientation. In the right two frames, no correction has been applied. Note, for example, the more vertical eigenvectors in the PLICs (marked by yellow square) in the corrected images. The difference is subtle, but it is of vital importance for computing connectivity. This is subject 4.

components of the diffusion tensor at each voxel. Also using Matlab, RGB vector colour FA maps were produced. The m-files are included in Appendix D.

Obtaining FA asymmetry Using MRIcro (www.sph.sc.edu/comd/rorden/mricro.html), and with reference to the RGB FA maps, a region of interest was drawn over the posterior limb of each internal capsule (PLIC). The PLICs were taken to be bounded superiorly at the slice in which the most superior parts of the basal ganglia disappeared; inferiorly at the slice above that in which the anterior commissure was visible; anteriorly by a line across the genu of the internal capsule; and posteriorly by a line joining the most posterior aspects of the thalamus and the putamen/globus pallidus (see Fig. 3.3).

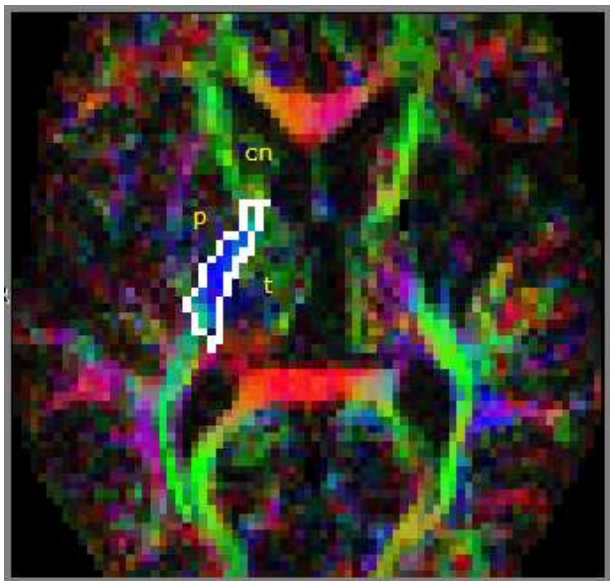

Figure 3.3: **Defining the posterior limb of the internal capsule (PLIC).** The outline was drawn in MRIcro. The anterior limb of the IC is the green area between the caudate nucleus (cn) and the putamen/globus pallidus (p). The external capsule is visible as the purple arc linking the ALIC and the PLIC. t = thalamus. Subject 3. Note the relatively vague corresponding PLIC on the opposite (lesioned) side.

Defining PLIC regions of interest This method for defining the PLICs runs into difficulties in those subjects with significant lesion involvement in the PLIC. Then, inferring the PLIC boundary with reference to the opposite PLIC can be rather subjective because the FA values are more uniformly low. Unlike in the contralesional hemisphere, some threshold FA intensity cannot be used to define the PLIC boundaries. This difficulty was overcome by defining PLIC ROIs in standard MNI space using MRIcro as described above. The standard PLIC ROIs can then be transformed into the individual's diffusion space and used as masks over the FA volume. As well as delineating the sample population of voxels for determining FA asymmetry, the PLIC ROIs thus defined will be used as seed masks in the for probabilistic tractography and connectivity mapping.

Corticospinal tract integrity The posterior limbs of the internal capsules were chosen for the measurements of the FA statistics because all the main motor pathways descend through these regions.

The ROI tool in MRIcro can produce statistics for a given ROI. From the mean FA value in each PLIC, the FA asymmetry was calculated as

$$\frac{|\langle \mathrm{FA}_{\mathrm{left}} \rangle - \langle \mathrm{FA}_{\mathrm{right}} \rangle|}{\langle \mathrm{FA}_{\mathrm{left}} \rangle + \langle \mathrm{FA}_{\mathrm{right}} \rangle}, \tag{3.1}$$

where the angled brackets signify means. By this measure, a healthy PLIC would score close to zero, while a lesioned PLIC would score closer to one.

The results of the assessment of PLIC asymmetry are summarised in Chapter 4.1.

3.2.3 The FSL pipeline

BET, DTIfit, BEDPOST, and ProbTrack FSL has its own program, called DTIfit, for calculating the diffusion tensors. It requires as input a text file listing the b values for each gradient direction, a text file listing the unit gradient directions (corrected for the image plane rotation relative to the scanner frame), a skull-stripped T_2 image, and the diffusion-weighted dataset. BET, FSL's brain extraction tool, was used to skull-strip the T_2 image. Diffusion tensors were estimated using DTIfit. This is not necessary to run BEDPOST (Bayesian estimation of diffusion parameters obtained using sampling techniques), but it provided a check for the Matlab analysis.

BEDPOST generates seven volumes of statistical information: 3D volumes of mean values for the FA and the spherical polar coordinates θ and ϕ; merged 4D volumes of samples from the distributions on the FA, θ, and ϕ; and a volume of vectors representing the mean of the principal diffusion directions distributions at each voxel.

The dataset is now ready for probabilistic tractography with ProbTrack. A GUI prompts the user for the BEDPOST directory, and offers menus for specifying the seeds/seed masks and targets. ProbTrack runs 5000 paths from each seed, assigning a one to each voxel that lies on one of these paths, and a zero otherwise. In this way, for a single seed voxel, a number between zero and 5000 is assigned to every other voxel in the volume; for a seed mask, the number of connections from each of the seed voxels is summed, so the total connectivity is proportional to the size of the seed mask.

First in this analysis, ProbTrack was used to compute the connectivity between the coregistered standard PLICs and the pre- and post- fMRI activations, as well as a group level pair of standard fMRI activations obtained using SPM. Second, Probtrack was used to generate connectivity maps of each PLIC, resulting in a PLIC ROI colourmapped according to the likelihood of its connection to each of the ipsilateral fMRI activations.

FSL is linux-based, which makes it easy to write scripts for processing the data from many subjects. A script for the FSL pipeline from brain extraction to estimation of diffusion parameters is shown in Appendix C.

The results from FSL are summarised in §4.3.

Chapter 4

Results

Some imaging results and clinical assessment results are included for all 28 participants in the MNL stroke study in Appendix A.

The results of assessment of corticospinal integrity using FA asymmetry in the PLICs are described in §4.1. The fMRI results are described in §4.2. The probabilistic tractography took place in two stages. First, each fMRI activation was used as a seed mask, and the connectivity was computed between it and every other voxel in the brain—no target was specified. These results are summarised in §4.3.1. Second, each PLIC ROI was used as a seed mask, and the pre- and post- ipsilateral activations were specified as target masks. Each voxel in the PLIC was assigned a number depending on the likelihood of its connectivity to each activation. These results are summarised in §4.3.2.

4.1 FA asymmetry as a predictor of functional recovery in patients with no MEPs

The results of assessing the PLIC asymmetry using (3.1) are summarised in Table 4.1 below. Only the results for the subjects for whom probabilistic tractography was carried out are shown here. Also included in the table are the change in clinical scores between the second pre-therapy assessments and the first post-therapy assessments (ΔFM_1); the change between the second pre- assessments and the second post-therapy assessments (ΔFM_2); whether the patient produced motor evoked potentials (MEPs); and whether the patient was part of the APBT + Task group (APBT). The reason for taking the two FM differences separately is that some subjects continued to exhibit functional improvement after the first assessment. A representative T_1 anatomical image is shown beside each to give an indication of lesion size and location. WBV stands for whole brain volume. WBV was calculated by binarising the skull-stripped T_2 volume and counting the nonzero voxels. The column labelled FAA* shows the FA asymmetry calculated from a pair of PLICs drawn by hand in standard space coregistered to that of the individual. The FAA* values conform to the FAA values to within 5% (Pearson correlation test).

The FA asymmetry was plotted against the change in the Fugl-Meyer clinical score for all participants. The results are shown in Figure 4.1 below, with data points separated according to whether they produced MEPs. In Fig. 4.1(a), the change in FM score is the difference between the pre-therapy FM score and the first post-therapy FM score. In Fig. 4.1(b), the change in FM score is the difference between the pre-therapy FM score and the second post-therapy FM score.

As might be expected, patients with FAA scores closer to zero (more symmetrical CST integrity) tended to show greater improvement in their clinical score than those with FAA scores closer to 0.5, regardless of whether they produced MEPs or not. In each case, the relationship between FAA and change in FM score is stronger for those patients

T_1	Subject	Lesion	WBV	FAA	FAA*	ΔFM_1	ΔFM_2	MEP	APBT
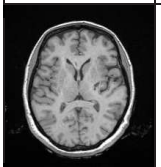	1	R subcort.	122285	0.151	0.066	3	3	0	1
	2	L cort.	128430	0.337	0.185	0	-1	0	1
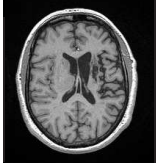	3	R subcort.	146532	0.206	0.204	3	4	1	0
	4	R subcort.	153472	0.008	0.021	4	5	1	0
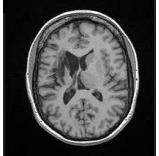	5	L subcort.	127423	0.179	0.167	5	6	1	1
	6	L cort.	133032	0.050	0.081	2	3	1	0
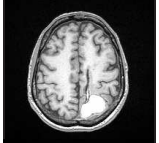	7	R cort.	131468	0.021	0.001	0	2	1	0
	8	R subcort.	151926	0.054	0.097	1	1	1	1
	9	R subcort.	160862	0.060	0.046	2	4	1	0

Table 4.1: FA asymmetry results and clinical data for selected patients. FAA = Fractional Anisotropy asymmetry (manual ROI); FAA* = Fractional Anisotropy asymmetry (coregistered to diffusion images from ROIs in standard space); ΔFM_x = the difference in FM score between the second pre-intervention clinical FM assessment and the xth (first or second) post-intervention assessment; MEP = Motor Evoked Potential (1 = MEP produced, 0 = No MEP); APBT = Active Passive Bimanual Therapy (1 = APBT + Task, 0 = Task only).

who produced no MEPs than it is for those who did produce MEPs. This is in keeping with recently published results that found FA asymmetry to be a stronger predictor of functional recovery in patients with no MEPs [57].

4.2 SPM Results

Table 4.2 below shows the squeezing frequency recorded from the saline bags during the fMRI task. All patients were able to perform the task to some degree. The point of this table is simply to give some idea of the physical performance of the task for each patient—to be kept in mind when looking at the fMRI activations.

Subject	Pre (Hz)		Post (Hz)	
	Unaffected	Affected	Unaffected	Affected
1	1.7	1.0	2.3	1.3
2	1.0	0.5	1.1	0.6
3	0.3	0.3	0.3	0.3
4	1.4	1.4	1.2	1.0
5	1.0	0.9	0.9	0.8
6	1.4	1.6	1.3	1.4
7	0.4	0.5	0.7	0.6
8	1.0	0.9	0.7	0.6
9	0.4	0.4	0.5	0.4

Table 4.2: fMRI squeezing frequencies for each hand for selected patients.

Representative slices showing the raw functional activations produced by SPM2 from the left hand task and the right hand task have been superimposed and are shown for each of the nine selected participants in Figure 4.2(a)–(i). All images are in "neurological" orientation (i.e. image left is patient left). White stars mark the lesioned hemispheres. The activations have been transformed into the diffusion space, and they are shown here superimposed on T_1 anatomical images that have also been coregistered with the diffusion images. Voxels with a positive t-value corresponding to a p value corrected for a familywise error of 0.01 were considered active in each case. Activations from before therapeutic intervention are shown in orange, and those from after are shown in blue.

In each case, the volumes of the motor-cortical activations (where present) were recorded by using the avwstats tool in FSL to count the voxels in the excised, binarised activation image.

The combined volumetric information from the fMRI activations is shown in Figure 4.3. In every case, the volume of the ipsilesional activation increased following the APBT intervention. In six of the nine subjects, the contralesional activation decreased in volume. If they can be correlated with functional recovery, these neurophysiological results will corroborate the idea posited in Chapter 1, that recovery of motor function is associated with the extent to which the original symmetrical physiology can be regained within the constraints of the post-stroke functioning anatomy [2, 5]. By this criterion, patient 8 is a prime candidate for significant functional recovery (see Fig. 4.2(h)). In at least two of those patients whose contralesional post- activations increased (patients 2 and 4), there is evidence (ipsilateral activations pre- or post- when using the affected hand) to suggest that they are using the contralesional motor system during affected hand movements. and

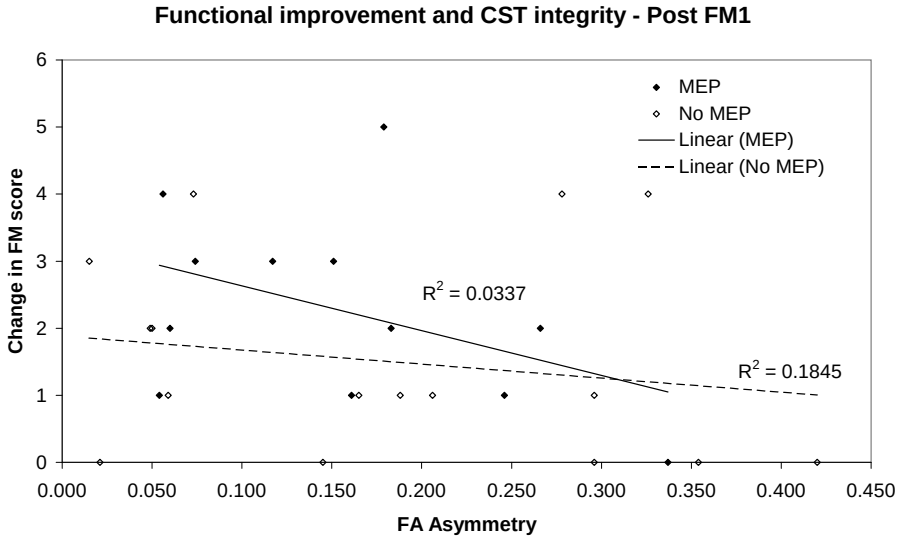

(a) ΔFM_1 vs FA asymmetry: Change in clinical score after first post-therapy assessment.

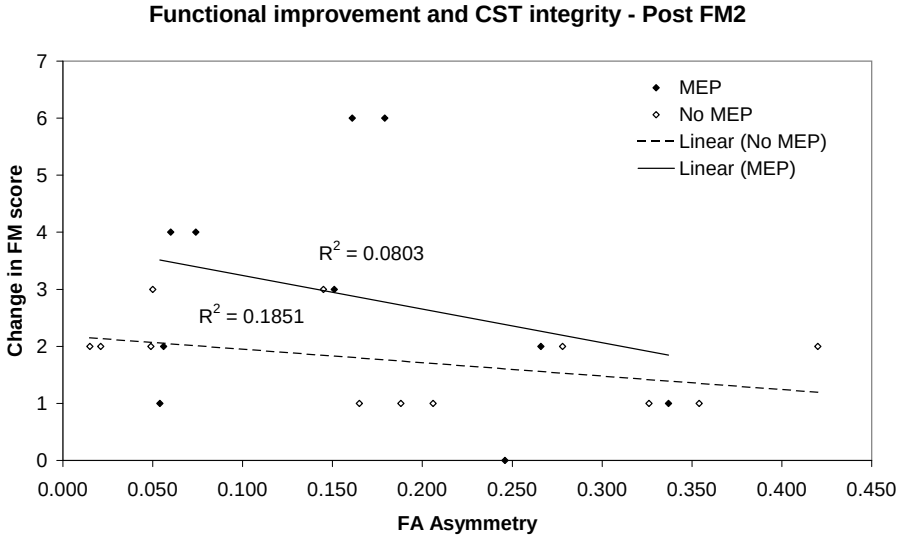

(b) ΔFM_2 vs FA asymmetry: Change in clinical score after second post-therapy assessment.

Figure 4.1: Functional improvement and CST integrity.

thereby compromising the possible benefits of the intervention to the lesioned hemisphere. In Figure 4.3(b), the change in total activation size has been plotted against the change in FM score. The quantity representing change in total activation size embodies the idea of hemispheric rebalancing:

$$\Delta = k(I_{\text{post}} - I_{\text{pre}} + C_{\text{pre}} - C_{\text{post}}), \tag{4.1}$$

where I and C are the pre- and post-therapy ipsilateral and pre- and post-therapy contralateral activations respectively. k is a weighting factor calculated from the WBV that compensates for different brain sizes. Δ will be larger for those patients in whom ipsilesional activations increased in size *and* contralesional activations decreased in size. The plot shows no significant correlation between hemispheric rebalancing as measured by activation volume change and functional recovery as measured by the change in FM score. This seems surprising, but it may be a consequence of the small sample size.

4.3 Connectivity mapping

The Analyze-format output images were thresholded, and the motor cortical activations excised and binarised using the avwmaths command line utility in FSL. Two sets of data were obtained: First, the activations, having been coregistered with the FA volume, were used as seed masks to investigate connectivity between the motor cortices and the brainstem; second, maps of connectivity between the PLICs and the ipslateral activations were generated in the PLIC ROIs, in order to assess movement of the voxels with the maximum connectivity within the PLIC from pre- to post-therapy.

4.3.1 Connectivity from fMRI activation seed masks

In FSL's probabilistic tractography algorithm ProbTrack, connectivity between two voxels is measured as the number of paths out of 5000 leaving the seed voxel that reach the target voxel. Connectivity distributions from multiple seeds are summed. The connectivity therefore depends on the size of the seed mask. In Figures 4.4(a)–(i), each nonzero voxel is coloured according to the sum of all the paths from every voxel in the seed mask. Most of the voxels in the volume have zero connectivity. Figure 4.5 shows a histogram of connectivity values from the right post- activation in subject 1. The connectivity ranges from one to about 10^4. There are relatively high numbers of voxels with very low ($<$ 30) connectivity, so voxel numbers are shown on a log scale. This distribution affects the mean connectivity values—these range roughly from 20 to 400.

Figure 4.4(a)–(i) show representative slices from the results of the application of the ProbTrack algorithm between the fMRI activations and every other voxel in the brain. The resulting images have been thresholded at 10% of the mean connectivity. Logarithmic scaling has been applied to bring out the contrast in the motor tracts, where the connectivity values are small compared to those within the activations themselves.

As expected from the fact that the volume of the activations has increased, the mean connectivity in the ipsilesional hemisphere also increased in every patient (see Fig. 4.6). The mean connectivity in the contralesional hemisphere decreased in 5 of the 9 patients. This coincides with the decreased contralesional activation size except in the case of subject 8.

The mean connectivity values from each activation were recorded and inserted into (4.1) in place of the activation volumes, to compare with the change in FM score. The results are shown in Figure 4.6(b).

The R^2 value shows that about 30% of the variance in the change in clinical score can be explained by the rebalancing of connectivity. This corresponds to a Pearson correlation coefficient of +0.5. This was unexpected, considering the lack of any correlation between activation changes and functional improvement shown in Fig. 4.3(b). The change in connectivity reflects the shifting/dilation/contraction of the seed masks, since the same single volume of pdfs is used for each tractography run. Why is there a stronger correlation between connectivity change so measured and functional recovery than between activation volume change and functional recovery? Figures 4.3(b) and 4.6(b) suggest that those patients who made the greatest improvements were not necessarily those whose activation volumes became more symmetrical; more precisely, they were those whose activation changes resulted in the recovery of more symmetrical motor connectivity. There is further discussion in §5.2.

4.3.2 PLIC ROI Connectivity maps

The PLIC connectivity maps are shown in Figure 4.7. In each case, an axial slice showing the voxels with the best connectivity has been chosen. Patient 8 is not shown, because the tractography from the activations showed that there was no connectivity to either PLIC.

The locations of the voxels with maximum connectivity to the PLIC in the contralesional hemispheres are consistent with the M1 locations in published internal capsule maps [43], and with previous studies of motor somatotopy in the PLIC [42]. These locations were consistent for both pre- and post- activations on the contralesional side.

Internal capsule connectivity results for the ipsilesional hemisphere were highly variable. Patients 1 and 2 showed no ipsilesional connectivity to the internal capsules, consistent with the fact that neither gave MEPs on that side. Neither 3 or 4 showed any PLIC connectivity on the lesioned side, despite producing MEPs. Patients 6, 7, and 9 gave the most consistent results, showing reduced connectivity on the lesioned side that changed little after therapy.

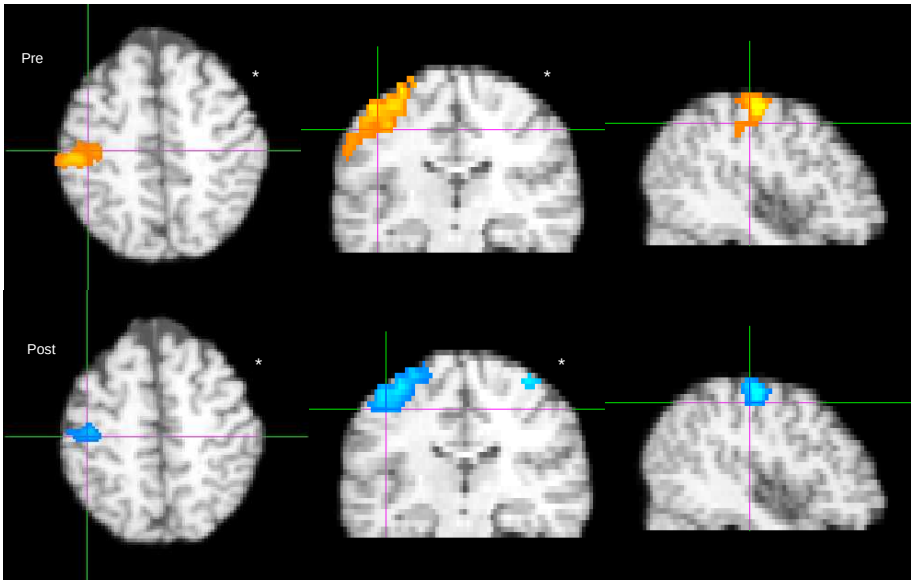

(a) **Patient 1:** fMRI activations (hand-squeezing task). Clean activations were observed in the left (contralesional) motor cortex. There were no significant activations in the ipsilesional motor cortex prior to therapy, but a small significant activation was observed after. Activation volume dropped from 759 voxels before, to 508 after in the contralesional hemisphere. Ipsilesional motor activation volume rose from zero to 37 voxels. $\Delta FM_2 = 3$.

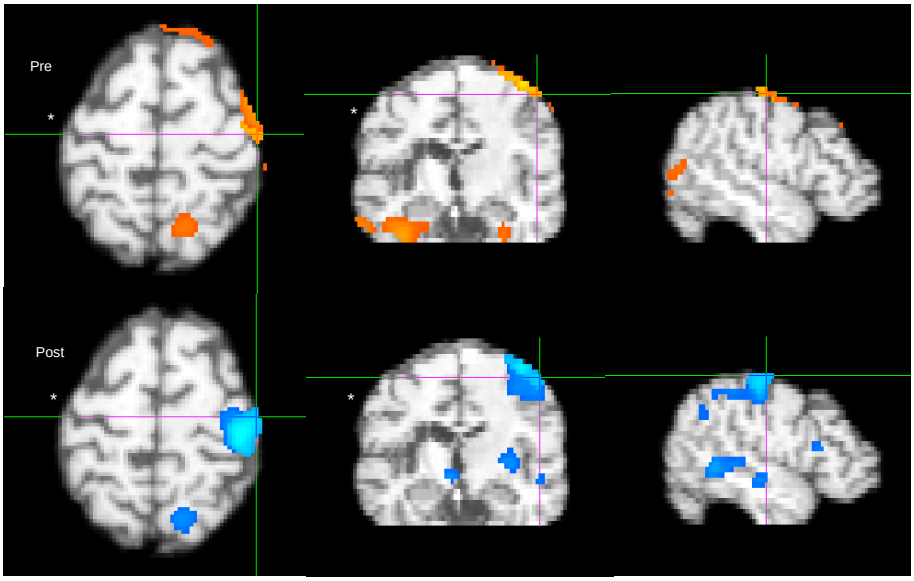

(b) **Patient 2:** fMRI activations (hand-squeezing task). There were clean motor activations before and after therapy in the contralesional (right) hemisphere, but no significant activations were observed in the ipsilesional hemisphere either before or after. There were significant movement-related artefacts among the activations recorded from performing the task with the affected hand. Post-treatment movement of the affected hand generated significant activation in the contralesional hemisphere. Ipsilesional activation volumes prior and post- were zero; contralesional activations pre- and post- were 264 and 471 voxels respectively. $\Delta FM_2 = -1.0$.

Figure 4.2: fMRI activations from the left and right hand-squeezing tasks, superimposed and transformed into the DWI space. Pre- activations are red–yellow; post- activations are dark-blue–light-blue. A white star indicates the lesioned hemisphere.

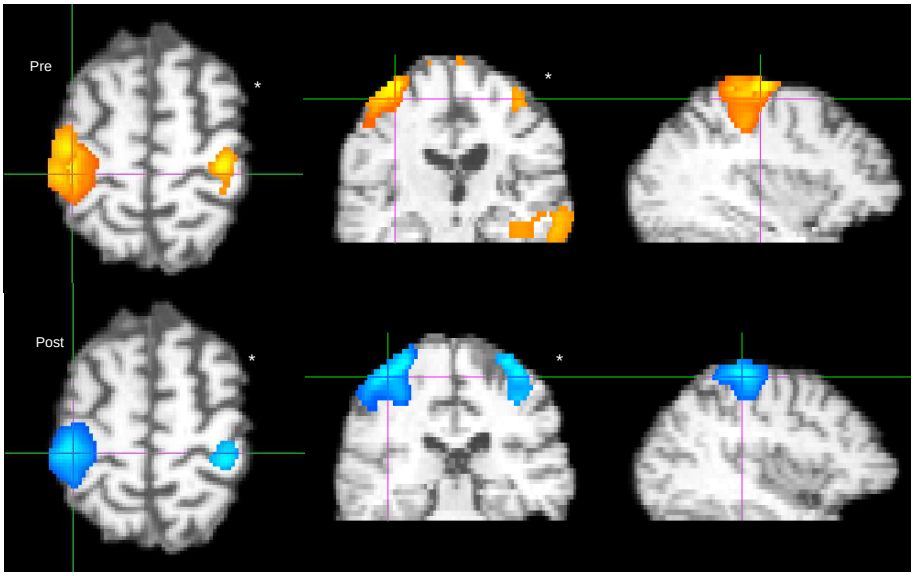

(c) **Patient 3:** fMRI activations (hand-squeezing task). Clean activations were observed pre- and post-therapy in both hemispheres. Activation volume in the ipsilesional (right) hemisphere rose from 283 to 436 voxels; and in the contralesional hemisphere dropped from 1417 to 1351 voxels. $\Delta FM_2 = 4.0$.

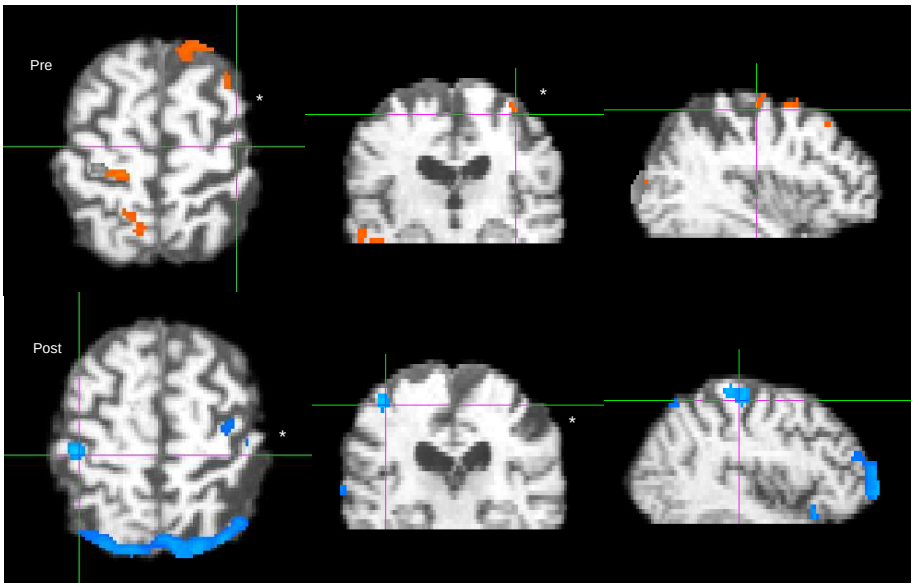

(d) **Patient 4:** fMRI activations (hand-squeezing task). In the contralesional (left) hemisphere, post- activation shifted laterally compared to the pre- activation. Activations in the ipsilesional hemisphere were smaller, with some contralesional activation before therapy. Contralesional activation volumes pre- and post-: 44 and 150 voxels; Ipsilesional volumes: zero and 48 voxels. $\Delta FM_2 = 5$.

Figure 4.2: **(cont.)** fMRI activations from the left and right hand-squeezing tasks, superimposed and transformed into the DWI space. Pre- activations are red–yellow; post- activations are dark-blue–light-blue. A white star indicates the lesioned hemisphere.

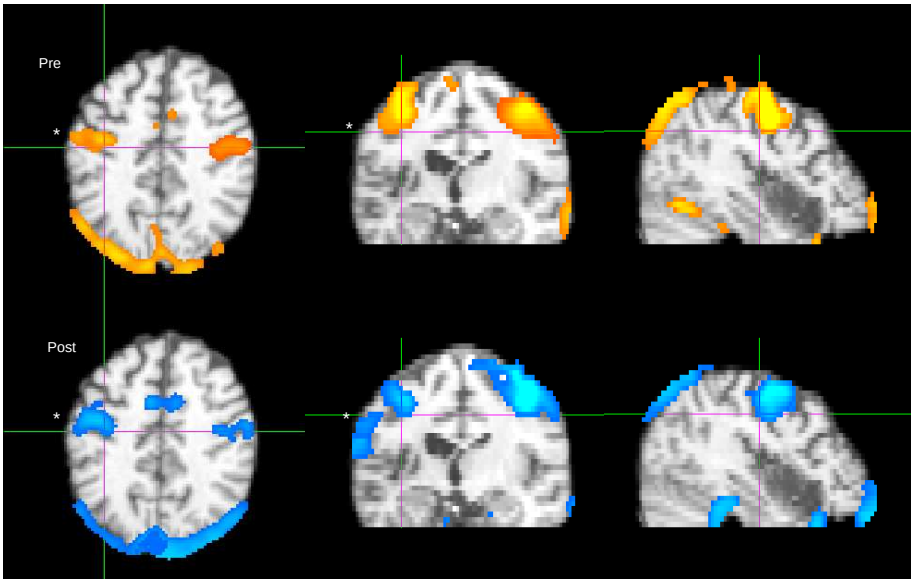

(e) **Patient 5:** fMRI activations (hand-squeezing task). Task performance led to patient movement and consequent messy activations with the affected (right) hand in the pre- scan and in the unaffected (right) hand in the post- scan. Activation volume in the ipsilesional hemisphere rose from 626 to 715 voxels. In the contralesional hemisphere, activation volume fell from 646 to 602 voxels. $\Delta \mathrm{FM}_2 = 6$.

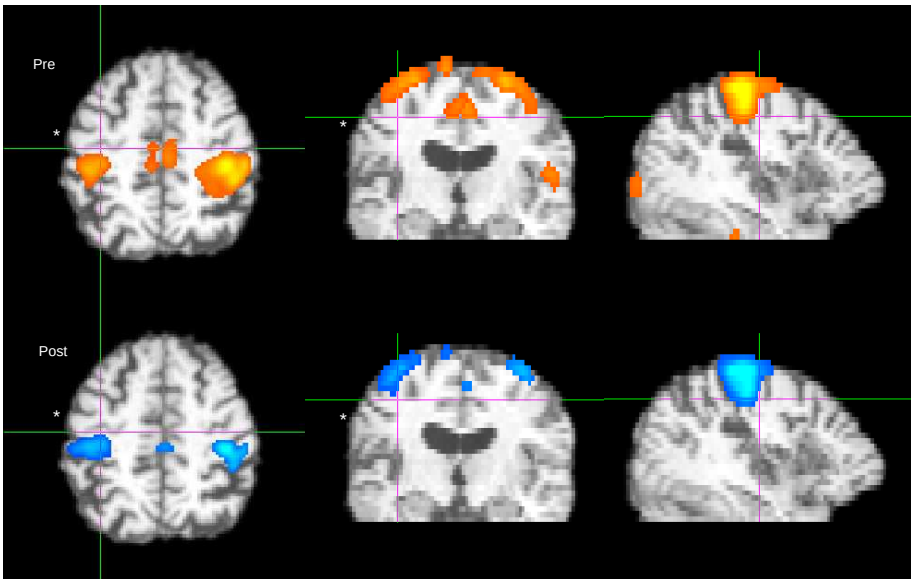

(f) **Patient 6:** fMRI activations (hand-squeezing task). Small, scattered activations in the pre- scan of both hemispheres gave way to cleaner activations in the post- scans. Activation volumes rose from 1334 to 1756 voxels in the lesioned hemisphere, and fell from 2092 to 909 voxels in the contralesional hemisphere. $\Delta \mathrm{FM}_2 = 3$.

Figure 4.2: **(cont.)** fMRI activations from the left and right hand-squeezing tasks, superimposed and transformed into the DWI space. Pre- activations are red–yellow; post- activations are dark-blue–light-blue. A white star indicates the lesioned hemisphere.

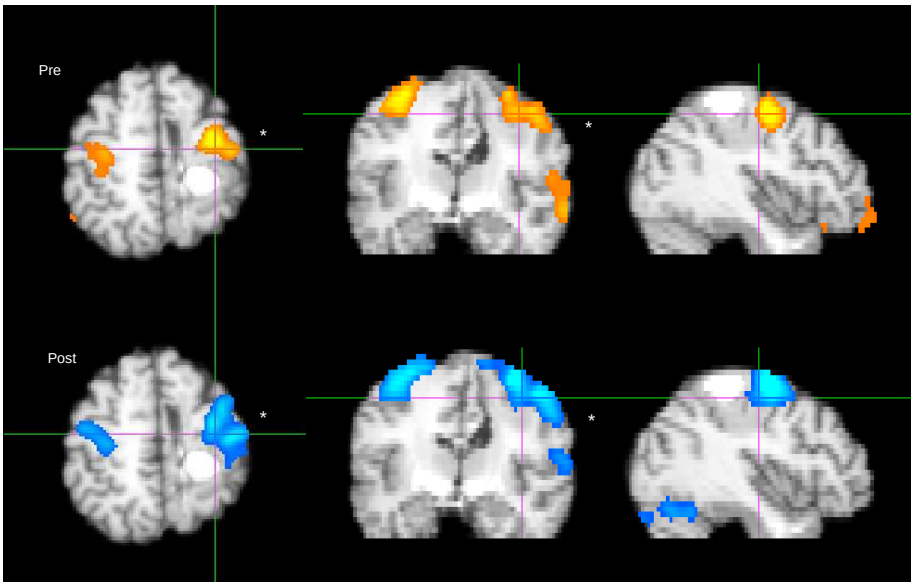

(g) **Patient 7:** fMRI activations (hand-squeezing task). Strong activations in both hemispheres increased in volume after the intervention, despite the obvious large stroke lesion. Activation volumes increased from 647 to 1024 voxels in the contralesional hemisphere, and from 605 to 1333 voxels in the lesioned hemisphere. $\Delta FM_2 = 2.0$.

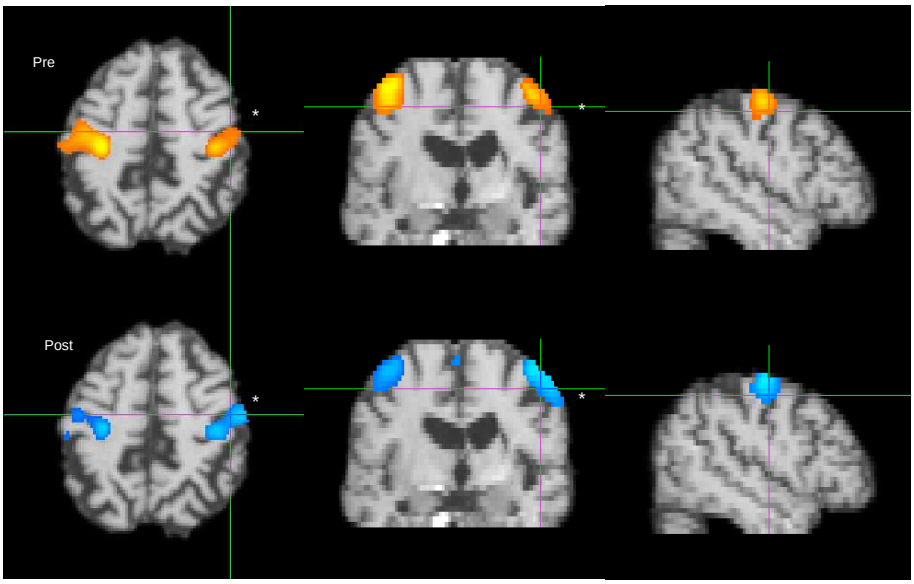

(h) **Patient 8:** fMRI activations (hand-squeezing task). This patient showed clean activations both pre- and post- in both hemispheres. In the contralesional hemisphere (left hand activations in the figure), the activation shrank from 1081 to 696 voxels. In the lesioned hemisphere (right hand activations in the figure), the activation increased in volume from 575 to 738 voxels. $\Delta FM_2 = 1.0$.

Figure 4.2: **(cont.)** fMRI activations from the left and right hand-squeezing tasks, superimposed and transformed into the DWI space. Pre- activations are red–yellow; post- activations are dark-blue–light-blue. A white star indicates the lesioned hemisphere.

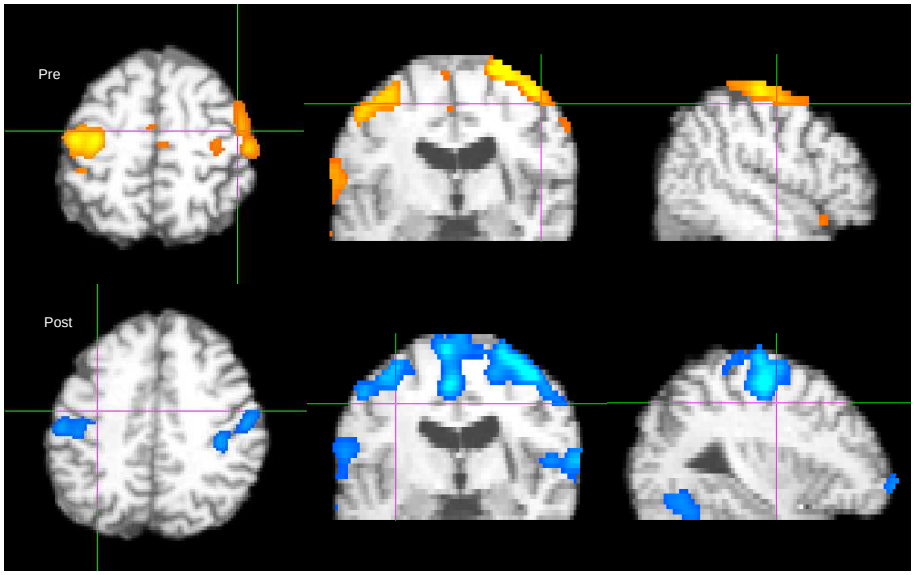

(i) **Patient 9:** fMRI activations (hand-squeezing task). There were strong activations pre- and post-, with some ipsilateral activation in the second left hand task. Activation volume increased in both hemispheres: from 917 to 1584 voxels in the contralesional hemisphere, and from 1438 to 1849 in the lesioned hemisphere. $\Delta \mathrm{FM}_2 = 4.0$.

Figure 4.2: **(cont.)** fMRI activations from the left and right hand-squeezing tasks, superimposed and transformed into the DWI space. Pre- activations are red–yellow; post- activations are dark-blue–light-blue. A white star indicates the lesioned hemisphere.

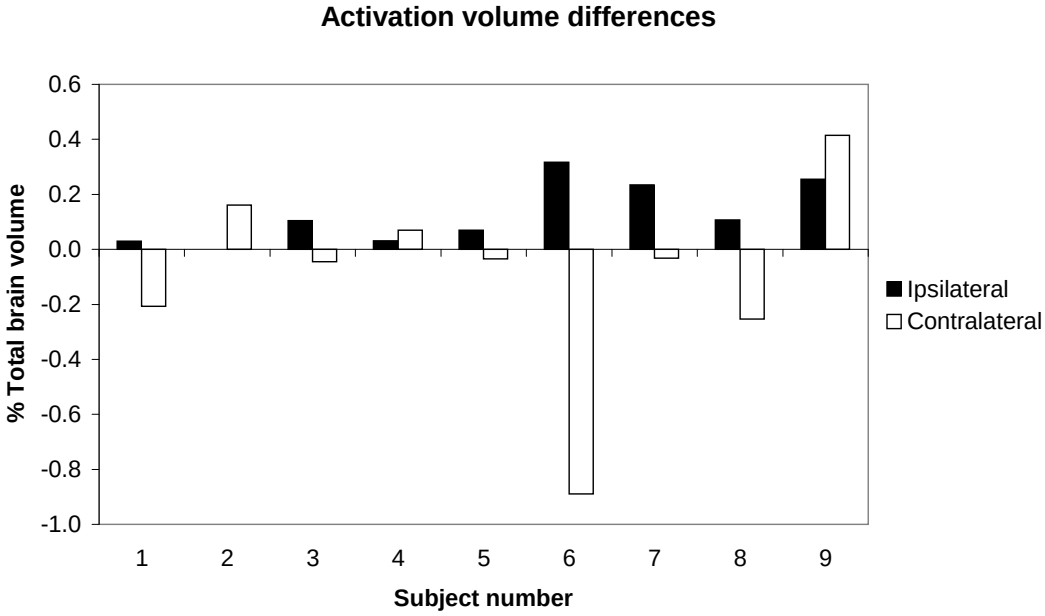

(a) fMRI activation volume changes. The legend is given relative to the stroke lesion. Ipsilesional activation volumes increased in all cases. Contralesional activation volumes decreased in six of the nine subjects.

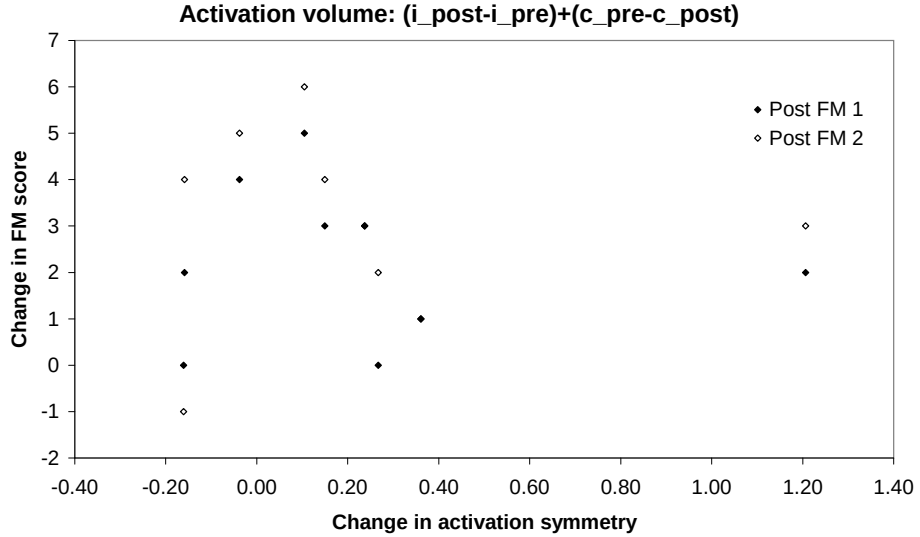

(b) Functional recovery and activation sizes. There is no relationship between functional recovery and change in the symmetry of fMRI activation.

Figure 4.3: Change in activation size and functional recovery

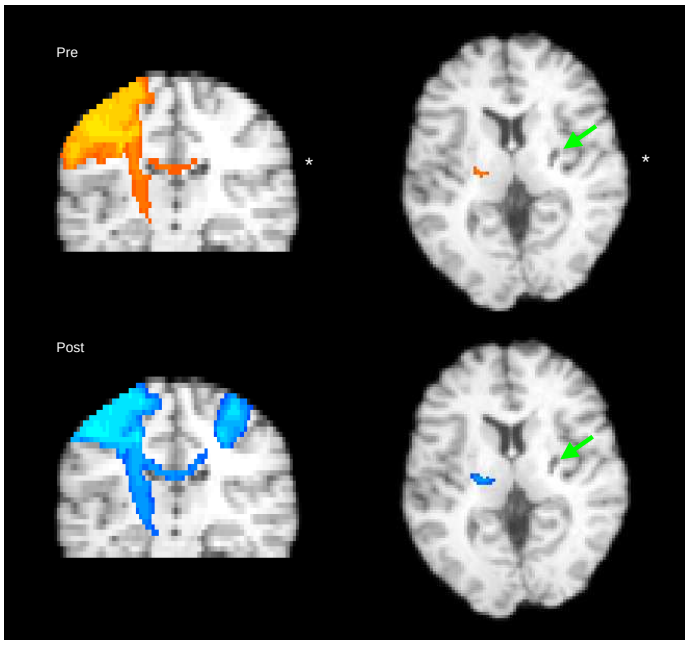

(a) **Probabilistic tractography. Patient 1:** There was no activation in the ipsilesional hemisphere prior to therapy. Despite increased activation volume following therapy, there was no connectivity to the right PLIC following therapy. The green arrow indicates the lesion. Note that even though the contralesional activation size decreased post-therapy, the connected CST is broader. $\Delta FM_2 = 3.0$.

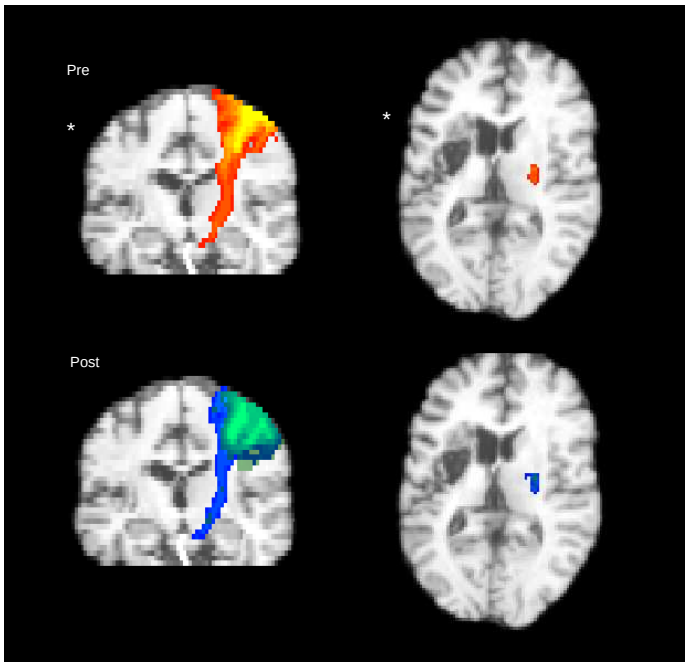

(b) **Probabilistic tractography. Patient 2:** Both before and after therapy there were no significant activations in the lesioned hemisphere. The contralesional hemisphere shows strong connectivity. The green area shows connectivity to the contralesional activation from use of the affected hand. $\Delta FM_2 = -1.0$.

Figure 4.4: Colourmaps show a log-scaled strength of connectivity to the activation seed masks. Each voxel is scaled according to the total number of paths that connect it with the seed area: there are 5000 possible paths for each seed voxel. Pre- connections are red–yellow; post- connections are dark-blue–light-blue. A white star indicates the lesioned hemisphere.

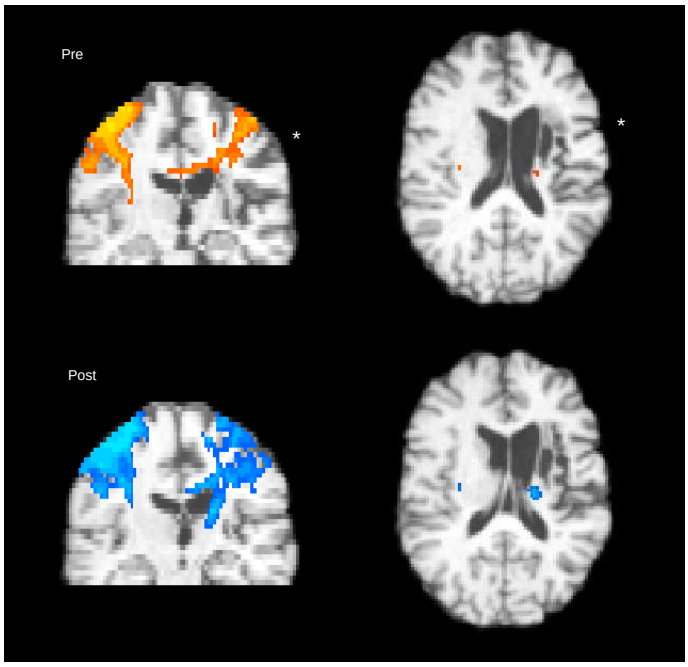

(c) **Probabilistic tractography. Patient 3:** The tractography showed connectivity to be stronger in the ipsilesional hemisphere, while the contralesional motor pathways descended through the external capsule. $\Delta FM_2 = 4.0$.

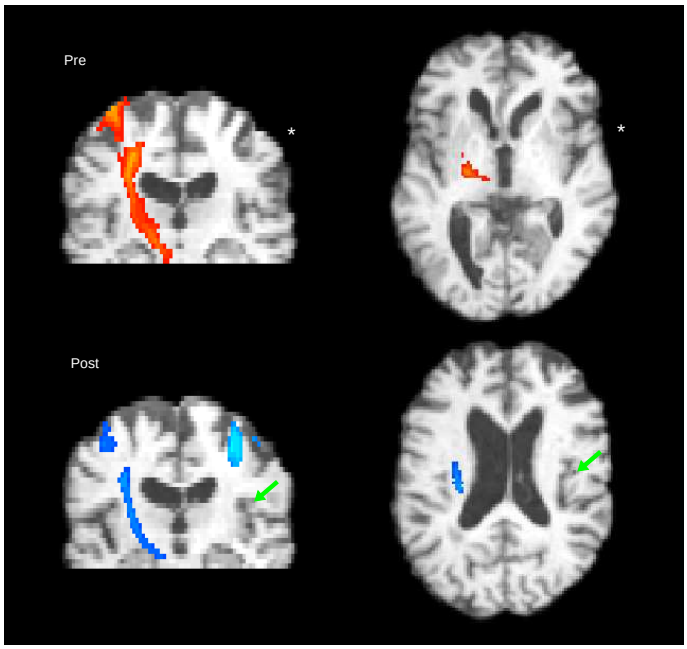

(d) **Probabilistic tractography. Patient 4:** There was strong connectivity in the contralesional hemisphere. There was no ipsilesional activation, and the post- activation shows no significant connectivity to the PLIC. There is a small infarct indicated by the green arrow. The lack of connectivity suggests Wallerian degeneration. $\Delta FM_2 = 5.0$.

Figure 4.4: **(cont.)** Colourmaps show a log-scaled strength of connectivity to the activation seed masks. Pre- connections are red–yellow; post- connections are dark-blue–light-blue. A white star indicates the lesioned hemisphere.

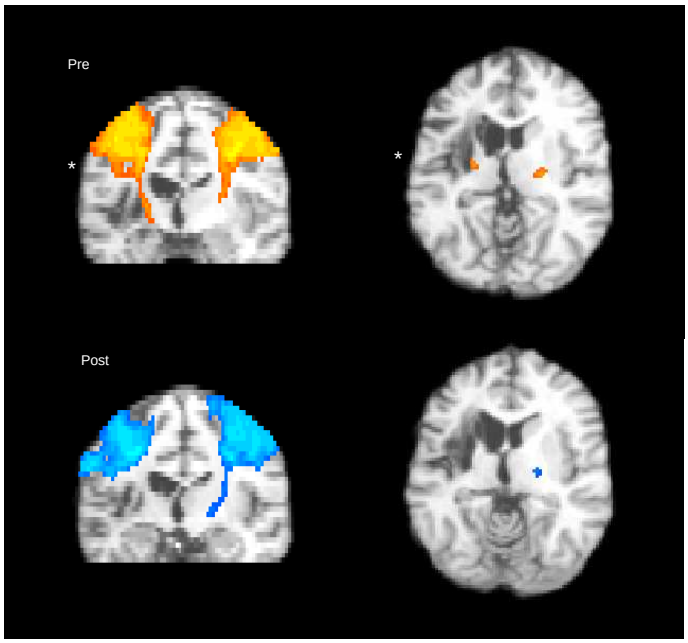

(e) **Probabilistic tractography. Patient 5:** There was no connectivity to the ipsilesional PLIC after therapy despite the larger activation. $\Delta FM_2 = 6.0$.

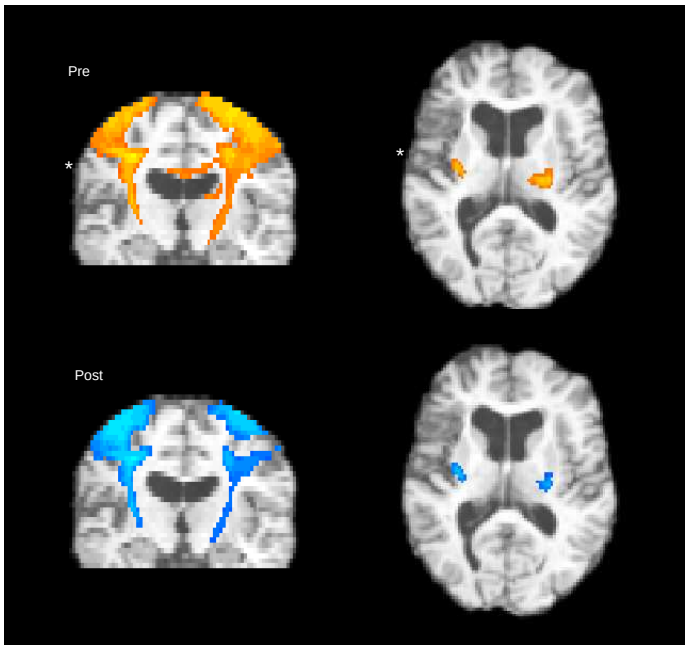

(f) **Probabilistic tractography. Patient 6:** Good connectivity was slightly weaker in the ipsilesional (left) hemisphere, and displaced latero-posteriorly compared with the contralesional activation. $\Delta FM_2 = 3.0$.

Figure 4.4: **(cont.)** Colourmaps show a log-scaled strength of connectivity to the activation seed masks. Pre- connections are red–yellow; post- connections are dark-blue–light-blue. A white star indicates the lesioned hemisphere.

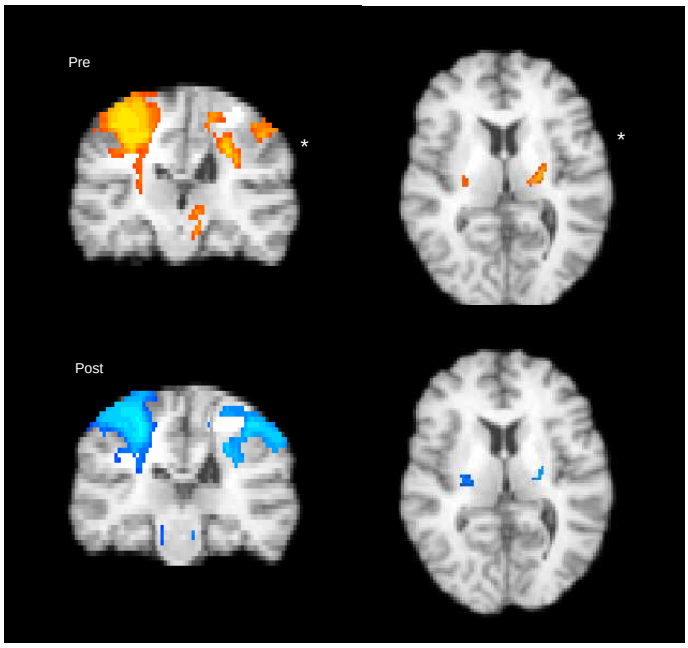

(g) **Probabilistic tractography. Patient 7:** Relatively strong connectivity in the ipsilesional hemisphere was weaker following therapy, while the contralesional connectivity was greater following therapy. $\Delta FM_2 = 2.0$.

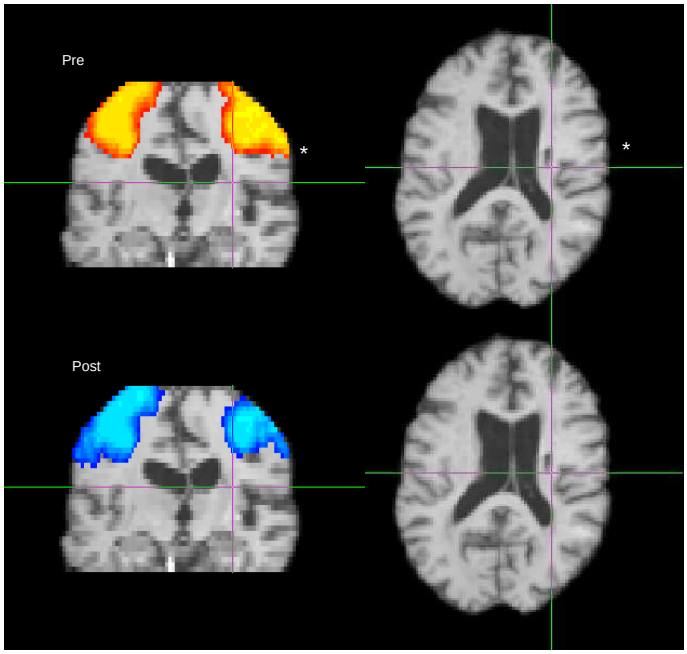

(h) **Probabilistic tractography. Patient 8:** Symmetrical activations showed no significant connectivity to the brainstem. The principle eigenvector field for patient 8 was unusually noisy, which affected the tractography. $\Delta FM_2 = 1.0$.

Figure 4.4: **(cont.)** Colourmaps show a log-scaled strength of connectivity to the activation seed masks. Pre- connections are red–yellow; post- connections are dark-blue–light-blue. A white star indicates the lesioned hemisphere.

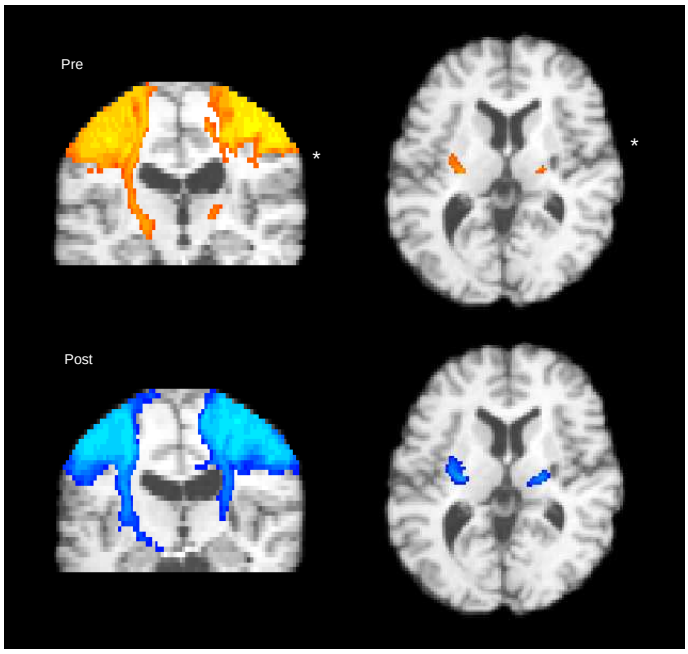

(i) **Probabilistic tractography. Patient 9:** Connectivity in the ipsilesional (right) hemisphere was slightly weaker, and displaced medially by the lesion. Connectivity was stronger bilaterally post- therapy. $\Delta FM_2 = 4.0$.

Figure 4.4: **(cont.)** Colourmaps show a log-scaled strength of connectivity to the activation seed masks. Pre- connections are red–yellow; post- connections are dark-blue–light-blue. A white star indicates the lesioned hemisphere.

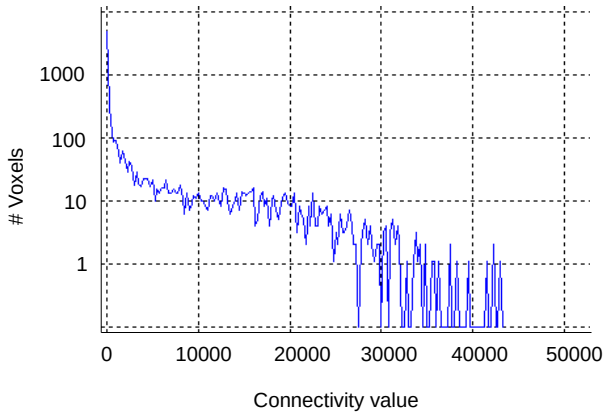

Figure 4.5: Connectivity histogram from subject 1

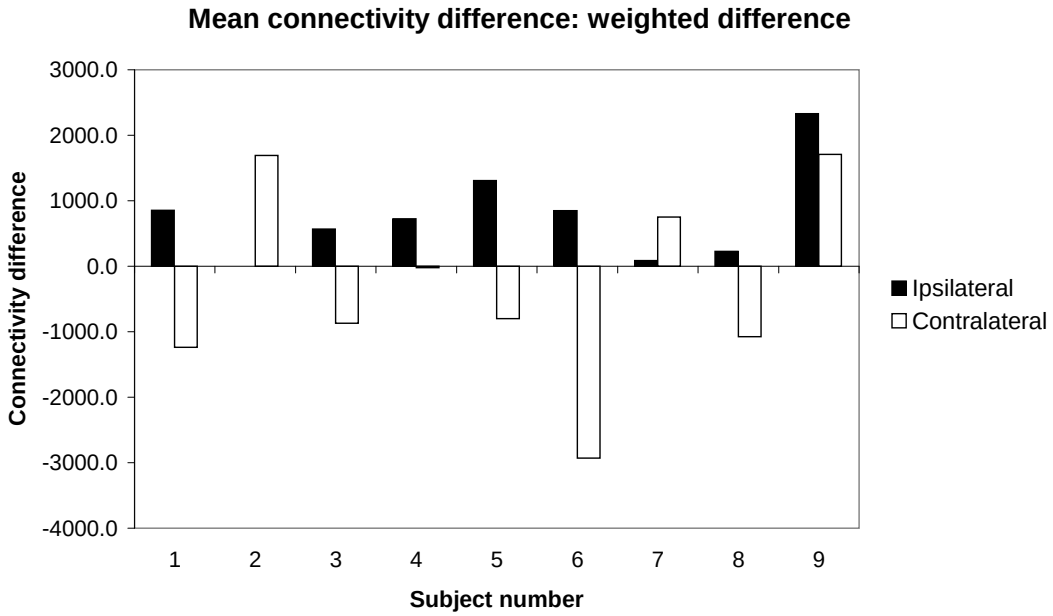

(a) Changes in mean connectivity to the motor task activation seed masks. The legend is given relative to the stroke lesion. Ipsilesional connectivity increased in all cases. Contralesional connectivity decreased in five of the nine patients.

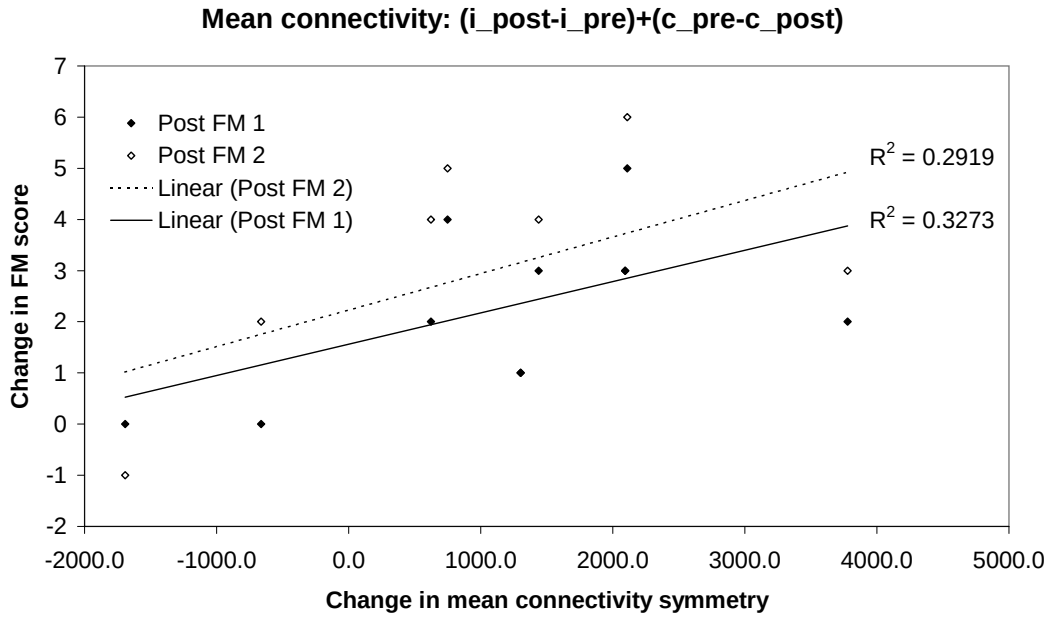

(b) Functional recovery and mean connectivity changes. The relationship is stronger than that between activation size and functional improvement (Fig. 4.3(b)).

Figure 4.6: Change in mean connectivity symmetry and functional improvement.

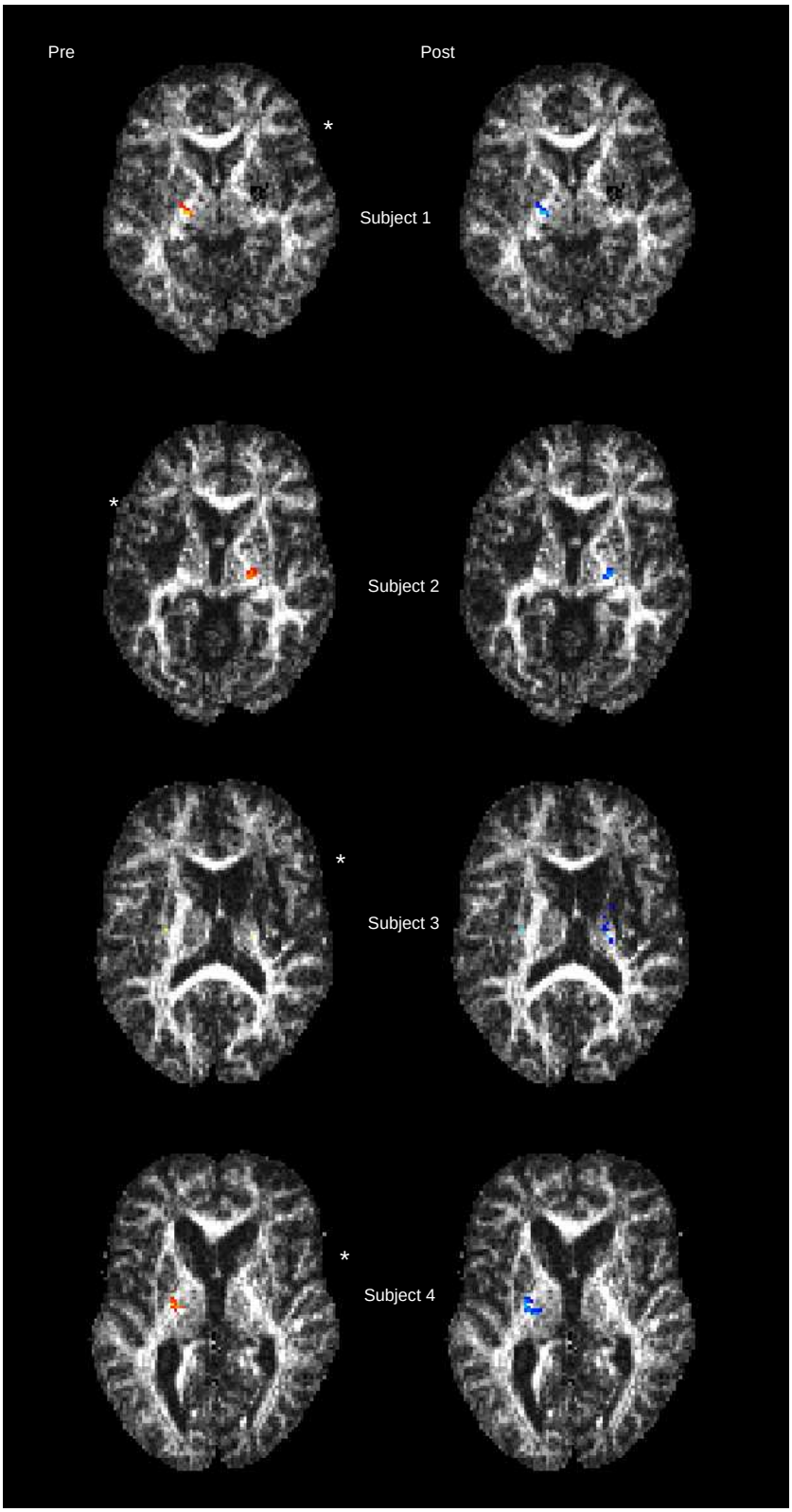

Figure 4.7: Internal capsule connectivity to the fMRI activations. Results have been thresholded at 10%. Contralesional location of connections is consistent with the results of previous studies [42, 43] and shows good reproducibility. Ipsilesional connectivity to the PLICs is highly variable. A white star indicates the lesioned hemisphere.

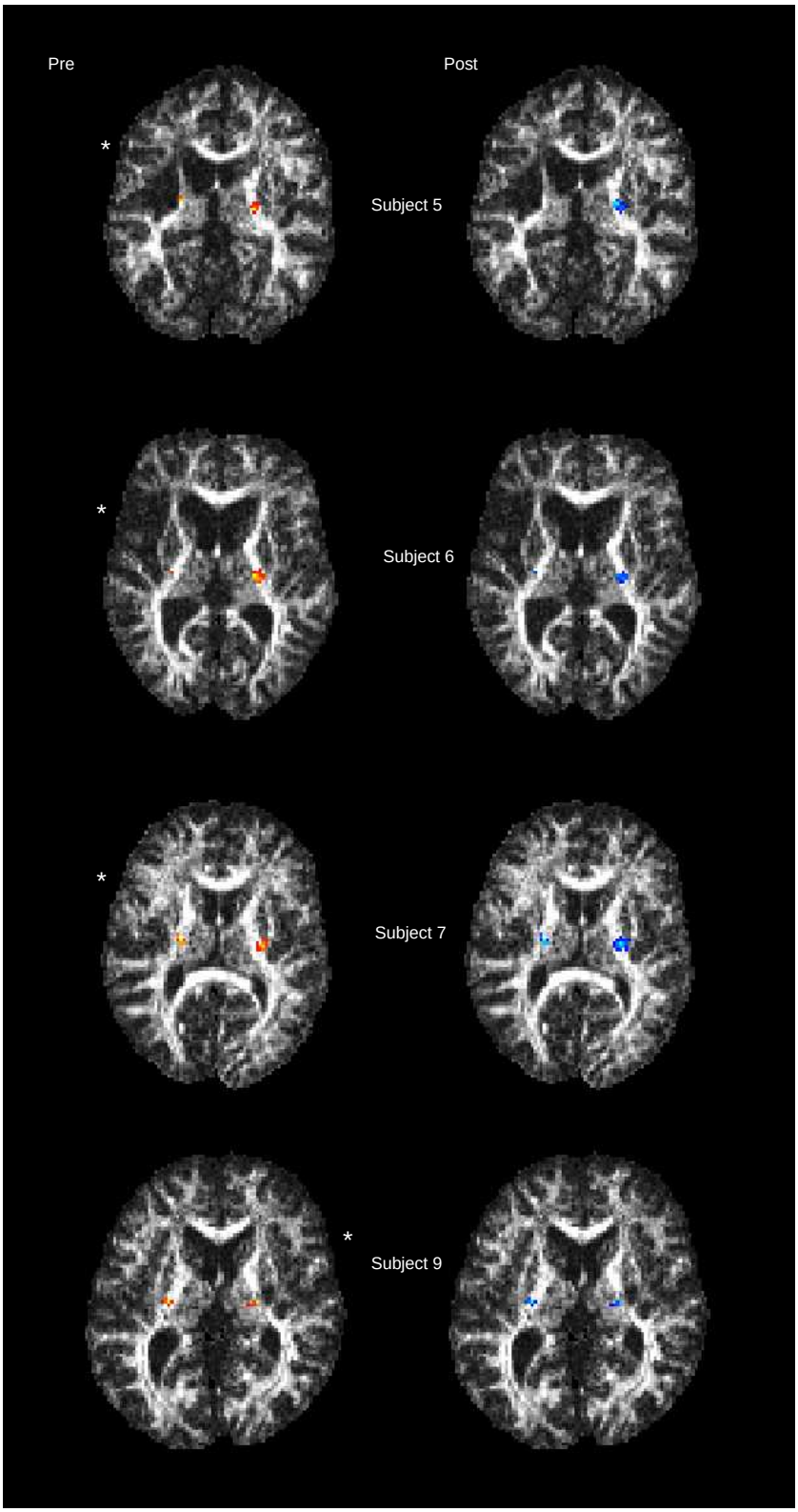

Figure 4.7: **(cont.)** Internal capsule connectivity to the fMRI activations.

Chapter 5

Discussion

The MNL stroke study is one of several multimodal neurological studies made possible only recently by technical developments in MRI and by the evolution of DTI (e.g. [61, 62, 66]). Since this project studied just nine patients in detail, it is possible to analyse each one individually, comparing the results from each modality. Section 5.1 discusses the individual results. Section 5.2 discusses group-level conclusions in a qualitative way. Finally, section 5.3 contains suggestions for further work.

5.1 Individual results

Patient 1. Patient 1 had a lacunar infarct within the right PLIC territory. The FA asymmetry value of 0.151 reflects this compromised PLIC integrity, and the fact that no MEP could be elicited from this subject using TMS both pre- and post-therapy reflects compromised motor neurological connectivity—structural and/or functional. Probabilistic tractography also found no significant ipsilesional connectivity between fMRI activation and PLIC. The lack of MEP and connectivity suggest that this subject may be activating contralesional motor cortex when using their affected limb. This compensation is not as efficacious for functional improvement as re-establishing some CNS functional symmetry [2, 4].

The fact that there is no significant connectivity from the post- ipsilesional activation to the right PLIC, or to the corpus callosum, and yet there is a considerable sensorimotor activation, suggests that the tractography may be failing at the point where the superior longitudinal fasciculus (SLF) crosses the CST and the corpus callosum—tracking the anisotropy here is not made any easier by having only 12-direction data. But the crossing problem also affects tractography in scans derived from more directions. In their DTI study of PLIC somatotopy, Zarei et al. [43], using 54 directions, masked out the SLF in their tractography, and made an assumption that the CST would be linear across the width of the mask. In patient 1, the contralesional PLIC somatotopy accorded with the results of Zarei et al., which are shown in Figure 5.1. Closer inspection of the connectivity maps shows that the lesion in fact disrupts exactly that part of the PLIC through which the relevant fibres should descend (Fig. 5.2(a)). However, there must be some limited connectivity because there is significant cortical activation that correlates with movement of the affected hand. This subject even "squeezed better" following therapy, judging by the small increase in squeezing frequency (Table 4.2).

We can conclude from this that there is ipsilesional connectivity but that it is beyond the resolution of both the DTI and the TMS to detect.

Patient 2. Like patient 1, patient 2 produced no MEP both before and after therapy, but subject 2 persisted in showing no ipsilesional connectivity even after therapy. Con-

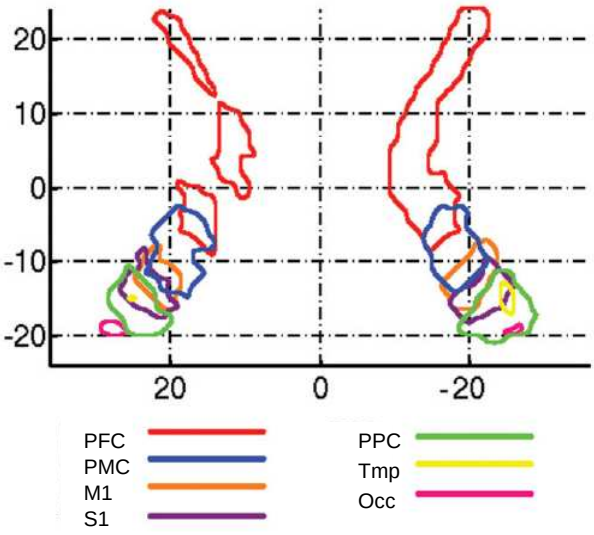

Figure 5.1: PLIC somatotopy from probabilistic tractography. Group segmentation map based on 11 healthy subjects, showing a topographical organization of cortical tracts in the internal capsule. The map was thresholded to include voxels that were present in >30% of the group and illustrates the overlap between connection regions, notably the premotor cortex and M1, and M1 and S1. PFC = prefrontal, PMC = premotor, M1 = primary motor, S1 = sensory, PPC = posterior parietal, Tmp = temporal, Occ = occipital cortices. Source: Zarei et al., [43].

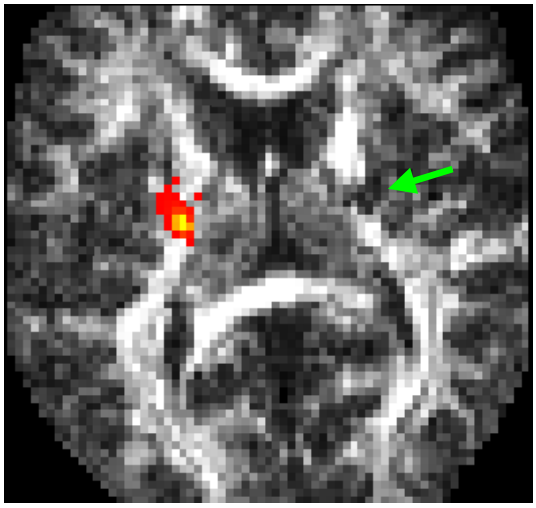

(a) Patient 1: The stroke lesion (green arrow) disrupts the right PLIC at the location of the descending sensorimotor tracts (see Fig. 5.1).

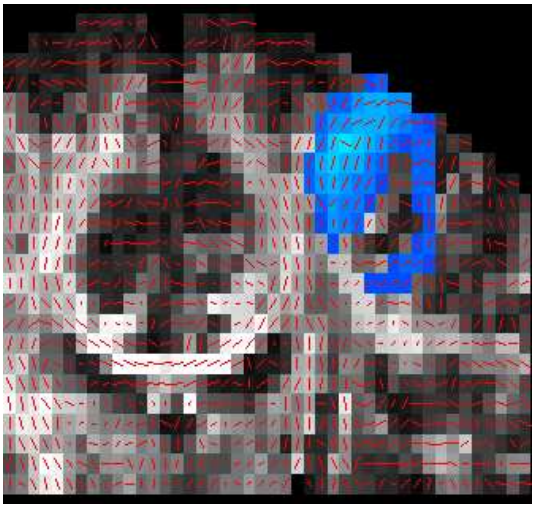

(b) Patient 1: The principal eigenvector field around the activation in the lesioned hemisphere fails to resolve limited sensorimotor connectivity.

Figure 5.2: Generally, tracking white matter in the lesioned hemispheres was difficult because of low FA values in the lesioned region (a), and weaker sensorimotor connectivity (b).

tralesional activation following the therapy suggests that the contralesional hemisphere is contributing more to the control of the affected hand: there was no change in ipsilesional activity, and contralesional activation increased.

Probabilistic connectivity mapping in the contralesional hemisphere revealed topographical organisation of sensorimotor tracts in the right PLIC that corresponds to the

population maps shown in Fig. 5.1. Probabilistic tractography from the group level activation coregistered to the individual space revealed that ipsilesional sensorimotor connectivity in patient 2 does exist down to the brainstem, but through the posterior PLIC. The rest of the PLIC on this side has been quite severely disrupted by the stroke lesion (Figure 5.3), reflected in the high FA asymmetry value.

Tractography shows that connectivity exists, but fMRI and TMS show that it is not being used. The poor response of this subject to the intervention supports the idea that stroke recovery is more limited if the contralesional hemisphere is recruited for motor control of the affected muscles than if some of the original ipsilesional control is preserved [2].

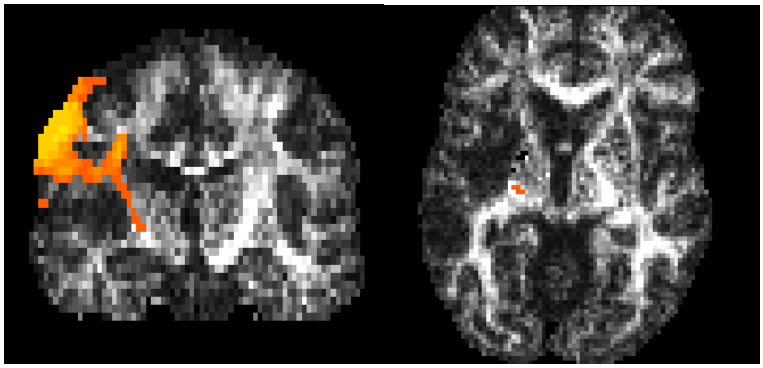

Figure 5.3: Patient 2: Probabilistic tractography from the group cortical activation for the squeezing task shows that sensorimotor connectivity does exist in the ipsilesional hemisphere.

Patient 3. This patient showed significant contralesional activation when using the affected hand before therapy which disappeared in the second fMRI session. Significant involvement of the lesion with the right PLIC (FAA = 0.204) contributed to the fact that probabilistic tractography did not find any connectivity between the activation and the PLIC prior to therapy.

The contralesional PLIC connectivity map shows the hand fibres descending via the posterior external capsule. Ipsilesional connectivity increased following the intervention, which is consistent with the significant functional improvement this patient made (ΔFM_2 = 4).

The fact that the contralesional connectivity to the activation went through the external capsule rather than the PLIC suggests, given that this subject responded well to the intervention by all measures, that the tractography is being confounded superior to the PLICs by crossing fibres.

Patient 4. Patient 4 had a very small lesion midway between the right PLIC and the anterior lateral parietal cortex. The PLICs show very little asymmetry (FAA = 0.008), and the clinical assessments indicate a relatively high level of function and a significant improvement in FM score.

The tractography puts the contralesional descending motor tracts at the level of the PLIC in a position that accords with Fig. 5.1. Despite the lesion size, the ipsilesional fMRI activation indicates compromised neurological function, and tracking from this seed mask terminated rapidly. Figure 5.4 below shows that the ipsilesional PLIC does show

significant connectivity to the group activation, shown in yellow, and that the connected voxels in the PLIC look anatomically reasonable. This subject also produced a MEP. These considerations suggest that the ipsilesional connectivity is not being resolved by the directional information in the diffusion tensor.

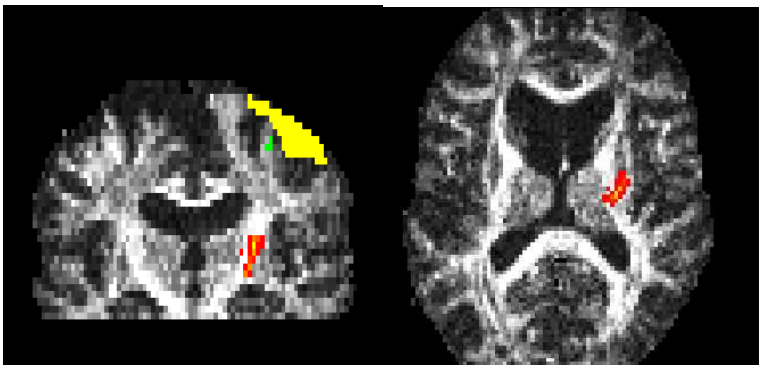

Figure 5.4: Patient 4: Probabilistic connectivity mapping from the ipsilesional PLIC to the group fMRI activation (yellow) shows that sensorimotor connectivity exists in the ipsilesional hemisphere. The connectivity map is shown in red-yellow. However the patient's own activation (green) is displaced from the group activation and shows no connectivity to the PLIC.

Patient 5. Patient 5 was unusual in showing connectivity to the ipsilesional PLIC before the intervention, but none afterward. At the same time, the squeezing frequency decreased. The patient performed poorly in the second fMRI scan, but in fact, this patient showed strong functional improvement ($\Delta FM_2 = 6$).

Despite a relatively large lesion and significant disruption of the CST in the region of the PLIC (FAA = 0.18), there is a general symmetry in the connectivity in patient 5 which improved after the intervention. The main lesion lies anterior to the PLIC and appears not to affect the fibre tracts of interest in this study. This, the fact that TMS produced MEPs, and the strong functional improvement suggest that the lack of ipsilesional post-connectivity is an artifact of underestimation of the tract size by the 12-direction diffusion scan.

Patient 6. This patient has a left subcortical lesion that does not appear to compromise very much either their clinical or their neurological function by the terms of this study. FA asymmetry was low (0.05) because the lesion is located posterior to the left PLIC. Connectivity to the left PLIC is compromised, however (see Fig.4.7), and the descending pathways at the level of the PLIC are displaced posteriorly compared to those in Fig. 5.1 and to the healthy PLICs in other patients.

Patient 7. Like patient 6, this patient showed very little lesion involvement with the PLICs (FAA = 0.021) and scored highly in the clinical assessment. The connectivity analyses revealed location of ipsilesional descending pathways at the level of the PLIC that closely approximates that in healthy participants.

Patient 8. Despite having MEPs and symmetrical activations, connectivity analyses on this patient failed to produce any results. The principle eigenvector field was unusually noisy (see Fig. 5.5).

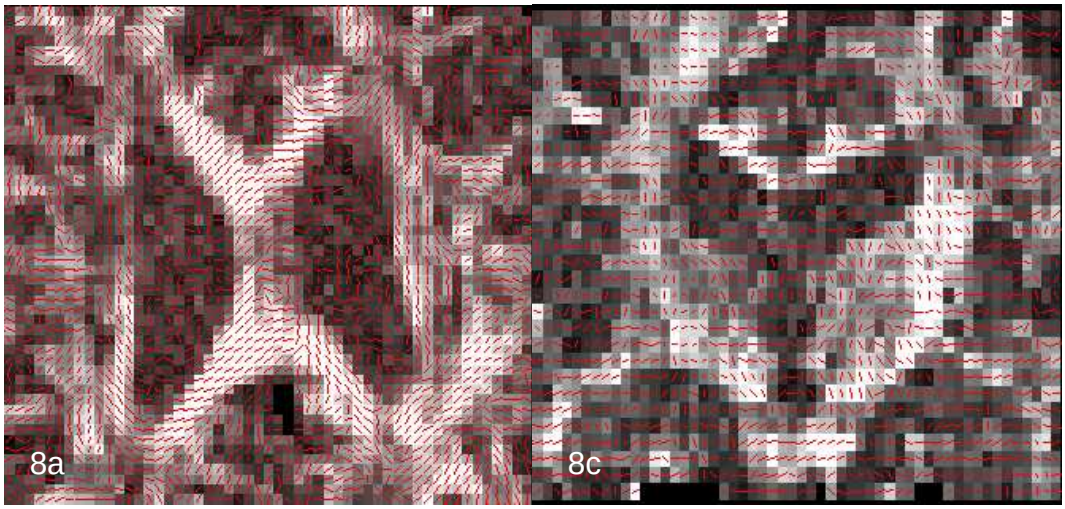

Figure 5.5: Subject 8: The noisy principal eigenvector field precluded connectivity analyses. Compare these pictures with Figs. 3.2 and B.1.

Patient 9. Like patients 6 and 7, patient 9 showed a symmetry in fMRI activations and in connectivity that was relatively little disrupted by the stroke lesion. Although the lesion is very close to the right PLIC, it affects the PLIC FA very little (FAA = 0.060). Figure 4.4(i) shows that the hand fibres on the lesioned side are displaced slightly away from the lesion.

5.2 General conclusions

We can discuss these results in terms of the aims stated in §1.3.1 of Chapter 1. It was anticipated when beginning the probabilistic analysis that it would be easier to acquire results from the lesioned hemispheres. In particular, the lack of ipsilesional fMRI activations in some patients was not foreseen. This rendered the aim of "seeding from the activations" meaningless. Also, in those patients who did have significant activations, the tractography did not always extend to the PLIC in the affected hemisphere. Aims 1 and 2 of §1.3.1 will therefore be addressed together.

Somatotopy in the PLIC. If the PLIC is divided into four quarters, the studies of Holodny et al. [42] and Zarei et al. [43] both locate the CST at the level of the PLIC in the third quarter. Motor and sensory pathways overlap within the CST [43], and hand fibres are generally located anterolateral to foot fibres [42].

The contralesional PLIC connectivity results of the current study are consistent with these results. The fibres of the CST pass through the third quarter in most subjects, and slightly more posteriorly in some (see patients 6 and 9 in Fig. 4.7). In patients 2, 4, 7, 9 and in the post-intervention map from subject 5, the voxels of maximum connectivity lie in the anterolateral part of the third quarter. Except in the case of patient 5, these locations stayed the same for both pre- and post- fMRI activations, despite the changes in the activations. In patient 5, the point of maximum connectivity was more lateral in the second scan. Acquiring scans along more mpg directions might provide more certainty in the results, but in the meantime, the contralesional connectivity corroborates the findings of the previous studies.

Disruption of the PLIC by the stroke lesion and/or lack of connectivity in the ipsilesional hemisphere mean that there is no comparison with somatotopic studies of healthy brains. The main point to be drawn from the ipsilesional tractography is that while contralesional sensorimotor connectivity has some anatomical consistency and reproducibility, the post-stroke anatomy in the lesioned hemisphere is unique to each individual. This means that second-level group analyses are problematic in a stroke population.

Connectivity and TMS. TMS of patients 1 and 2 produced no MEPs, indicating very poor motor connectivity. Not surprisingly, both subjects produced very limited or no activations in the ipsilesional hemisphere. Also not surprisingly, probabilistic tractography failed to find connectivity between their cortical activations, when they were present, and the PLICs. However, given that little or no connectivity was found in many of the lesioned hemispheres that *did* produce MEPs, it seems safe to say that where TMS cannot elicit a MEP, it is unlikely that the tractography will be able to image connectivity from the stimulated cortical area, while a lack of DTI connectivity does not guarantee that there really is no connectivity.

A comparison between 12- and 30-direction DTI data. In Appendix B, a 30-direction DTI scan is compared with a 12-direction scan of a healthy subject. The results indicate that the connectivity values from the 12-direction scans in the CST barely exceed the noise level. This explains the variability in the ipsilesional tractography results, and suggests that some connected pathways could perhaps have been negotiated through the lesioned hemisphere with 30-direction scans.

Activation size and connectivity. The connectivity measure relies on a single volume of voxelwise pdfs on the diffusion parameters. Therefore any change in the pre- to post-connectivity depends to some extent on the displacement, contraction, or dilation of the fMRI activation—there is no post-intervention diffusion data set. This raises the question of why the connectivity changes should correlate with the change in FM score better than the activation volumes. The two measures, calculated from (4.1) correlate only weakly with each other (see Fig. 5.6).

Answering this question requires a closer look at the definition of Δ:

$$\Delta = k(I_{\text{post}} - I_{\text{pre}} + C_{\text{pre}} - C_{\text{post}}), \tag{5.0}$$

The connectivity is defined in such a way that it will depend on the seed mask size. i.e. a large activation will produce a larger mean connectivity. Because of the dependence of connectivity on seed mask size, the value of (5.1) for connectivity (call it Δ_c) will depend on the value for the activation size (call it Δ_a). The value of (5.1) is larger the bigger the ipsilesional post-pre difference and the bigger the pre-post contralesional difference in activation volume or mean connectivity. For Δ_c to correlate with change in FM score then, when Δ_a does not, indicates that connectivity depends on more than just the seed mask volume. And of course, this is true. Connectivity *also* depends on the white matter integrity. The BOLD activation volume is independent of white matter integrity. The positive correlation between Δ_c and change in FM score in Fig. 4.6(b) is revealing a relationship between white matter integrity and functional improvement.

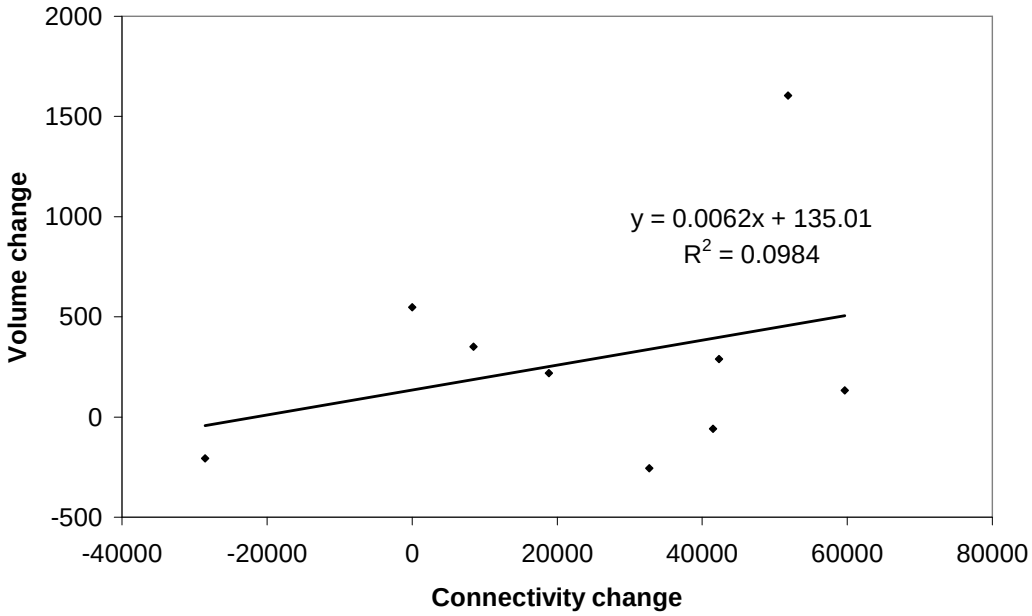

Figure 5.6: Correlation between the change in mean connectivity and the activation volume changes calculated from (4.1).

This result provides support for the findings of Ward et al. [55] and Stinear et al. [57]: that functional improvement in stroke patients depends on CST integrity. In the latter, CST integrity was measured according to the asymetry of the mean FA in the PLICs (3.1). Obtaining a measure of CST integrity via the process of coregistering fMRI activations and doing probabilistic tractography is perhaps more objective than evaluating PLIC FA asymmetry, which depends on the determination of a PLIC ROI, and also on some kind of direct involvement of the lesion with the PLIC for it to be sensitive to asymmetry. The correlation in Fig. 4.6(b) is independent of the lesion location.

This relationship also provides support for the statement in Ward (2005) [2] that functional recovery depends upon the extent to which the pre-stroke, more symmetrical neurophysiology can be regained within the new post-stroke architecture. The correlation in Fig. 4.6(b) shows that the development of more symmetrical activations following therapeutic intervention does not mean anything for functional improvement without the underlying corticospinal integrity. This result suggests that the movement of the fMRI activations occurs in such a way as to make the most of the preserved white matter connectivity.

This result was obtained from a longitudinal analysis—it still begs the question of whether there exists a measure of CST integrity that can predict functional outcome. In providing evidence for the benefits of persevering with bilateral motor control as far as possible, however, it suggests that after a single initial assessment it will be possible to tailor therapeutic intervention in such a way that symmetrical motor control is encouraged if it is not already present and the connectivity still exists (e.g. subject 2 in this study).

Summary. Probabilistic tractography was chosen for assessing the connectivity in nine patients from whom DWI data sets were acquired along 12 diffusion gradient directions. From the outset, two factors constituted obstacles to producing robust connectivity in this data, which were mentioned in §2.2.4. First, the distribution of the 12 directions means that there is as much as a $\pm 5^\circ$ uncertainty in the measured fibre orientation; second, the maximum orientation uncertainty lay in directions that corresponded to the white matter pathways we were most interested in. However, despite these obstacles, there are some strong conclusions to be drawn from the DTI analysis.

Connectivity appears relatively robust and reproducible in the unlesioned hemispheres, considering the proviso about the underestimation/uncertainty of corticospinal tractography derived from 12-direction DTI scans. In all subjects, the location and size of fibre trajectories was consistent with recent findings. We can conclude that 12-direction scans are sufficient for determining sensorimotor connectivity in healthy subjects.

Ipsilesional connectivity is highly variable in comparison. The lesion does not have to be large or directly involved with the CST to severely compromise connectivity. The ipsilesional tractography was further hindered by the uncertainty from the mpg gradient orientations. More robust tractography in the ipsilesional hemisphere of stroke patients might be achieved using more diffusion gradient directions. Technological advances mean that these will probably become routine in the near future.

Regions of high uncertainty in fibre orientation, like the lesions where they disrupted the PLICs and the intersection of the SLF, CST, and corpus callosum, were also obstacles to the tractography. There is a possibility that in the lesioned hemisphere of chronic stroke patients, Wallerian degeneration may reduce white matter anisotropy distal to the lesion, reducing the likelihood that the relevant connections can be made [67].

Ipsilesional fMRI activation size and connectivity increased in all patients following the intervention. Contralesional activation size and connectivity decreased in most patients following the intervention. A measure of the extent to which symmetry of activation volume and connectivity was regained was defined in (4.1). This measure did not correlate with functional improvement in the case of the activation volumes, but in the case of mean connectivity, a small–medium [68] correlation was observed. So the size of the fMRI activations and the extent to which they approach the original symmetry is not as important for functional improvement as the connectivity, and the extent to which the connectivity approaches the pre-stroke symmetry. This result reveals firstly that there is a relationship between structural integrity of the CST and functional improvement, corroborating recent results [55, 56, 57]. But, furthermore, the current result shows the relationship between the *redressed symmetry* of connectivity and functional improvement.

The CST connectivity measured from fMRI activation seed masks is a non-subjective way of assessing corticospinal integrity. This analysis used custom-made batch scripts that made use of the SPM toolbox for the fMRI data, and similar unix scripts can be readily written for the FSL pipeline. By providing a means of investigating the viability of the sensorimotor CNS in stroke patients, this analysis can inform rehabilitative intervention in the clinic by suggesting therapies that are tailored to optimise the preserved connectivity in individual patients.

5.3 Suggestions for further work

An obvious suggestion for a future analysis of this type is to acquire a DWI data set with >25 directions, and determine whether the lower uncertainty in orientation is capable of resolving the stroke-affected connectivity.

Given that a correlation has been found in the data so far with only nine patients, it would be useful to apply the above analysis to the rest of the twenty-eight stroke study participants for which the same data is available, and test the relationship further.

Chapter 6

Conclusions

This study used Diffusion Tensor Magnetic Resonance Imaging (DTI) to investigate the connectivity of the corticospinal tracts (CSTs) in the brains of nine subjects who suffered a stroke at least 6 months before particpation in the study. The location of the CST and its somatotopic arrangement in the posterior limbs of the internal capsules (PLICs) in the contralesional hemisphere were consistent with results obtained in previous studies. However, the presence of the stroke lesion strongly affected the ability of the probabilistic tractography algorithm to follow white matter tracts in the lesioned hemisphere. It is suggested that diffusion-weighted scans acquired along more directions than 12 may be able to resolve compromised ipsilesional connectivity. A measure sensitive to the extent to which symmetrical mean connectivity is regained following intervention was found to correlate with change in clinical score. This measure is less subjective and more comprehensive than those used in previous studies. This correlation supports the theory that it is the extent to which motor neurophysiological symmetry can be regained in the post-stroke architecture that determines functional recovery. It also suggests that the movement of the fMRI activations occurs in such a way as to make the most of the preserved white matter connectivity. These results are contributing to a three-year, multimodal stroke study which aims to use such results to individually tailor stroke therapy, optimising the preserved neurophysiology for functional rehabilitation.

Appendix A

FA asymmetry and clinical results for all subjects in study

FAA = Fractional Anisotropy asymmetry (manual ROI); Pre FM2 = second pre-intervention FM score; Post FM1 = First post-intervention FM score; Post FM2 = Second post-intervention FM score; ΔFM_x = the difference in FM score between the second pre-intervention clinical FM assessment and the xth (first or second) post-intervention assessment; MEP = Motor Evoked Potential (1 = MEP produced, 0 = No MEP); APBT = Active Passive Bimanual Therapy (1 = APBT + Task, 0 = Task only).

Subject	Lesion	FAA	PreFM2	PostFM1	PostFM2	ΔFM1	ΔFM2	MEP	APBT
aa01	R subcort.	0.151	10	13	13	3	3	0	1
br01	L cort.	0.354	4	4	5	0	1	0	1
cs03	L cort.	0.337	14	14	13	0	1	0	1
dh01	L subcort.	0.059	22	23		1		1	0
dt01	R subcort.	0.074	15	18	19	3	4	0	1
gc01	R subcort.	0.206	22	23	23	1	1	1	0
gv01	R subcort.	0.008	23	27	28	4	5	1	0
gw01	L subcort.	0.278	20	23	22	3	2	0	1
hg01	R subcort	0.015	26	26	28	0	2	0	0
hm01	R subcort.	0.145	9	13	12	4	3	0	0
jv01	L Cort	0.326	4	4	5	0	1	0	0
kn01	R subcort.	0.117	18	21		3		0	0
kr01	L subcort.	0.183	15	17	17	2	2	1	0
ld01	L cort.	0.246	6	7	6	1	0	0	1
le01	L cort.	0.296	10	9	12	1	2	0	1
lh01	L subcort.	0.165	10	9	11	1	1	0	1
lm01	L subcort.	0.179	23	28	29	5	6	1	1
mh01	R subcort.	0.266	22	24	24	2	2	1	0
mk01	L subcort.	0.420	5	5	7	0	2	0	1
ml01	L cort.	0.050	27	29	30	2	3	1	0
ml02	L cort.	0.021	25	25	27	0	2	1	0
pc01	R subcort.	0.054	23	24	24	1	1	1	1
rv01	L subcort.	0.161	10	9	16	1	6	0	1
tp01	R subcort.	0.060	24	26	28	2	4	1	0
ts01	L subcort	0.188	16	15	15	1	1	1	1
vh01	L subcort.	0.056	11	15	13	4	2	0	1
wh01	L cort.	0.049	24	26	26	2	2	1	0
wm01	L cort.	0.073	11	15		4		0	1

The Matlab code to produce a 4D Analyze pair of files is:

```
function [a] = sDWscans(fname,D)
% Function to create volumes of synthetic Diffusion-weighted scans
% for input volume fname whose
```

```
% statistics conform to given diffusion tensor D.
% - for synthetically augmenting a volume of DWI to one with more
% directions

a = [];
b = 1000;
%g = load(['./g_13FlipYZmatlab.txt']);
gv = load(['e:/gc01_bvecs.txt']);
gv = gv';
% Flip z col of g vector
%gv(:,3) = -gv(:,3);

% Generate the diffusion tensors (written to ANALYZE format)
%[PE,EVx,EVy,EVz,fa,D,rgb] = ...
%  dti('G:\Original Scanner data\fr01\FR01 pre DTI\',...
%  'C:\MATLAB7\work\mri\',...
%  'ns032i00001.img', [2,128,128,36,12]);
[t2S0,pdim,dtype] = readanalyze('mriT2');

for i = 1:max(size(gv))
    fprintf('Generating volume %i\n',i);

    fid = fopen(['sdti/',fname,'_sDTI_',num2str(i),'.img'], 'wb', 'ieee-le');
    fprintf(['sdti/',fname,'_sDTI_',num2str(i),'.img\n'])
    fprintf('DW gradient direction: %0.3f %0.3f %0.3f\n',gv(i,:));

    % Now create i volumes of DW signals with given DT
    for z = 1:36
        d = squeeze(D(:,:,z,:,:));
        s0 = t2S0(:,:,z);
        for y = 1:128
            for x = 1:128
                dt = squeeze(d(x,y,:,:));
                aslice(x,y) = s0(x,y)*exp(-b*gv(i,:)*dt*gv(i,:)');
            end
        end
        a(:,:,z) = aslice(:,:);
        imshow(aslice,[])
        fwrite(fid, aslice, 'float32');
    end
    ahdr = create_analyze;
    write_analyze(['sdti/', fname,'_sDTI_',...
        num2str(i), '.hdr'],ahdr,0);
    fclose(fid);
end
fprintf('...Done.\n');
```

Appendix B

Comparison of 12- and 30-direction DTI

Background and methods During the MNL stroke study, a 30-direction diffusion-weighted scan of a healthy patient was obtained for comparison with a 12-direction scan of the same patient obtained previously. The aim was to compare the results of the probabilistic tractography from the two data sets. The DWI acquisition parameters for both scans are summarised in Table B.1. Despite more than doubling the number of directions, the halved TR and the lower z-resolution meant that the total scan time was about about the same in each case.

# directions	12	30
TR (ms)	4800	2700
TE (ms)	88	88
Resolution	128×128×36	128×128×25
Voxel size (mm)	1.8×1.8×3.0	1.8×1.8×6.5
Number of averages	4	4

Table B.1: DWI acquisition parameters for 12- and 30-direction scans.

Results Results are shown in Figures B.1 and B.2 below. The FA map from the 30-direction scan was much less noisy than that from the 12-direction scan. The principal eigenvector field was also much smoother, reflecting the reduced uncertainty in fibre orientation. The background slices in the figures are FA maps. Introducing a lower threshold

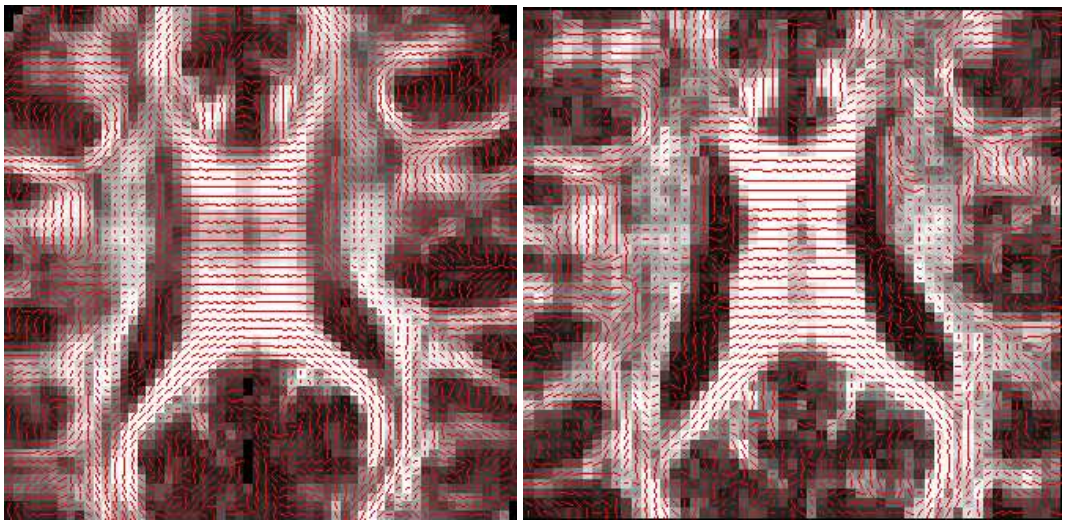

Figure B.1: Principal eigenvector field comparison for subject ps01: The 30-direction scan (left) is much smoother, particularly in regions of partial volume effects like the edges of the ventricles.

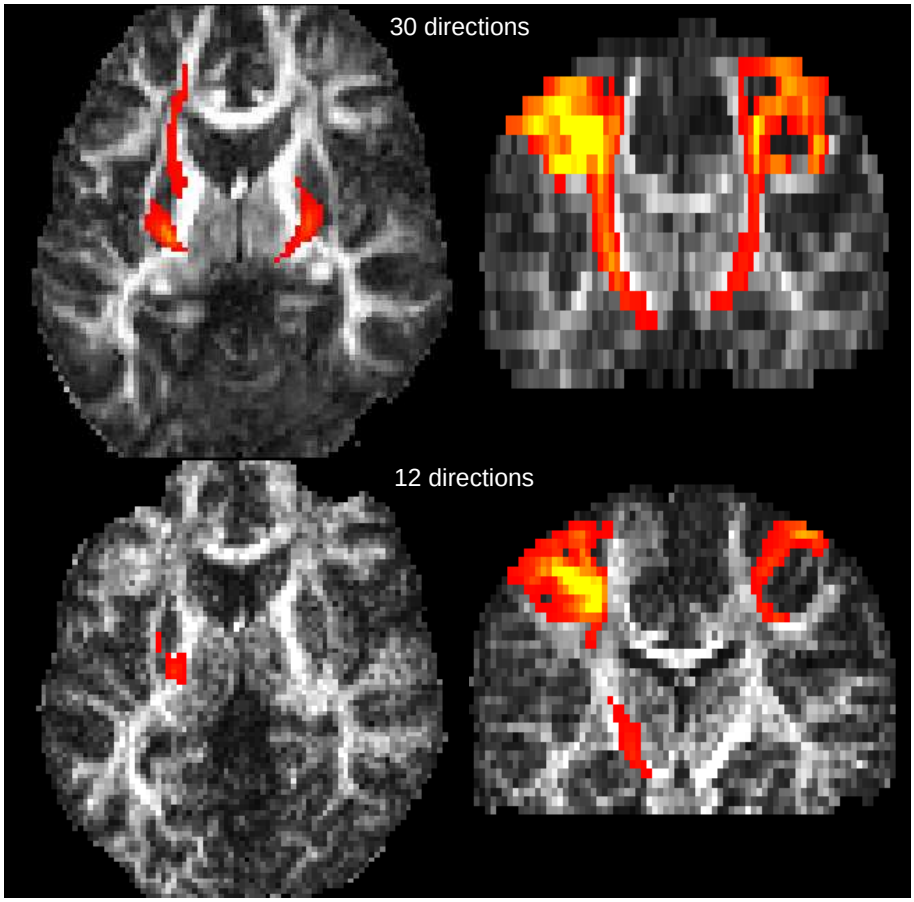

Figure B.2: Tractography comparison for subject ps01: The 30-direction scan (top) gave much better resolution of the FA map (background image), and gave much better results in regions of known anatomical connectivity. In both images, all voxels whose connectivity values were below 1% have been thresholded out.

of 1% for the connected tracts in the 12-direction data obliterated any significant connectivity. The CST connectivity was barely above the noise level. In the 30-direction data, the ProbTrack algorithm found significant connectivity in the CST that survived the introduction of a 1% threshold.

Given the better results from the 30-direction scan, it would have been very interesting to have applied a 30-direction scan to a subject with stroke to compare connectivity results in the lesioned hemisphere.

Appendix C

Sample linux batch script for FSL

The following script was used to process the Analyze .hdr/.img pairs, compute the diffusion parameters (BEDPOST), and coregister the T_1 images into the diffusion space (FLIRT).

```
#!/bin/bash
# My first script. Run by going cat bedposter | sh from peter/bin
date
# echo "This is a script for running FSL."
# echo "BET: Brain Extraction Tool"
# echo "FLIRT: linear image registration to align the dti volumes"
# echo "with the T2"
# echo "FDT/dtifit: to create the FA and eigenvector volumes"
# echo "and, finally,"
# echo "BEDPOST: the Bayesian estimation of Diffusion Parameters"
# echo "(which takes a LONG time)"
# echo " "
working_dir="/mnt/share/PETER/fsl_working"

# done:  ps01 tp01 aa01 dh01 di01 fr01 gt01 jv01 ld01 le01 lm01
mk01 ml02
#
#gc01 gv01 ml01 tp01 ml02 pc01
for subj in aa01 gc01 cs03 lm01 ml01 tp01 ml02 pc01; do
subj_dir=$subj"_12"
subj_proc=$subj"proc"
subj_T1=$subj"_T1"

# Put ANALYZE T2 pairs and bvals and bvecs files into each folder
#
cp $working_dir/ps01_61/bvals $working_dir/$subj_dir/
cp $working_dir/ps01_61/bvecs $working_dir/$subj_dir/
cp /media/USBD/proc/$subj_proc/xT2.hdr $working_dir/$subj_dir/
cp /media/USBD/proc/$subj_proc/xT2.img $working_dir/$subj_dir/
mv $working_dir/$subj_dir/xT2.hdr $working_dir/$subj_dir/nodif.hdr
mv $working_dir/$subj_dir/xT2.img $working_dir/$subj_dir/nodif.img
ls $working_dir/$subj_dir

# Apply BET to 4D file
#
```

```
echo "1. Applying BET to $subj"
$FSLDIR/bin/bet $working_dir/$subj_dir/data
$working_dir/$subj_dir/data_brain -f 0.3 -g 0 -m -t -s
#
# # and to T2 file
# #
$FSLDIR/bin/bet $working_dir/$subj_dir/nodif
$working_dir/$subj_dir/nodif_brain
-f 0.3 -g 0 -m -t -s
ls $working_dir/$subj_dir
#
# # # # # Apply FLIRT NOTE:   This is all done by spm2 (17/1/2007)
# # # # #
# # # # $FSLDIR/bin/flirt -in $working_dir/$subj_dir/data_brain.nii.gz
-ref $working_dir/$subj_dir/nodif.hdr
-out #$working_dir/$subj_dir/data_brainf.nii.gz
-omat $working_dir/$subj_dir/data_brainf.nii.mat
-bins 256 -cost corratio
-searchrx -90 #90 -searchry -90 90 -searchrz -90 90 -dof 6
-interp trilinear
# #
# # Fit the tensors
# #
echo "2. Fitting tensors to $subj"
$FSLDIR/bin/dtifit --data=$working_dir/$subj_dir/data
--out=$working_dir/$subj_dir/dti
--mask=$working_dir/$subj_dir/nodif_brain_mask
--bvecs=$working_dir/$subj_dir/bvecs
--bvals=$working_dir/$subj_dir/bvals

echo " "
ls $working_dir/$subj_dir
echo " "
bedpost_datacheck $working_dir/$subj_dir
# Bayesian Estimation of Diffusion Parameters Obtained By (Monte Carlo)
Sampling # Techniques
#
echo "3. BEDPOSTing $subj"
$FSLDIR/bin/bedpost $working_dir/$subj_dir
echo "End bedposter."
echo " "
echo " "
# The next bit extracts the brain from the T1 scan for reg with FLIRT
$FSLDIR/bin/bet $working_dir/T1/$subj/t1 $working_dir/T1/$subj/T1_brain
-f 0.3 -g 0 -m -t -s
# Create the T1 to FA space transformation matrix
/usr/share/fsl/bin/flirt -in $working_dir/T1/$subj/T1_brain.nii.gz
```

```
-ref $working_dir/$subj_dir/nodif_brain.nii.gz -out
$working_dir/T1/$subj_dir/T1_brain_dreg.nii.gz -omat
$working_dir/T1/$subj_dir/T1_brain_dreg.nii.mat -bins 256 -cost corratio
-searchrx -90 90 -searchry -90 90 -searchrz -90 90 -dof 6
-interp trilinear -omat $subj\T12FA.mat

done
```

Appendix D

Matlab code

The following code was used to produce vector images of the FA and the principal diffusion direction. Function RGBFAVOL calls RGBFA to calculate each slice, then organises the slices into .png volumes of specified orientation, and with or without the principal eigenvectors.

```
function rgbfavol(imstackdir,...
    subj,...
    rgb,fa,EVx,EVy,EVz,...
    orientation) % axial/coronal/sagittal?

%clear all;

iptsetpref('ImshowAxesVisible','on')
[xres,yres,zres,i,j] = size(rgb);
quiverOnOff = 0;

vol = subj;

 switch orientation
        case 'a'
            for slicenum = 1:zres
                outdir = [imstackdir subj 'a/'];
                if exist(outdir)==0
                    mkdir(outdir);
                end
                clf
                f = squeeze(rgb(:,:,slicenum,:));faf = fa(:,:,slicenum);
                g = imrotate(f,-90);fag = imrotate(faf,-90);
                h = uint16(round(g*65535));
                im = image(h,'AlphaData',fag);
                alph = fag;
                brighten(0.3);
                hold on
                h2 = quiver(fliplr(EVx(:,:,slicenum)'),...
                fliplr(EVy(:,:,slicenum)'),'color','w');
                set(h2,'AutoScaleFactor',1,'ShowArrowhead','on');
                axis equal
                fprintf('Slice number %i\n',slicenum)
                if slicenum < 10
```

```
            filestr = [outdir vol '_00' num2str(slicenum) '.png'];
        elseif slicenum > 99
            filestr = [outdir vol '_' num2str(slicenum) '.png'];
        else
            filestr = [outdir vol '_0' num2str(slicenum) '.png'];
        end
        switch quiverOnOff
            case 1
             set(h2,'Visible','on');
            case 0
             set(h2,'Visible','off');
        end
        set(gcf,'Color',[0 0 0]);
        axis tight
        axis off
        set(gcf,'InvertHardCopy','off');
        %imwrite(h,filestr,'png','Alpha',alph,'Background',[0 0 0]);
        saveas(gcf,filestr);
    end %slicenum

case 'c'
    for slicenum = 1:yres
        outdir = [imstackdir subj 'c/'];
        if exist(outdir)==0
            mkdir(outdir);
        end
        clf
        f = squeeze(rgb(:,slicenum,:,:));faf = squeeze(fa(:,slicenum,:));
        g = imrotate(f,-90);fag = imrotate(faf,-90);
        h = uint16(round(g*65535));
        brighten(0.3);
        im = image(h,'AlphaData',fag);
        alph = fag;
        hold on
        px = permute(EVx,[1,3,2]);
        pz = permute(EVz,[1,3,2]);
        h2 = quiver(fliplr(px(:,:,slicenum)'),...
            fliplr(pz(:,:,slicenum)'),'color','w');
        set(h2,'AutoScaleFactor',1,'ShowArrowhead','on');
        axis xy
        axis([20 110 1 36]);
        daspect([5/3 1 1]);
        fprintf('Slice number %i\n',slicenum)
        if slicenum < 10
            filestr = [outdir vol '_00' num2str(slicenum) '.png'];
        elseif slicenum > 99
            filestr = [outdir vol '_' num2str(slicenum) '.png'];
```

```
            else
                filestr = [outdir vol '_0' num2str(slicenum) '.png'];
            end
            switch quiverOnOff
               case 1
                 set(h2,'Visible','on');
               case 0
                 set(h2,'Visible','off');
            end
            set(gcf,'Color',[0 0 0]);
            axis tight
            axis off
            set(gcf,'InvertHardCopy','off');
            %imwrite(h,filestr,'png','Alpha',alph,'Background',[0,0,0]);
            saveas(gcf,filestr);
         end %for slicenum

      case 's'
          for slicenum = 1:xres
            outdir = [imstackdir subj 's/'];
            if exist(outdir)==0
                mkdir(outdir);
            end
             clf
            f = squeeze(rgb(slicenum,:,:,:));faf = squeeze(fa(slicenum,:,:));
            g = imrotate(f,-90);fag = imrotate(faf,-90);
            h = uint16(round(g*65535));
            brighten(0.3);
            im = image(h,'AlphaData',fag);
            alph = fag;
            hold on;
            py = permute(EVy,[2,3,1]);
            pz = permute(EVz,[2,3,1]);
            h2 = quiver(fliplr(py(:,:,slicenum)'),...
               fliplr(pz(:,:,slicenum)'),'color','w');
            set(h2,'AutoScaleFactor',1,'ShowArrowhead','on');
            axis xy
            daspect([5/3 1 1]);
            fprintf('Slice number %i\n',slicenum)
             if slicenum < 10
                 filestr = [outdir vol '_00' num2str(slicenum) '.png'];
             elseif slicenum > 99
                 filestr = [outdir vol '_' num2str(slicenum) '.png'];
             else
                 filestr = [outdir vol '_0' num2str(slicenum) '.png'];
             end
             switch quiverOnOff
```

```
                    case 1
                        set(h2,'Visible','on');
                    case 0
                        set(h2,'Visible','off');
                end

                axis tight
                axis off
                set(gcf,'InvertHardCopy','off');
                set(gcf,'Color',[0 0 0]);
                %imwrite(h,filestr,'png','Alpha',alph,'Background',[0,0,0]);
                saveas(gcf,filestr);
            end %for slicenum
        end %switch orientation

close all;

function [h,alph] = rgbfa(rgb,fa,EVx,EVy,EVz,slicenum,orientation,quiverOnOff)
% RGBFA produces series of slices of RGB color plots of FA using the tensor
% data produced by siemens_analyze.m and dti.m.
% Quiver plots are also produced to show the directions of the principle
% eigenvectors of the diffusion tensors. There is also code for producing
% segmented plots for each of the three directions.
% INPUTS: rgb : 5D rgb volume of principle eigenvector data
%         EVx : 3D matrix of x components of principle eigenvector
%         EVy : 3D matrix of y components of principle eigenvector
%         EVz : 3D matrix of z components of principle eigenvector
%         slicenum : slice number
%         orientation : slice orientation - 'a', 'c', or 's'
%         quiverOnOff is a 0/1 flag for superimposing principle
%         eigenvectors (projection onto plane).
%
%
%-------------------------------------------------------------------------

close all;
%siemens_analyze;
figure(slicenum);
iptsetpref('ImshowAxesVisible','on')
[xres,yres,zres,i,j] = size(rgb);
fprintf('Slice number %i\n',slicenum)

    switch orientation
        case 'a'
            f = squeeze(rgb(:,:,slicenum,:));faf = fa(:,:,slicenum);
            g = imrotate(f,270);fag = imrotate(faf,270);
            h = uint16(round(g*65535));
```

```
            im = image(h,'AlphaData',fag);
            alph = faf;
            brighten(0.3);
            hold on
            h2 = quiver(fliplr(EVx(:,:,slicenum)'),...
                fliplr(EVy(:,:,slicenum)'),'color','w');
            set(h2,'AutoScaleFactor',1,'ShowArrowhead','off');
            axis equal
        case 'c'
            f = squeeze(rgb(:,slicenum,:,:));faf = squeeze(fa(:,slicenum,:));
            g = imrotate(f,270);fag = imrotate(faf,270);
            h = uint16(round(g*65535));
            brighten(0.3);
            im = image(h,'AlphaData',fag);
            alph = fag;
            hold on
            px = permute(EVx,[1,3,2]);
            pz = permute(EVz,[1,3,2]);
            h2 = quiver(fliplr(px(:,:,slicenum)'),...
                fliplr(pz(:,:,slicenum)'),'color','w');
            set(h2,'AutoScaleFactor',1,'ShowArrowhead','off');
            axis xy
            axis([20 110 1 36]);
            daspect([5/3 1 1]);
        case 's'
            f = squeeze(rgb(slicenum,:,:,:));faf = squeeze(fa(slicenum,:,:));
            g = imrotate(f,270);fag = imrotate(faf,270);
            h = uint16(round(g*65535));
            brighten(0.3);
            im = image(h,'AlphaData',fag);
            alph = fag;
            hold on;
            py = permute(EVy,[2,3,1]);
            pz = permute(EVz,[2,3,1]);
            h2 = quiver(fliplr(py(:,:,slicenum)'),...
                fliplr(pz(:,:,slicenum)'),'color','w');
            set(h2,'AutoScaleFactor',1,'ShowArrowhead','off');
            axis xy
            daspect([5/3 1 1]);
    end
    set(gcf,'Color',[0 0 0]);
    axis tight
    axis off
switch quiverOnOff
    case 1
    set(h2,'Visible','on');
    case 0
```

```
    set(h2,'Visible','off');
end


%--------------------------------------------------------------------------
```

References

[1] M. Barnes, B. Dobkin, and J. Bogousslavsky. *Recovery after Stroke*. Cambridge University Press, 2005.

[2] N.S. Ward. Plasticity and the functional reorganization of the human brain. *International Journal of Psychophysiology*, 58:158–161, 2005.

[3] P.M. Rossini, C. Calautti, F. Pauri, and J.-C. Baron. Post-stroke plastic reorganisation in the adult brain. *The Lancet Neurology*, 2:493–502, 2003.

[4] J.W. Stinear and W.D. Byblow. Rhythmic bilateral movement training modulates corticomotor excitability and enhances upper limb motricity poststroke: A pilot study. *Journal of Clinical Neurophysiology*, 21(2):124–131, March/April 2004.

[5] C.M. Stinear, V.K. Lim, P.A. Barber, J.P. Coxon, and W.D. Byblow. A novel stroke rehabilitation protocol: Preliminary evidence of hemispheric balancing and improved upper limb function. Poster presented at The Motor Control and Cognitive Neuroscience Conference, Dunedin, NZ, 2005.

[6] M. Rijntjes. Mechnanisms of recovery in stroke patients with hemiparesis or aphasia: new insights, old questions and the meaning of therapies. *Current Opinion in Neurology*, 19:76–83, 2006.

[7] T. Wieloch and K. Nikolich. Mechanisms of neural plasticity following brain injury. *Current Opinion in Neurobiology*, 16:1–7, 2006.

[8] R.J. Nudo. Mechanisms for recovery of motor function following cortical damage. *Current Opinion in Neurobiology*, 16:638–644, 2006.

[9] E.L. Hahn. Spin echoes. *Physical Review*, 80(4):580–594, 1950.

[10] H.Y. Carr and E.M. Purcell. Effects of diffusion on free precession in nuclear magnetic resonance experiments. *Physical Review*, 94(3):630–638, 1954.

[11] E.O. Stejskal and J.E. Tanner. Spin diffusion measurements: spin echoes in the presence of a time-dependent field gradient. *Journal of Chemical Physics*, 42:288–292, 1965.

[12] D.S. Tuch, T.G. Reese, M.R. Wiegell, and V.J. Wedeen. Diffusion MRI of complex neural architecture. *Neuron*, 40:885–895, 2003.

[13] D. Le Bihan, J.-F. Mangin, C. Poupon, C.A. Clark, S. Pappata, N. Molko, and H. Chabriat. Diffusion Tensor Imaging: Concepts and Applications. *Journal of Magnetic Resonance Imaging*, 13:534–546, 1990.

[14] R. Turner, D. Le Bihan, and J. Maier et al. Echo-planar imaging of intravoxel incoherent motion. *Radiology*, 177:407–414, 1990.

[15] T.E.J. Behrens, M.W. Wolrich, and M. Jenkinson et al. Characterization and propagation of uncertainty in Diffusion-Weighted MR imaging,. *Magnetic Resonance in Medicine*, 50:1077–1088, 2003.

[16] A. Ulug and P.C.M. van Zijl. Orientation-Independent Diffusion Imaging Without Tensor Diagonalization: Anisotropy Definitions Based on Physical Attributes of the diffusion ellipsoid. *Journal of Magnetic Resonance Imaging*, 9:804–813, 1999.

[17] C. Pierpaoli and P. Basser. Towards a quantitative assessment of diffusion anisotropy. *Magnetic Resonance in Medicine*, 38:893–906, 1996.

[18] P.J. Basser and C. Pierpaoli. Microstructural and physiological features of tissues elucidated by quantitative-diffusion-tensor MRI. *Journal of Magnetic Resonance Series B*, 111:209–219, 1996.

[19] S. Mori, B.J. Crain, V.P. Chacko, and P.C.M. van Zijl. Three-dimensional tracking of axonal projections in the brain by magnetic resonance imaging. *Annals of Neurology*, 45:265–269, 1999.

[20] S. Mori and P.C.M. van Zijl. Fibre tracking: principles and strategies – a technical review. *NMR in Biomedicine*, 15:468–480, 2002.

[21] P.G. Batchelor and M. Moakher et al. A rigorous framework for diffusion tensor calculus. *Magnetic Resonance in Medicine*, 53:221–225, 2005.

[22] E.R. Melhem, S. Mori, and G. Mukundan et al. Diffusion tensor MR imaging of the brain and white matter tractography. *American Journal of Radiology*, 178:3–16, 2002.

[23] M. Lazar, D.M. Weinstein, and J.S. Tsaruda et al. White matter tractography using diffusion tensor deflection. *Human Brain Mapping*, 18:306–321, 2003.

[24] S. Mori et al. `http://lban.med.jhmi.edu`, 2005.

[25] P. Fillard et al. `http://www-sop.inria.fr/epidaure/personnel/Pierre.Fillard`, 2005.

[26] Y. Matusani. `http://www.ut-radiology.umin.jp/people/matusani/dTV`, 2005.

[27] H.J. Park et al. `http://neuroimage.yonsei.ac.kr/dodti/`, 2005.

[28] S.M. Smith, M. Jenkinson, M.W. Woolrich, J. Andersson, C.F. Beckmann, T.E.J. Behrens, H. Johansen-Berg, P.R. Bannister, M. De Luca, I. Drobnjak, D.E. Flitney, R. Niazy, J. Saunders, J. Vickers, Y. Zhang, N. De Stefano, J.M. Brady, and P.M. Matthews. `http://www.fmrib.ox.ac.uk`, 2007. FMRIB: Oxford Centre for Functional Magnetic Resonance of the Brain.

[29] J. Konishi, K. Yamada, O. Kizu, H. Ito, K. Sugimura, K. Yoshikawa, M. Nakagawa, and T. Nishimura. MR tractography for the evaluation of functional recovery from lenticulostriate infarcts. *Neurology*, 64:108–113, 2005.

[30] J.S. Lee, M-K. Han, S.H. Kim, O-K. Kwon, and J.H. Kima. Fiber tracking by diffusion tensor imaging in corticospinal tract stroke: Topographical correlation with clinical symptoms. *NeuroImage*, 26:771–776, 2005.

[31] H. Parmar H, X. Golay, K.E. Lee, F. Hui, and Y.Y. Sitoh. Early experiences with diffusion tensor imaging and magnetic resonance tractography in stroke patients. *Singapore Medical Journal*, 47(3):198–203, 2006.

[32] A. Kunimatsu, S. Aoki, Y. Masutani, O. Abe, H. Mori, and K. Ohtomo. Three-dimensional white matter tractography by diffusion tensor imaging in ischaemic stroke involving the corticospinal tract. *Neuroradiology*, 45(8):532–535, August 2003.

[33] S. Mori, S. Wakana, P.C.M. van Zijl, and L.M. Nagae-Poetscher. *MRI Atlas of Human White Matter*. Elsevier, Amsterdam and New York, 1st edition, 2005.

[34] D.S. Tuch and T.G. Reese et al. High angular resolution diffusion imaging reveals intravoxel white matter fiber heterogeneity. *Magnetic Resonance in Medicine*, 48:577–582, 2002.

[35] R. Watts, C. Liston, and N. Sumit et al. Using magnetic resonance diffusion tensor imaging and its applications to human brain development. *Mental Retardation and Developmental Disabilities Research Reviews*, 9:168–177, 2003.

[36] D.K. Jones. Determining and visualizing uncertainty in estimates of fibre orientation from diffusion tensor MRI. *Magnetic Resonance in Medicine*, 49:7–12, 2003.

[37] D.S. Tuch. Q-ball imaging. *Magnetic Resonance in Medicine*, 52:1358–1372, 2004.

[38] Derek K. Jones, Adam R. Travis, Greg Eden, Carlo Pierpaoli, and Peter Basser. PASTA: Pointwise assessment of streamline tractography attributes. *Magnetic Resonance in Medicine*, 53:1462–1467, 2005.

[39] G.J.M. Parker and D. Alexander. Probabilistic anatomical connectivity derived from the microscopic persistent angular structure of cerebral tissue. *Philosophical Transactions of The Royal Society B*, 360:893–902, 2005.

[40] T.E.J. Behrens, H. Johansen-Berg, and M.W. Woolrich et al. Non-invasive mapping of connections between human thalamus and cortex using diffusion imaging. *Nature Neuroscience*, 6(7):750–757, 2003.

[41] T. Behrens. `http://www.jiscmail.ac.uk/cgi-bin/webadmin`, 2007. JISCmail: FSL help Item #009632.

[42] A.I. Holodny, D.M. Gor, R. Watts, P.H. Gutlin, and A.M. Ulug. Diffusion-Tensor MR Tractography of somatotopic organization of corticospinal tracts in the internal capsule: Initial anatomic results in contradistinction to prior reports. *Radiology*, 234:649–653, 2005.

[43] M. Zarei, H. Johansen-Berg, and M. Jenkinson et al. Two-dimensional population map of cortical connections in the human internal capsule. *Journal of Magnetic Resonance Imaging*, 25:48–54, 2007.

[44] F. Bloch. Nuclear induction. *Physical Review*, 70(7 and 8):460–474, October 1946.

[45] A. Einstein. On the movement of small particles suspended in stationary liquids required by the molecular-kinetic theory of heat. *Annalen der Physik*, 17:549–560, 1905.

[46] M. Haw. Einstein's random walk. *Physics World*, January 2005.

[47] D. Le Bihan. *Categorical Course in Physics: The Basic Physics of MR Imaging*, chapter 11, pages 131–145. RSNA, 1997.

[48] M. Neeman, J. P. Freyer, L. Sillerud, J. Mattiello, P.J. Basser, and D. Le Bihan. *Diffusion and Perfusion Magnetic Resonance Imaging*, chapter 5, pages 73–91. Raven Press, New York, 1995.

[49] R. Turner and D. Le Bihan. *Diffusion MR Imaging: Echo-Planar Techniques*, chapter 2, pages 51–55. Raven Press, New York, 1995.

[50] P.B. Kingsley. Introduction to Diffusion Tensor Imaging Mathematics (parts 1–3). *Concepts in Magnetic Resonance*, 28A(2):101–179, 2006.

[51] G.J.M. Parker. Analysis of MR diffusion weighted images. *British Journal of Radiology*, 77(2):S176–S185, 2004.

[52] S.C. Partridge, P. Mukherjee, R.G. Henry, S.P. Miller, J.I. Berman, H. Jin, Y. Lu, O.A. Glenn, D.M. Ferriero, A.J. Barkovich, and D.B. Vigneron. Diffusion Tensor Imaging: Serial quantitation of white matter tract maturity in premature newborns. *NeuroImage*, 22(3):1302–14, 2004.

[53] L. Hermoye and C. Saint Martin. Pediatric diffusion tensor imaging: normal database and observation of the white matter maturation in early childhood. *NeuroImage*, 29(2):493–504, 2006.

[54] D. Bonekamp and L.M. Nagae et al. Diffusion tensor imaging in children and adolescents: Reproducibility, hemispheric, and age-related differences. *NeuroImage*, 34(2):733–742, 2007.

[55] N.S. Ward and J.M. Newton et al. Motor system activation after subcortical stroke depends on corticospinal system integrity. *Brain*, 129:890–819, 2006.

[56] J.M. Newton and N.S. Ward et al. Non-invasive mapping of corticofugal fibres from multiple motor areas – relevance to stroke recovery. *Brain*, 129:1844–1858, 2006.

[57] C.M. Stinear, A.P. Barber, and P.R. Smale et al. Function potential in chronic stroke patients depends on corticospinal tract integrity. *Brain*, 130:170–180, 2007.

[58] Stanislaw Ulam. *Adventures of a Mathematician*. University of California Press, Berkeley, 3 edition, 1991.

[59] D. Jones. The effect of gradient sampling schemes on measures derived from diffusion tensor MRI: A Monte Carlo study. *Magnetic Resonance in Medicine*, 51:807–815, 2004.

[60] E. Heiervang, T.E.J. Behrens, C.E. Mackay, M.D. Robson, and H. Johansen-Berg. Between session reproducibility and between subject variability of diffusion MR tractography measures. *NeuroImage*, 33:867–877, 2006.

[61] A. Cherubini and G. Luccichenti et al. Multimodal fMRI tractography in normal subjects and in clinically recovered traumatic brain injury patients. *NeuroImage*, 34:1331–1341, 2007.

[62] A. Aron, T.J. Behrens, S. Smith, M.J. Frank, and R.A. Poldrack. Triangulating a cognitive control network using diffusion-weighted magnetic resonance imaging (MRI) and functional MRI. *The Journal of Neuroscience*, 27(14):3743–3752, 2007.

[63] P. Leopardi. Recursive Zonal Equal Area (EQ) Sphere Partitioning Toolbox Release 1.10. `http://eqsp.sourceforge.net/`, 2005. Matlab toolbox.

[64] Wellcome Department of Imaging Neuroscience. `www.fil.ion.ucl.ac.uk/spm`.

[65] K. Williams. A definition of spatial orientation for the Insight Toolkit. *Insight Journal*, August-December 2005.

[66] Maxime Guye, Geoffrey J.M. Parker, Mark Symms, Philip Boulby, Claudia A.M. Wheeler-Kingshott, Afraim Salek-Haddadi, Gareth J. Barker, and John S. Duncan. Combined functional MRI and tractography to demonstrate the connectivity of the human primary motor cortex in vivo. *NeuroImage*, 19:1349–1360, 2003.

[67] D.J. Werring, A.T. Toosy, C.A. Clark, G.J.M. Parker, G.J. Barker, D.H. Miller, and A.J. Thompson. Diffusion tensor imaging can detect and quantify corticospinal tract degeneration after stroke. *Journal of Neurology, Neurosurgery and Psychiatry*, 69:269–272, 2000.

[68] J. Cohen. *Statistical Power Analysis for the Behavioral Sciences*. Lawrence Erlbaum Associates, Hillsdale, NJ, 2nd edition, 1988.